



저작자표시-비영리-변경금지 2.0 대한민국

이용자는 아래의 조건을 따르는 경우에 한하여 자유롭게

- 이 저작물을 복제, 배포, 전송, 전시, 공연 및 방송할 수 있습니다.

다음과 같은 조건을 따라야 합니다:



저작자표시. 귀하는 원 저작자를 표시하여야 합니다.



비영리. 귀하는 이 저작물을 영리 목적으로 이용할 수 없습니다.



변경금지. 귀하는 이 저작물을 개작, 변형 또는 가공할 수 없습니다.

- 귀하는, 이 저작물의 재이용이나 배포의 경우, 이 저작물에 적용된 이용허락조건을 명확하게 나타내어야 합니다.
- 저작권자로부터 별도의 허가를 받으면 이러한 조건들은 적용되지 않습니다.

저작권법에 따른 이용자의 권리와 책임은 위의 내용에 의하여 영향을 받지 않습니다.

이것은 [이용허락규약\(Legal Code\)](#)을 이해하기 쉽게 요약한 것입니다.

[Disclaimer](#)



공학박사 학위논문

Design of Pyrophosphate Cathode Materials for High-Performance Rechargeable Na-Ion Batteries

고성능 소듐 이차 전지용
피로인산염계 양극 재료 설계

2017년 2월

서울대학교 대학원
재료공학부
송희조

Design of Pyrophosphate Cathode Materials for High-Performance Rechargeable Na-Ion Batteries

**A THESIS SUBMITTED TO
DEPARTMENT OF MATERIALS SCIENCE AND
ENGINEERING
SEOUL NATIONAL UNIVERSITY**

**FOR THE DEGREE OF
DOCTOR OF PHILOSOPHY**

**BY
Hee Jo Song**

FEBRUARY 2017

Abstract

Design of Pyrophosphate Cathode Materials for High-Performance Rechargeable Na-Ion Batteries

Hee Jo Song

Department of Materials Science and Engineering

The Graduate School

Seoul National University

Ever-increasing demands for energy production and energy storage, environmental-friendly energy storage systems have become important issues at the present time. Rechargeable batteries are one of the most attractive electrochemical energy storage systems to store both conventional energy from fossil fuels, nuclear reactions, and renewable energy from solar, wind, *etc.* Among the rechargeable batteries, rechargeable LIBs have been developed in recent years as power sources in energy storage because of their high power and energy density, little memory effect together with long operating life and

good environmental compatibility. In addition, recent advances in LIB technologies toward increasing the gravimetric and volumetric energy densities enable LIB to apply in the large-scale electrical energy storage such as electrical vehicles (EVs) or grid-scale energy storage systems (EESs). However, limitation of the availability of high-cost Li resources resulting from the lack of reserves and their uneven distribution have led to a search for alternative battery system.

As a post LIBs, rechargeable Na-ion batteries (NIBs) are considered as one of the potential candidates for large-scale energy storage systems because of the abundance and low cost of sodium resources, and similar electrochemical behavior of Na-ion with the Li-ion for intercalation in the cathode. So, the development of high-performance cathode materials is needed for their NIB application. While there exist many challenges in the fabrication of cathodes, one of the polyanionic framework, $\text{Na}_2\text{MP}_2\text{O}_7$ (M = transition metal), has been in the spotlight as a potential cathode material in NIBs because of its thermal, chemical stability and good electrochemical performance (good rate capability, cyclability in $\text{Na}_2\text{FeP}_2\text{O}_7$, and high operating voltage in $\text{Na}_2\text{CoP}_2\text{O}_7$).

In this thesis, $\text{Na}_2\text{MP}_2\text{O}_7$ (M = Fe, Co) cathode materials are designed for high-performance NIBs through both nano-engineering and compositional engineering. Also, free-standing electrode is fabricated by incorporating this high-performance cathode material with flexible electrode for high-performance flexible electrode. For this, first, general synthetic process for

synthesizing $\text{Na}_2\text{MP}_2\text{O}_7$ nanoparticles embedded in carbon ($\text{Na}_2\text{MP}_2\text{O}_7/\text{C}$ nanocomposite; $\text{Na}_2\text{MP}_2\text{O}_7\text{-NPs/C}$) is presented. $\text{Na}_2\text{MP}_2\text{O}_7\text{-NPs/C}$ prepared via a citric acid-assisted sol-gel method, followed by a post heat treatment, ball milling and re-heat treatment process ($\text{HT}\rightarrow\text{BM}\rightarrow\text{HT}$). From this synthetic process, uniform-size $\text{Na}_2\text{MP}_2\text{O}_7$ ($\text{M} = \text{Fe, Co, Ni}$) nanoparticles under 50 nm which are homogeneously embedded in carbon can be obtained.

In Fe-based pyrophosphate, $\text{Na}_2\text{FeP}_2\text{O}_7\text{-NPs/C}$ exhibits not only reversible capacity near the theoretical value (97 mA h g^{-1}) over the voltage range of 2.0–4.0 V (vs. Na/Na^+). Moreover, they display superior rate capability of 77, 70, 66 and 65 mA h g^{-1} even at high rates of 10, 20, 30 and 60 C, respectively. Equally notable is the exceptional long-term cyclability at high rates. At the rate of 10 and 60 C, capacity retention at 10000 cycles is over 80%, respectively. Meanwhile, electrochemical performance of Fe-based pyrophosphate is improved by compositional change. Compared to $\text{Na}_2\text{FeP}_2\text{O}_7$, more electrochemical $\text{Fe}^{2+}/\text{Fe}^{3+}$ redox reaction can occur in $\text{Na}_{3.12}\text{Fe}_{2.44}(\text{P}_2\text{O}_7)_2$ when charging/discharging, which anticipates in higher practical capacity and energy density than $\text{Na}_2\text{FeP}_2\text{O}_7$. So, for improving the energy density of Fe-based pyrophosphate, therefore, $\text{Na}_{3.12}\text{Fe}_{2.44}(\text{P}_2\text{O}_7)_4$ nanoparticles embedded in carbon ($\text{Na}_{3.12}\text{Fe}_{2.44}(\text{P}_2\text{O}_7)_4/\text{C}$ nanocomposite; $\text{Na}_{3.12}\text{Fe}_{2.44}(\text{P}_2\text{O}_7)_4\text{-NPs/C}$) is synthesized for the same synthetic process. Indeed, Specific capacity of $\text{Na}_{3.12}\text{Fe}_{2.44}(\text{P}_2\text{O}_7)_2\text{-NPs/C}$ is measured to be higher than that of $\text{Na}_2\text{FeP}_2\text{O}_7\text{-NPs/C}$. Furthermore, reduced graphene oxide-supported $\text{Na}_{3.12}\text{Fe}_{2.44}(\text{P}_2\text{O}_7)_4$ -

NPs/C ($\text{Na}_{3.12}\text{Fe}_{2.44}(\text{P}_2\text{O}_7)_4$ -NPs/C/rGO) composite is also synthesized. The addition of small amount of rGO in $\text{Na}_{3.12}\text{Fe}_{2.44}(\text{P}_2\text{O}_7)_4$ -NPs/C exhibits not only a high reversible electrochemical reaction, but also a superior rate capability (92, 85 and 78 mA h g⁻¹ at 2, 5 and 10 C), and long-term cyclic stability (capacity retention of 70% over 5000 cycle at 10 C). This low-cost and high-performance composite can be a promising cathode material in NIBs.

Co-based pyrophosphate is studied. Among the three distinct polymorphs in $\text{Na}_2\text{CoP}_2\text{O}_7$, it is known that triclinic polymorph (rose) exhibits similar electrochemical behavior with $\text{Na}_2\text{FeP}_2\text{O}_7$, but significantly higher operating voltage than $\text{Na}_2\text{FeP}_2\text{O}_7$ and even other NIB cathode materials. However, it is hard to obtain rose phase in ordinary synthetic process. Fine controls can make it possible to synthesize rose phase. So, several synthesis conditions that can obtain the rose phase are discussed in detail. Rose phase can be obtained in stoichiometric compound annealed at low temperature under 500 °C. Also, With the increasing of Co element and decreasing of Na element in non-stoichiometric $\text{Na}_{2-2x}\text{Co}_{1+x}\text{P}_2\text{O}_7$ compounds, metastable rose phase can be obtained stably at higher annealing temperature over 500 °C compared to stoichiometric compound.

$\text{Na}_{2-2x}\text{Co}_{1+x}\text{P}_2\text{O}_7/\text{C}$ nanocomposites ($\text{Na}_{2-2x}\text{Co}_{1+x}\text{P}_2\text{O}_7$ -NPs/C) are synthesized for the same synthetic process with Fe-based pyrophosphate nanocomposites. In contrast to micro-sized bulk $\text{Na}_{2-2x}\text{Co}_{1+x}\text{P}_2\text{O}_7$, metastable rose becomes to major products both stoichiometric and non-stoichiometric

$\text{Na}_{2-2x}\text{Co}_{1+x}\text{P}_2\text{O}_7$ -NPs/C ($0 \leq x \leq 0.2$) heat-treated at 600 °C. All three rose phase $\text{Na}_2\text{Co}_1\text{P}_2\text{O}_7$ -NPs/C, $\text{Na}_{1.8}\text{Co}_{1.1}\text{P}_2\text{O}_7$ -NPs/C and $\text{Na}_{1.6}\text{Co}_{1.2}\text{P}_2\text{O}_7$ -NPs/C exhibit the better electrochemical performance than B- $\text{Na}_{1.8}\text{Co}_{1.1}\text{P}_2\text{O}_7$ /C. In particular, rose phase $\text{Na}_{1.8}\text{Co}_{1.1}\text{P}_2\text{O}_7$ -NPs/C exhibits a good cyclic stability with the reversible capacity more than 80 mA h g⁻¹. This high-performance $\text{Na}_{2-2x}\text{Co}_{1+x}\text{P}_2\text{O}_7$ -NPs/C can be a promising high-voltage cathode material in NIBs.

Finally, $\text{Na}_2\text{FeP}_2\text{O}_7$ -NPs/C uniformly loaded on the surface of flexible porous carbon cloth ($\text{Na}_2\text{FeP}_2\text{O}_7$ -NPs/C@PCC) electrode is fabricated by dip-coating process, This flexible electrode without any conductive agents and polymeric binders also exhibit excellent rate capability and long-term cyclability at high rate of 10 C (56 mA h g⁻¹ after 2000 cycles). We show high-performance free-standing $\text{Na}_2\text{FeP}_2\text{O}_7$ -NPs/C@PCC electrodes for possible application in flexible NIBs.

Overall, this thesis focuses on the synthesis of $\text{Na}_2\text{MP}_2\text{O}_7$ /C nanocomposites and evaluation of their electrochemical performance for high-performance NIB cathode material through nano-engineering and compositional engineering. Also, their application to free-standing electrode combined with the porous carbon cloth for possible flexible NIBs is investigated. Furthermore, synthetic strategy in this thesis would open the preparation of other sodium metal pyrophosphate nanocomposites, and will

provide a new breakthrough to solve the faced problems in rechargeable NIBs and other energy storage devices.

Keywords: pyrophosphate, nanocomposite, sol-gel, flexible electrode, carbon cloth, dip-coating, cathode, sodium-ion battery, Na-ion battery

Student Number: 2010-20608

Table of Contents

Abstract	i
Table of Contents.....	vii
List of Tables	x
List of Figures	xii
Chapter 1. Introduction	1
1.1 Overview: Rechargeable Batteries for Energy Storage Systems	1
1.2 Aim and Strategies	14
1.3 Bibliography	16
Chapter 2. Background and Literature Review.....	21
2.1 Li-Ion and Na-Ion Batteries	21
2.2 Polyanionic Cathode Materials for Na-Ion Battery	26
2.3 Nanotechnologies for Battery Electrodes	30
2.4 Flexible Batteries	34
2.5 Bibliography	37
Chapter 3. $\text{Na}_2\text{MP}_2\text{O}_7/\text{C}$ Nanocomposites.....	40

3.1	Experiments	40
3.2	Synthesis of $\text{Na}_2\text{MP}_2\text{O}_7/\text{C}$ Nanocomposites	43
3.2.1	$\text{Na}_2\text{MP}_2\text{O}_7\text{-NPs}/\text{C}$ ($\text{M} = \text{Fe}$)	43
3.2.2	$\text{Na}_2\text{MP}_2\text{O}_7\text{-NPs}/\text{C}$ ($\text{M} = \text{Co, Ni}$).....	50
3.2.3	Nanocomposites Characterization.....	56
3.3	Bibliography	66

Chapter 4. Fe-Based Pyrophosphate 67

4.1	Experiments	67
4.2	$\text{Na}_2\text{FeP}_2\text{O}_7/\text{C}$ Nanocomposite for Na-Ion Batteries.....	70
4.3	$\text{Na}_{3.12}\text{Fe}_{2.44}(\text{P}_2\text{O}_7)_2/\text{C}$ Nanocomposites	91
4.3.1	$\text{Na}_{3.12}\text{Fe}_{2.44}(\text{P}_2\text{O}_7)_2/\text{C}$ Nanocomposite for Na-Ion Batteries	91
4.3.2	$\text{Na}_{3.12}\text{Fe}_{2.44}(\text{P}_2\text{O}_7)_2/\text{C/rGO}$ Nanocomposite for Na-Ion Batteries	102
4.4	Bibliography	119

Chapter 5. Co-Based Pyrophosphate 121

5.1	Experiments	121
5.2	Triclinic Phase $\text{Na}_{2-2x}\text{Co}_{1+x}\text{P}_2\text{O}_7$	124
5.2.1	Temperature Dependence.....	124
5.2.2	Time Dependence	130

5.3	$\text{Na}_{2-2x}\text{Co}_{1+x}\text{P}_2\text{O}_7/\text{C}$ Nanocomposites	137
5.3.1	Synthesis of $\text{Na}_{2-2x}\text{Co}_{1+x}\text{P}_2\text{O}_7/\text{C}$ Nanocomposites	137
5.3.2	$\text{Na}_{2-2x}\text{Co}_{1+x}\text{P}_2\text{O}_7/\text{C}$ Nanocomposites for Na-Ion Batteries	148
5.4	Bibliography	162

Chapter 6. Free-Standing Electrodes 163

6.1	Experiments	163
6.2	Porous Carbon Cloth.....	165
6.3	$\text{Na}_2\text{FeP}_2\text{O}_7/\text{C}$ Nanocomposite on Porous Carbon Cloth	172
6.3.1	Fabrication of $\text{Na}_2\text{FeP}_2\text{O}_7/\text{C}$ Nanocomposite on Porous Carbon Cloth.....	172
6.3.2	$\text{Na}_2\text{FeP}_2\text{O}_7/\text{C}$ Nanocomposite on Porous Carbon Cloth for Na-Ion Batteries	179
6.4	Bibliography	183

Chapter 7. Conclusion..... 184

Abstract in Korean.....	187
Research Achievements.....	191

List of Tables

Table 1.1.1	Summary of the practical rechargeable batteries. [3]	8
Table 1.1.2	Crystal information of $\text{Na}_2\text{FeP}_2\text{O}_7$ and $\text{Na}_{3.12}\text{Fe}_{2.44}(\text{P}_2\text{O}_7)_2$	9
Table 1.1.3	Crystal information of orthorhombic and triclinic polymorph $\text{Na}_2\text{CoP}_2\text{O}_7$	10
Table 2.1.1	Li-ion batteries vs. Na-ion batteries.....	24
Table 2.4.1	Comparison of a flexible LIB with a traditional battery. [2.29]	36
Table 4.2.1	Atomic ratio of Na, Fe, and P in each B- $\text{Na}_2\text{FeP}_2\text{O}_7/\text{C}$ and M- $\text{Na}_2\text{FeP}_2\text{O}_7$ -NPs/C by ICP analysis.....	78
Table 4.2.2	Discharge capacities of B- $\text{Na}_2\text{FeP}_2\text{O}_7/\text{C}$ and M- $\text{Na}_2\text{FeP}_2\text{O}_7$ -NPs/C at different rates of 0.1, 1 and 10 C obtained from Figure 4.1.19.	79
Table 4.3.1	Atomic ratio of Na, Fe, and P in $\text{Na}_{3.12}\text{Fe}_{2.44}(\text{P}_2\text{O}_7)_2$ -NPs/C by ICP analysis	94
Table 4.3.2	Atomic ratio of Na, Fe, and P in $\text{Na}_{3.12}\text{Fe}_{2.44}(\text{P}_2\text{O}_7)_2$ -NPs/C/rGO by ICP analysis.	108
Table 4.3.3	Comparison of the electrochemical performance with various reported $\text{Na}_2\text{FeP}_2\text{O}_7$ - and $\text{Na}_{3.12}\text{Fe}_{2.44}(\text{P}_2\text{O}_7)_2$ -based cathode materials for NIBs.	109
Table 5.2.1	Phase diagram of $\text{Na}_{2-x}\text{Co}_{1+x}\text{P}_2\text{O}_7$ synthesized by solid-state	

reaction obtained from XRD patterns in Figure 5.2.1, 5.2.2 and 5.2.3 (holding time: 1 h).....	126
Table 5.2.2 Phase diagram of $\text{Na}_{2-2x}\text{Co}_{1+x}\text{P}_2\text{O}_7$ synthesized by solid-state reaction obtained from XRD patterns in Figure 5.2.4 and 5.2.5 (holding time: 6 h).....	133
Table 5.2.3 Atomic ratio of Na, Co and P in each $\text{Na}_2\text{CoP}_2\text{O}_7$, $\text{Na}_{1.8}\text{Co}_{1.1}\text{P}_2\text{O}_7$ and $\text{Na}_{1.6}\text{Co}_{1.2}\text{P}_2\text{O}_7$ synthesized at 500 °C for 1 h, 600 °C for 1 h and 680 °C for 6 h, respectively, by ICP analysis.....	134
Table 5.3.1 Phase diagram of $\text{Na}_{2-2x}\text{Co}_{1+x}\text{P}_2\text{O}_7$ -NPs/C synthesized by sol-gel method obtained from XRD patterns in Figure 5.3.1, 5.3.2 and 5.3.3.	141
Table 5.3.2 Atomic ratio of Na, Co and P in each $\text{Na}_2\text{CoP}_2\text{O}_7$ -NPs/C, $\text{Na}_{1.8}\text{Co}_{1.1}\text{P}_2\text{O}_7$ -NPs/C and $\text{Na}_{1.6}\text{Co}_{1.2}\text{P}_2\text{O}_7$ -NPs/C synthesized at 600 °C for 1 h, 600 °C for 3 h and 600 °C for 3 h, respectively, by ICP analysis.....	142

List of Figures

Figure 1.1.1	Environmental and energy problems induced by use of fossil fuels. Image is from internet website (http://www.climate-change-knowledge.org/climate-change.html).....	11
Figure 1.1.2	Comparison of the well-known practical rechargeable batteries in terms of volumetric energy density vs. gravimetric energy density. [1.3]	12
Figure 1.1.3	Voltage-specific capacity plots of cathode materials for NIBs. [1.35]	13
Figure 2.1.1	Schematic illustration of a typical Li-ion battery composed of positive electrode (cathode), negative electrode (anode), electrolyte and separator. The charging and discharging cycles are achieved through the exchange of Li-ions between the positive and negative electrode.....	25
Figure 2.3.1	Schematic illustration of nanoparticles synthesis by top-down or bottom-up physical or chemical methods.....	33
Figure 3.2.1	(a-b) High- and low-magnification FESEM images of A-Na ₂ FeP ₂ O ₇ -NPs/C. (c-d) High- and low-magnification FESEM images of A-Na ₂ FeP ₂ O ₇ -NPs/C after ball milling. (e-f) High- and low-magnification FESEM images of M-Na ₂ FeP ₂ O ₇ -NPs/C.....	46

Figure 3.2.2	FESEM image of Na ₂ FeP ₂ O ₇ -NPs/C surface after heat treatment at 600 °C for 6 h	47
Figure 3.2.3	FESEM image of Na ₂ FeP ₂ O ₇ -NPs/C synthesized by a sol-gel method with low amounts of citric acid.	48
Figure 3.2.4	XRD patterns of B-Na ₂ FeP ₂ O ₇ (bottom), A-Na ₂ FeP ₂ O ₇ -NPs/C (middle), and M-Na ₂ FeP ₂ O ₇ -NPs/C (top).....	49
Figure 3.2.5	(a-b) High- and low-magnification FESEM images of A-Na ₂ CoP ₂ O ₇ -NPs/C. (c-d) High- and low-magnification FESEM images of M-Na ₂ CoP ₂ O ₇ -NPs/C.....	52
Figure 3.2.6	(a-b) High- and low-magnification FESEM images of A-Na ₂ NiP ₂ O ₇ -NPs/C. (c-d) High- and low-magnification FESEM images of M-Na ₂ NiP ₂ O ₇ -NPs/C.	53
Figure 3.2.7	(a-b) High- and low-magnification FESEM images of Na ₂ MnP ₂ O ₇ /C.	54
Figure 3.2.8	XRD patterns of (a) Na ₂ CoP ₂ O ₇ -NPs/C, (b) Na ₂ NiP ₂ O ₇ -NPs/C (middle), and (c) Na ₂ MnP ₂ O ₇ /C.	55
Figure 3.2.9	Nitrogen adsorption-desorption isotherms and their pore size distributions (inset) of A-Na ₂ FeP ₂ O ₇ -NPs/C and M-Na ₂ FeP ₂ O ₇ -NPs/C.....	60
Figure 3.2.10	Nitrogen adsorption-desorption isotherms of (a) M-Na ₂ CoP ₂ O ₇ -NPs/C and (b) M-Na ₂ NiP ₂ O ₇ -NPs/C.....	61
Figure 3.2.11	Digital photographs of B-Na ₂ FeP ₂ O ₇ /C, A-Na ₂ FeP ₂ O ₇ -NPs/C	

and M-Na ₂ FeP ₂ O ₇ -NPs/C powder in glass 4 ml vials (1 g each).	
Inset shows the FESEM image of B-Na ₂ FeP ₂ O ₇ /C.....	62
Figure 3.2.12 TGA (weight loss) curves of A-Na ₂ FeP ₂ O ₇ -NPs/C and M-Na ₂ FeP ₂ O ₇ -NPs/C.....	63
Figure 3.2.13 (a-b) Low-and high-resolution TEM images of M-Na ₂ FeP ₂ O ₇ -NPs/C and (c) reduced FFT of the area enclosed in the square in (b).	64
Figure 3.2.14 TEM EDS elemental mapping of M-Na ₂ FeP ₂ O ₇ -NPs/C.	65
Figure 4.2.1 Cyclic voltammetry of B-Na ₂ FeP ₂ O ₇ /C and M-Na ₂ FeP ₂ O ₇ -NPs/C at a scan rate of 0.03 mV s ⁻¹	80
Figure 4.2.2 2 nd and 5 th galvanostatic voltage profiles of B-Na ₂ FeP ₂ O ₇ /C and M-Na ₂ FeP ₂ O ₇ -NPs/C at 0.05 C.	81
Figure 4.2.3 Specific capacities of B-Na ₂ FeP ₂ O ₇ /C (0.2 C), A-Na ₂ FeP ₂ O ₇ -NPs/C (0.05 C) and M-Na ₂ FeP ₂ O ₇ -NPs/C (0.2 C).	82
Figure 4.2.4 XRD patterns of M-Na ₂ FeP ₂ O ₇ -NPs/C before cycling and after 100 cycles.	83
Figure 4.2.5 Comparison of rate capability of B-Na ₂ FeP ₂ O ₇ /C and M-Na ₂ FeP ₂ O ₇ -NPs/C at different rates of 0.1, 1 and 10 C.	84
Figure 4.2.6 Nyquist plots for B-Na ₂ FeP ₂ O ₇ /C and Na ₂ FeP ₂ O ₇ -NPs/C at (a) 2 nd and (b) 10 th charged and discharged states at 3.0 V.....	85
Figure 4.2.7 Rate capability of M-Na ₂ FeP ₂ O ₇ -NPs/C at different rates from 0.1 to 60 C.	86

Figure 4.2.8	Comparison of rate performance to the recently results in the literature for $\text{Na}_2\text{FeP}_2\text{O}_7$	87
Figure 4.2.9	Rate capability of $\text{Na}_2\text{FeP}_2\text{O}_7$ -NPs/C with various ratios of active material, carbon black and binder at different rate from 0.1 to 10 C.....	88
Figure 4.2.10	Rate capability of $\text{Na}_2\text{FeP}_2\text{O}_7$ -NPs/C w with different loading of active material at different rate from 0.1 to 10 C	89
Figure 4.2.11	Long-term cyclability of M- $\text{Na}_2\text{FeP}_2\text{O}_7$ -NPs/C at both 10 and 60 C	90
Figure 4.3.1	(a-b) High- and low-magnification FESEM images of M- $\text{Na}_{3.12}\text{Fe}_{2.44}(\text{P}_2\text{O}_7)_2$ -NPs/C	95
Figure 4.3.2	XRD pattern of $\text{Na}_{3.12}\text{Fe}_{2.44}(\text{P}_2\text{O}_7)_2$ -NPs/C	96
Figure 4.3.3	Cyclic voltammetry of $\text{Na}_{3.12}\text{Fe}_{2.44}(\text{P}_2\text{O}_7)_2$ -NPs/C at a scan rate of 0.05 mV s^{-1}	97
Figure 4.3.4	Comparison of specific capacity between $\text{Na}_2\text{FeP}_2\text{O}_7$ -NPs/C and $\text{Na}_{3.12}\text{Fe}_{2.44}(\text{P}_2\text{O}_7)_2$ -NPs/C at 0.2 C	98
Figure 4.3.5	Comparison of rate capability between $\text{Na}_2\text{FeP}_2\text{O}_7$ -NPs/C and $\text{Na}_{3.12}\text{Fe}_{2.44}(\text{P}_2\text{O}_7)_2$ -NPs/C from 0.1 to 10 C.....	99
Figure 4.3.6	GITT and corresponding QOCP curves of the $\text{Na}_2\text{FeP}_2\text{O}_7$ -NPs/C and $\text{Na}_{3.12}\text{Fe}_{2.44}(\text{P}_2\text{O}_7)_2$ -NPs/C	100
Figure 4.3.7	Calculated sodium diffusion coefficients of the $\text{Na}_2\text{FeP}_2\text{O}_7$ -NPs/C and $\text{Na}_{3.12}\text{Fe}_{2.44}(\text{P}_2\text{O}_7)_2$ -NPs/C (a) at charged and (b)	

discharged states.....	101
Figure 4.3.8 Low- and High-magnification FESEM images of M- $\text{Na}_{3.12}\text{Fe}_{2.44}(\text{P}_2\text{O}_7)_2\text{-NPs/C/rGO}$	110
Figure 4.3.9 (a) TEM image of $\text{Na}_{3.12}\text{Fe}_{2.44}(\text{P}_2\text{O}_7)_2\text{-NPs/C/rGO}$. (b) TEM image of GO. (c) TEM image of $\text{Na}_{3.12}\text{Fe}_{2.44}(\text{P}_2\text{O}_7)_2\text{-}$ NPs/C/rGO and HR image obtained from the marked region in (c).....	111
Figure 4.3.10 XRD pattern of $\text{Na}_{3.12}\text{Fe}_{2.44}(\text{P}_2\text{O}_7)_2\text{-NPs/C/rGO}$	112
Figure 4.3.11 C 1s level XPS spectra of $\text{Na}_{3.12}\text{Fe}_{2.44}(\text{P}_2\text{O}_7)_2\text{-NPs/C/rGO}$..	113
Figure 4.3.12 Nitrogen adsorption-desorption isotherms of $\text{Na}_{3.12}\text{Fe}_{2.44}(\text{P}_2\text{O}_7)_2\text{-NPs/C}$ and $\text{Na}_{3.12}\text{Fe}_{2.44}(\text{P}_2\text{O}_7)_2\text{-NPs/C/rGO}$	114
Figure 4.3.13 TGA (weight loss) curves of $\text{Na}_{3.12}\text{Fe}_{2.44}(\text{P}_2\text{O}_7)_2\text{-NPs/C}$ and $\text{Na}_{3.12}\text{Fe}_{2.44}(\text{P}_2\text{O}_7)_2\text{-NPs/C/rGO}$	115
Figure 4.3.14 (a) Voltage–capacity profiles of $\text{Na}_{3.12}\text{Fe}_{2.44}(\text{P}_2\text{O}_7)_2\text{-NPs/C/rGO}$. (b) Comparison of rate performance between $\text{Na}_{3.12}\text{Fe}_{2.44}(\text{P}_2\text{O}_7)_2\text{-NPs/C}$ and $\text{Na}_{3.12}\text{Fe}_{2.44}(\text{P}_2\text{O}_7)_2\text{-NPs/C/rGO}$ from 0.1 to 10 C.....	116
Figure 4.3.15 Nyquist plots for $\text{Na}_{3.12}\text{Fe}_{2.44}(\text{P}_2\text{O}_7)_2\text{-NPs/C}$ and $\text{Na}_{3.12}\text{Fe}_{2.44}(\text{P}_2\text{O}_7)_2\text{-NPs/C/rGO}$ at the 1 st , 5 th and 10 th charged states.....	117
Figure 4.3.16 Long-term cyclability of $\text{Na}_{3.12}\text{Fe}_{2.44}(\text{P}_2\text{O}_7)_2\text{-NPs/C/rGO}$ at 10	

C.....	118	
Figure 5.2.1	XRD patterns of $\text{Na}_2\text{CoP}_2\text{O}_7$ with various annealing temperature from 500 to 650 °C for 1 h.....	127
Figure 5.2.2	XRD patterns of $\text{Na}_{1.8}\text{Co}_{1.1}\text{P}_2\text{O}_7$ with various annealing temperature from 500 to 650 °C for 1 h.....	128
Figure 5.2.3	XRD patterns of $\text{Na}_{1.6}\text{Co}_{1.2}\text{P}_2\text{O}_7$ with various annealing temperature from 500 to 680 °C for 1 h.....	129
Figure 5.2.4	XRD patterns of $\text{Na}_{1.8}\text{Co}_{1.1}\text{P}_2\text{O}_7$ annealed at 600 °C with increasing holding times from 1 to 6 h.....	135
Figure 5.2.5	XRD patterns of $\text{Na}_{1.6}\text{Co}_{1.2}\text{P}_2\text{O}_7$ annealed at 650 and 680 °C with increasing holding times from 1 to 6 h.....	136
Figure 5.3.1	XRD patterns of $\text{Na}_2\text{CoP}_2\text{O}_7$ -NPs/C. HT condition of (a) 600 °C for 1 h and (b) 600 °C for 3 h.....	143
Figure 5.3.2	XRD patterns of $\text{Na}_{1.8}\text{Co}_{1.1}\text{P}_2\text{O}_7$ -NPs/C. HT condition of (a) 600 °C for 1 h, (b) 600 °C for 3 h, (c) 600 °C for 6 h, and (d) 600-650 °C for 3-6 h.....	144
Figure 5.3.3	(a) High- and (b) low-magnification FESEM images of B- $\text{Na}_2\text{CoP}_2\text{O}_7$ synthesized by a solid-state reaction.....	145
Figure 5.3.4	XRD patterns of $\text{Na}_{1.6}\text{Co}_{1.2}\text{P}_2\text{O}_7$ -NPs/C. HT condition of (a) 600 °C for 1 h and (b) 600 °C for 3 h.....	146
Figure 5.3.5	High- and low-magnification FESEM images of (a-b) $\text{Na}_{1.8}\text{Co}_{1.1}\text{P}_2\text{O}_7$ -NPs/C and (c-d) $\text{Na}_{1.6}\text{Co}_{1.2}\text{P}_2\text{O}_7$ -NPs/C.....	147

Figure 5.3.6	XRD pattern of B-Na _{1.8} Co _{1.1} P ₂ O ₇ /C synthesized by (a) 1-step solid-state reaction with glucose as a carbon source, and (b) 2-step solid-state reaction with graphite as a carbon source...153
Figure 5.3.7	Galvanostatic voltage profiles of B-Na _{1.8} Co _{1.1} P ₂ O ₇ /C at 0.2 C.....154
Figure 5.3.8	Cyclic voltammetry of (a) Na ₂ CoP ₂ O ₇ -NPs/C, (b) Na _{1.8} Co _{1.1} P ₂ O ₇ -NPs/C and (c) Na _{1.6} Co _{1.2} P ₂ O ₇ -NPs/C at a scan rate of 0.05 mV s ⁻¹155
Figure 5.3.9	(a) Comparison of 5 th cyclic voltammetry among Na ₂ CoP ₂ O ₇ -NPs/C, Na _{1.8} Co _{1.1} P ₂ O ₇ -NPs/C and Na _{1.6} Co _{1.2} P ₂ O ₇ -NPs/C at a scan rate of 0.05 mV s ⁻¹ . (b) Expansion of CV in the range of 3.8-4.1 V.....156
Figure 5.3.10	Galvanostatic voltage profiles of Na ₂ CoP ₂ O ₇ -NPs/C at 0.2 C.....157
Figure 5.3.11	Galvanostatic voltage profiles of Na _{1.8} Co _{1.1} P ₂ O ₇ -NPs/C at 0.2 C.....158
Figure 5.3.12	Galvanostatic voltage profiles of Na _{1.6} Co _{1.2} P ₂ O ₇ -NPs/C at 0.2 C.....159
Figure 5.3.13	Galvanostatic voltage profiles of Na _{1.8} Co _{1.1} P ₂ O ₇ -NPs/C charged to 120 mA h g ⁻¹ and discharged to 1.5 V at 0.2 C. .160
Figure 5.3.14	Comparison of discharge voltage profiles of Na _{1.8} Co _{1.1} P ₂ O ₇ -NPs/C charged to 100 and 120 mA h g ⁻¹ , respectively, at 10 th

and 20 th cycle.....	161
Figure 6.2.1 Schematic illustration of the fabrication of Na ₂ FeP ₂ O ₇ -NPs/C@PCC electrode.....	168
Figure 6.2.2 FESEM images of bare-CC.....	169
Figure 6.2.3 Digital photographs of (a) bare-CC and (b) UV-ozone-treated CC with water.....	170
Figure 6.2.4 FESEM images of (a) FeOOH@CC, (b) Fe ₃ O ₄ embedded in CC, and (e) PCC.....	171
Figure 6.3.1 Schematic illustration of the Na ₂ FeP ₂ O ₇ -NPs/C@PCC electrode.....	174
Figure 6.3.2 FESEM images of Na ₂ FeP ₂ O ₇ -NPs/C@PCC.....	175
Figure 6.3.3 EDS elemental mapping of Na ₂ FeP ₂ O ₇ -NPs/C@PCC.....	176
Figure 6.3.4 XRD patterns of commercial bare-CC and Na ₂ FeP ₂ O ₇ -NPs/C@PCC.....	177
Figure 6.3.5 Digital photograph of flexible Na ₂ FeP ₂ O ₇ -NPs/C@PCC electrode.....	178
Figure 6.3.6 Rate capability of Na ₂ FeP ₂ O ₇ -NPs/C@PCC.....	181
Figure 6.3.7 Long-term cyclability of Na ₂ FeP ₂ O ₇ -NPs/C@PCC at 2000 th cycle.....	182

Chapter 1. Introduction

1.1 Overview: Rechargeable Batteries for Energy Storage Systems

Ever-increasing demands for energy production and energy storage in order to fulfill the requirements of modern societies have led to a rapid global consumption of fossil fuels (coal, oil and gas etc.) mainly in power station and automobiles bringing out various environmental issues, such as air pollution, emission of radioactive substances and CO₂ emissions-related global warming described in Figure 1.1.1. [1.1-1.3] So, environmental-friendly energy production and energy storage have become important issues at the present time. Over several decades, solar, wind, tidal, biomass, geothermal and hydroelectric energy resources with less-polluting, less-harmful, and abundant alternatives have been studies extensively. For the effective management of these renewable energy as well as conventional energy from fossil fuels and nuclear reactions, it is absolutely essential to mount energy storage systems (ESSs) converting these energy to other forms so it can be used when needed. [1.3,1.4]

Electrochemical devices such as rechargeable batteries are one of the most attractive forms to store both conventional energy and renewable energy. Also, it is facile to convert other energy forms such as chemical and kinetic energy. Since the 19th century, many researches about rechargeable batteries

have been studied to date. However, only a few materials have linked to great success in rechargeable batteries due to the ability to reverse the electrochemical reactions at both sides of the electrodes. Typical rechargeable batteries are Pb-acid battery, Ni-Cd battery, Ni-metal hydride battery, and particularly, Li-ion battery (Table 1.1.1 and Figure 1.1.2). [1.3,1.5]

Among the rechargeable batteries, since Sony successfully commercialized in Li-ion batteries (LIBs) in the 1990s, rechargeable LIBs have been developed in recent years as power sources in energy storage and conversion. From compact electronic equipment to electric vehicles and stationary energy storage systems, these batteries have been widely used because of their high power and energy density, little memory effect together with long operating life and good environmental compatibility. [1.6-1.9] Nevertheless, the large-scale demand for Li globally has caused a steep price increase owing to the lack of reserves and an uneven distribution of Li resources in the world, which restricts the use of LIBs in the automobile market and large-scale energy storage systems. [1.10,1.11] Long-term planning in the energy storage field is required to discover alternative materials that can resolve both the scaling and cost challenges. [1.12] Thus, use of low-cost and abundant materials is indispensable. Rechargeable Na-ion batteries (NIBs) are under consideration as one of the potential candidates for large scale electric energy storage such as automobiles (electrical vehicles, hybrid electrical vehicles, plug-in electrical vehicles) and grid-scale energy storage system (power station,

smart grid), because of unlimited global resources, abundant elements, and low cost of Na in contrast to Li. The cost per energy (kW h) that Na is able to provide can offer a tremendous advantage as a huge amount of Na is required for large scale applications. [1.9] In addition, the electrochemical behavior of Na-ion insertion/desertion on NIB cathode materials is relatively similar to those of Li-ions for LIB cathode materials, which makes it possible to use similar compounds for both LIB and NIB cathode systems. [1.10]. Therefore, the development of high-performance cathode materials is needed for their NIB application.

As cathode materials for LIBs, polyanionic compounds have been widely researched in the last decade, especially in phosphate-based compounds such as LiMPO₄ (M = transition metal) because of their long lifetime, low cost, environmental friendliness, and thermal stability. [1.13,1.14] Motived by this, NaMPO₄, which has a similar composition to LiMPO₄ has been researched, but it is believed to be inappropriate as a cathode material for NIBs so far, because of its electrochemical inactivity in Na cells (in the case of thermodynamically stable maricite structure) or poor Na-ion insertion kinetics (in the case of metastable olivine structure). [1.15] Recently, various polyanionic cathode materials such as Na₂FePO₄F, [1.16] Na₃V₂(PO₄)₃, [1.17] Na₃V₂(PO₄)₂F₃ , [1.18] Na₄Fe₃(PO₄)₂(P₂O₇), [1.19] NaVPO₄F, [1.20] Na₇V₄(P₂O₇)₄(PO₄), [1.21] and NaVOPO₄, [1.22] have been reported.

With the successful development on lithium transition metal

pyrophosphates ($\text{Li}_2\text{MP}_2\text{O}_7$; M = transition metal) series as a cathodes for LIBs, Na-based transition metal pyrophosphates, $\text{Na}_2\text{MP}_2\text{O}_7$ (M = transition metal), has been in the spotlight as a cathode material in NIBs. [1-10] It has all the advantages of phosphate-based compounds. Additionally, in the case of $\text{Na}_2\text{FeP}_2\text{O}_7$, it exhibits a capacity of $\sim 90 \text{ mA h g}^{-1}$ with good rate capability and cyclability compared to other cathode materials, which originates from its open frameworks that can facilitate efficient diffusion of Na ions for battery operation, making it economically feasible for large-scale devices. [1.23-1.27] Since first being reported in 2012, some characteristics of $\text{Na}_2\text{FeP}_2\text{O}_7$, *i.e.*, crystal and electrochemical information for non-aqueous NIB cathodes through solid-state reaction [1.23-1.25] and crystallization process of glass compound [1.26] have been studied. Longoni et al. synthesized $\text{Na}_2\text{FeP}_2\text{O}_7/\text{MWCNT}$ composites showing good rate capability. [1.27]

As mentioned above, although $\text{Na}_2\text{FeP}_2\text{O}_7$ exhibits an excellent rate capability and cyclability, the electrochemical properties of only micron- or submicron-sized particles have been investigated. Hence, there still remain many topics to study on the advanced battery performance in $\text{Na}_2\text{FeP}_2\text{O}_7$. In this respect, synthesis of nano-sized or nano-structured $\text{Na}_2\text{FeP}_2\text{O}_7$ electrodes is the best and well-known strategy for improving the battery performance of $\text{Na}_2\text{FeP}_2\text{O}_7$. [1.7] However, it is a challenge to synthesize $\text{Na}_2\text{FeP}_2\text{O}_7$ nanomaterials because there have been only a few reports on the synthesis of $\text{Li}_2\text{MP}_2\text{O}_7$ series nanomaterials. In addition to this, if the $\text{Na}_2\text{FeP}_2\text{O}_7$

nanomaterials are incorporated with carbon, it could improve the low electrical conductivity originating from the polyanionic structure, which can lead to high performance $\text{Na}_2\text{FeP}_2\text{O}_7$ electrodes.

Meanwhile, According to the previous researches, both $\text{Na}_2\text{FeP}_2\text{O}_7$ and $\text{Na}_{3.12}\text{Fe}_{2.44}(\text{P}_2\text{O}_7)_2$ show similar electrochemical behavior as a NIB cathode material resulting from the similarity of crystal structure between them. [1.25,1.28] Their crystal information is tabulated in Table 1.1.2 However, more electrochemical $\text{Fe}^{2+}/\text{Fe}^{3+}$ redox reaction can occur in $\text{Na}_{3.12}\text{Fe}_{2.44}(\text{P}_2\text{O}_7)_2$ when charging/discharging, which results in higher theoretical capacity of $\text{Na}_{3.12}\text{Fe}_{2.44}(\text{P}_2\text{O}_7)_2$ (117 mA h g^{-1}) than that of $\text{Na}_2\text{FeP}_2\text{O}_7$ (97 mA h g^{-1}). For this reason, it is anticipated that $\text{Na}_{3.12}\text{Fe}_{2.44}(\text{P}_2\text{O}_7)_2$ exhibits higher practical energy density than $\text{Na}_2\text{FeP}_2\text{O}_7$ when applying for NIB electrode. In addition, $\text{Na}_{3.12}\text{Fe}_{2.44}(\text{P}_2\text{O}_7)_2$ nanomaterials incorporated with carbon can also lead to high performance $\text{Na}_{3.12}\text{Fe}_{2.44}(\text{P}_2\text{O}_7)_2$ electrode than $\text{Na}_2\text{FeP}_2\text{O}_7$ electrode.

In the case of $\text{Na}_2\text{CoP}_2\text{O}_7$, there have been addressed a few information about electrochemical properties when application in NIBs. It is known that $\text{Na}_2\text{CoP}_2\text{O}_7$ exists in three different structures; orthorhombic, tetragonal and triclinic polymorphs [1.29,1.30]. Among them, orthorhombic and triclinic polymorphs, also referred to as the “blue” and “rose” form, respectively, originated from their powder color, are generally synthesized by solid-state or wet-chemical synthetic processes. Orthorhombic polymorph shows the most thermodynamically stable phase in $\text{Na}_2\text{CoP}_2\text{O}_7$, while triclinic polymorph

shows metastable form compared to orthorhombic polymorph. Their crystal information is tabulated in Table 1.1.3.

According to a previous report, the orthorhombic polymorph (blue phase) $\text{Na}_2\text{CoP}_2\text{O}_7$ exhibits a discharge capacity of 75-80 mA h g⁻¹, but an average operating voltage of only 3.0 V (vs. Na/Na⁺), a value that is substantially lower than the commonly expected Co²⁺/Co³⁺ redox reaction potential. [1.31,1.32] In contrast, triclinic polymorph (rose phase) exhibits an high average operating voltage of 4.3 V (vs. Na/Na⁺), which is one of the NIB cathode materials which electrochemically reacts with Na-ions at the high voltage. [1.33-1.35] Therefore, it is important to synthesize rose phase $\text{Na}_2\text{CoP}_2\text{O}_7$, especially nano-sized rose phase $\text{Na}_2\text{CoP}_2\text{O}_7$ to improve its electrochemical performance similar to Fe-based pyrophosphate compounds.

Meanwhile, with the rapid development of flexible/bendable electronics, flexible batteries have been attracting great interest as a promising power source recently, such as such as wearable devices, rollup displays and bendable mobile phones. [1.36-1.38] For flexible electrodes, various carbon-based flexible substrates such as carbon paper, carbon cloth (CC), carbon nanotubes (CNTs), and graphene film have been used because of their porous network, cost-effectiveness, outstanding electrical conductivity, and good chemical and electrochemical stability. [1.39-1.41] Among the various flexible substrates, CC not only displays excellent mechanical flexibility and strength compared to other carbon-based flexible substrates, it also serves as a three-dimensional

current collector, replacing traditional Cu or Al foil. [1.42] Hence, combining this CC with an active material through processes such as a facile dip-coating has been studied recently. [1.43-1.45]

Table 1.1.1 Summary of the practical rechargeable batteries. [3]

Rechargeable Battery	Cathode	Anode	Electrolyte	Voltage (V)	Cycle Life (#)
Pb-acid	PbO ₂	Pb	H ₂ SO ₄	2.1	<500
Ni-Cd	NiOOH	Cd	KOH	1.2	2000
Ni-Metal Hydride	NiOOH	Intermetallic Compound	KOH	1.2	500- 1000
Lithium-ion	LiCoO ₂	C (Graphite)	LiPF ₆	3.7	>1000

Table 1.1.2 Crystal information of $\text{Na}_2\text{FeP}_2\text{O}_7$ and $\text{Na}_{3.12}\text{Fe}_{2.44}(\text{P}_2\text{O}_7)_2$.

System	Space group	a	b	c	
$\text{Na}_2\text{FeP}_2\text{O}_7$	triclinic	P-1	6.449	9.482	10.993
$\text{Na}_{3.12}\text{Fe}_{2.44}(\text{P}_2\text{O}_7)_2$	triclinic	P-1	6.424	9.440	10.981

System	α	β	γ	V
$\text{Na}_2\text{FeP}_2\text{O}_7$	64.85	86.24	73.13	581.05
$\text{Na}_{3.12}\text{Fe}_{2.44}(\text{P}_2\text{O}_7)_2$	64.77	86.21	73.13	575.19

Table 1.1.3 Crystal information of orthorhombic and triclinic polymorph $\text{Na}_2\text{CoP}_2\text{O}_7$.

	System	Space group	a	b	c
$\text{Na}_2\text{CoP}_2\text{O}_7$	orthorhombic	P21cn	7.713	10.271	15.378
	triclinic	P-1	9.735	10.940	12.289
	System	α	β	γ	V
$\text{Na}_2\text{CoP}_2\text{O}_7$	orthorhombic	90	90	90	1218.25
	triclinic	148.78	121.76	68.38	566.80

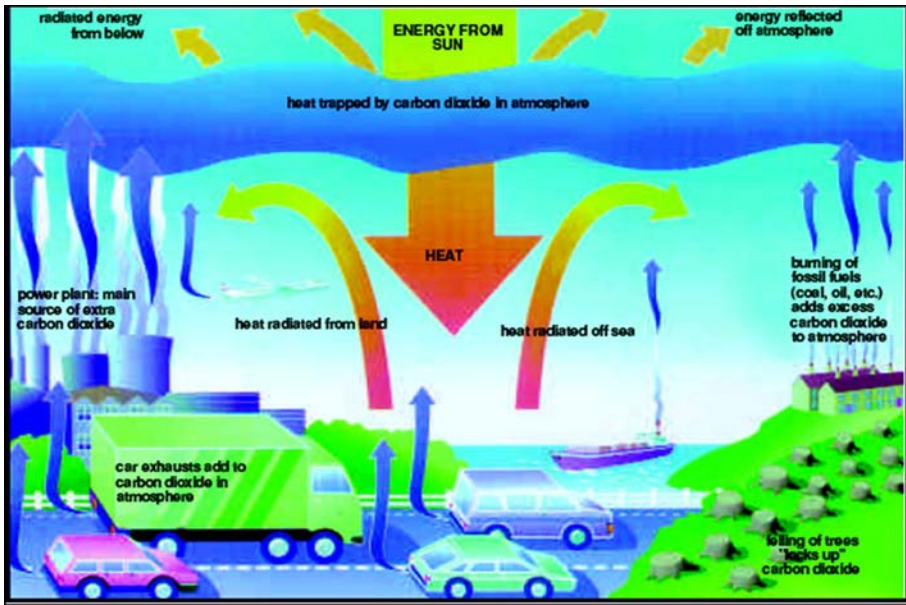


Figure 1.1.1 Environmental and energy problems induced by use of fossil fuels.

Image is from internet website (<http://www.climate-change-knowledge.org/climate-change.html>).

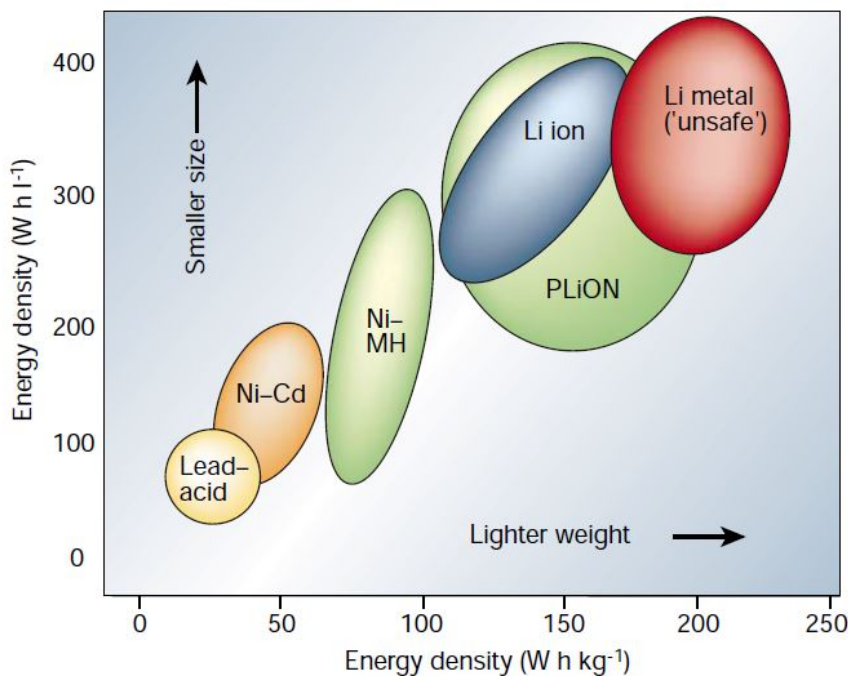


Figure 1.1.2 Comparison of the well-known practical rechargeable batteries in terms of volumetric energy density vs. gravimetric energy density. [1.3]

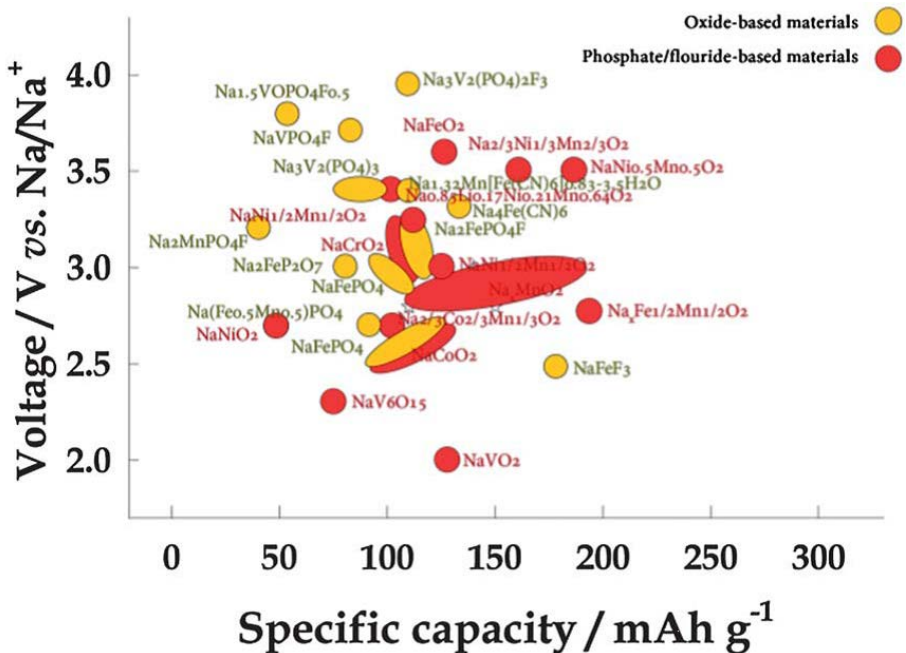


Figure 1.1.3 Voltage-specific capacity plots of cathode materials for NIBs.

[1.35]

1.2 Aim and Strategies

The objective of this thesis is to develop the high-performance cathode materials in NIBs. For this, $\text{Na}_2\text{MP}_2\text{O}_7/\text{C}$ nanocomposites ($\text{M} = \text{Fe, Co}$) are synthesized and their electrochemical performance for high-performance cathode materials in NIBs is evaluated. Also, their application to free-standing electrode combining the $\text{Na}_2\text{FeP}_2\text{O}_7\text{-NPs/C}$ and porous carbon cloth for possible flexible NIBs is investigated.

For high-performance electrode in NIBs, this thesis suggests the following strategies. The first is nano-engineering. Nano technology in battery electrodes can improve electrochemical performance of capacity, rate capability and cyclability. Also, particle size reduction to nanoscale under tens of nanometer can induce metastable phase to be a majority product of nanoscale samples. The second is compositional engineering. In Fe-based pyrophosphate, Fe-excess, followed by Na-deficiency for charge balance, compound can increase more $\text{Fe}^{2+}/\text{Fe}^{3+}$ redox reaction, resulting in a improvement of energy density. Also, Co instead of Fe can increase the operating voltage, delivering an increase of energy density. The final is fabrication of free-standing electrode by incorporating this high-performance cathode material with flexible electrode for high-performance flexible electrode.

In chapter 2, the basic principle of LIB, NIB and their literature review,

especially about the polyanionic cathode materials for NIB are investigated.

Also, the advantages of nanotechnologies for battery electrodes are examined.

Finally, status of flexible/bendable electronics are reviewed.

In chapter 3, general synthetic strategy for synthesizing $\text{Na}_2\text{MP}_2\text{O}_7/\text{C}$ nanocomposites by a sol-gel method are described in detail. Characterization of these nanocomposites is discussed.

In chapter 4, electrochemical performance of Fe-based pyrophosphate nanocomposites, $\text{Na}_2\text{FeP}_2\text{O}_7$ and $\text{Na}_{3.12}\text{Fe}_{2.44}(\text{P}_2\text{O}_7)_2$, is measured and evaluated in terms of nano-engineering and compositional engineering.

In chapter 5, phase dependence of Co-based pyrophosphate compounds is established in terms of annealing temperature, holding time and Na/Co ration in compound. Also, synthesizing metastable rose phase $\text{Na}_{2-2x}\text{Co}_{1+x}\text{P}_2\text{O}_7/\text{C}$ nanocomposites through the particle size reduction to nanoscale and evaluating their electrochemical performance.

In chapter 6, free-standing electrode ($\text{Na}_2\text{FeP}_2\text{O}_7$ -NPs/C on porous carbon cloth) without any conductive agents and polymeric binders is fabricated by a facile dip-coating process, and their electrochemical performance is measured for high-performance flexible NIBs

1.3 Bibliography

- [1.1] D. Larcher, J.-M. Tarascon, *Nature Chem.*, **2015**, *7*, 19-29.
- [1.2] B. Scrosati, J. Hassoun, Y.-K. Sun, *Energy Environ. Sci.*, **2011**, *4*, 3287.
- [1.3] Y. Abu-Lebdeh, I. Davidson, Nanotechnology for Lithium-Ion Batteries, Springer.
- [1.4] T. R. Cook, D. K. Dogutan, S. Y. Reece, Y. Surendranath, T. S. Teets, D. G. Nocera, *Chem. Rev.*, **2010**, *110*, 6474-6502.
- [1.5] Z. Yang, J. Zhang, M. C. Kintner-Meyer, X. Lu, D. Choi, J. P. Lemmon, J. Liu, *Chem. Rev.*, **2011**, *111*, 3577-3613.
- [1.6] P. Poizot, S. Laruelle, S. Gruegeon, L. Dupont, J.-M. Tarascon, *Nature*, **2000**, *407*, 496-499.
- [1.7] G.-N. Zhu, Y.-G. Wang, Y.-Y. Xia, *Energy Environ. Sci.*, **2012**, *5*, 6652-6667.
- [1.8] M. Armand, J.-M. Tarascon, *Nature*, **2008**, *451*, 652-657.
- [1.9] L. P. Wang, L. Yu, X. Wang, M. Srinivasan, Z. J. Xu, *J. Mater. Chem. A*, **2015**, *3*, 9353-9378.
- [1.10] P. Barpanda, S.-i. Nishimura, A. Yamada, *Adv. Energy Mater.*, **2012**, *2*, 841-859.
- [1.11] M. D. Slater, D. Kim, E. Lee, C. S. Johnson, *Adv. Funct. Mater.*, **2013**, *23*, 947-958.

- [1.12] C. Wadia, P. Albertus, V. Srinivasan, *J. Power Sources*, **2011**, *196*, 1593-1598.
- [1.13] Z. Bi, X. Zhang, W. He, D. Min, W. Zhang, *RSC Adv.*, **2013**, *3*, 19744-19751.
- [1.14] Z. Gong, Y. Yang, *Energy Environ. Sci.*, **2011**, *4*, 3223.
- [1.15] Y. Zhu, Y. Xu, Y. Liu, C. Luo, C. Wang, *Nanoscale*, **2013**, *5*, 780-787.
- [1.16] B. L. Ellis, W. R. Makahnouk, Y. Makimura, K. Toghill, L. F. Nazar, *Nat. Mater.*, **2007**, *6*, 749-753.
- [1.17] Z. Jian, L. Zhao, H. Pan, Y.-S. Hu, H. Li, W. Chen, L. Chen, *Electrochem. Commun.*, **2012**, *14*, 86-89.
- [1.18] K. Chihara, A. Kitajou, I. D. Gocheva, S. Okada, J.-i. Yamaki, *J. of Power Sources*, **2013**, *227*, 80-85.
- [1.19] H. Kim, I. Park, S. Lee, H. Kim, K.-Y. Park, Y.-U. Park, H. Kim, J. Kim, H.-D. Lim, W.-S. Yoon, K. Kang, *Chem. of Mater.*, **2013**, *25*, 3614-3622.
- [1.20] Y. Lu, S. Zhang, Y. Li, L. Xue, G. Xu, X. Zhang, *J. of Power Sources*, **2014**, *247*, 770-777.
- [1.21] C. Deng, S. Zhang, *ACS Appl. Mater. Interf.*, **2014**, *6*, 9111-9117.
- [1.22] J. Song, M. Xu, L. Wang, J. B. Goodenough, *Chem. Commun.*, **2013**, *49*, 5280-5282.

- [1.23] H. Kim, R. A. Shakoor, C. Park, S. Y. Lim, J.-S. Kim, Y. N. Jo, W. Cho, K. Miyasaka, R. Kahraman, Y. Jung, J. W. Choi, *Adv. Funct. Mater.*, **2013**, *23*, 1147-1155.
- [1.24] P. Barpanda, G. Liu, C. D. Ling, M. Tamaru, M. Avdeev, S.-C. Chung, Y. Yamada, A. Yamada, *Chem. Mater.*, **2013**, *25*, 3480-3487.
- [1.25] P. Barpanda, T. Ye, S.-i. Nishimura, S.-C. Chung, Y. Yamada, M. Okubo, H. Zhou, A. Yamada, *Electrochim. Commun.*, **2012**, *24*, 116-119.
- [1.26] T. Honma, N. Ito, T. Togashi, A. Sato, T. Komatsu, *J. Power Sources*, **2013**, *227*, 31-34.
- [1.27] G. Longoni, J. E. Wang, Y. H. Jung, D. K. Kim, C. M. Mari, R. Ruffo, *J. Power Sources*, **2016**, *302*, 61-69.
- [1.28] K.-H. Ha, S. H. Woo, D. Mok, N.-S. Choi, Y. Park, S. M. Oh, Y. Kim, J. Kim, J. Lee, L. F. Nazar, K. T. Lee, *Adv. Energy Mater.*, **2013**, *3*, 770-776.
- [1.29] F. Sanz, C. Parada, J. M. Rojo, C. Ruiz-Valero, R. Saez-Puche, *J. Solid State Chem.*, **1999**, *145*, 604-611.
- [1.30] G. S. Gopalakrishna, M. J. Mahesh, K. G. Ashamanjari, J. Shashidharaprasad, *J. Crystal. Growth*, **2005**, *281*, 604-610.
- [1.31] P. Barpanda, J. Lu, T. Ye, M. Kajiyama, S.-C. Chung, N. Yabuuchi, S. Komaba, A. Yamada, *RSC Adv.*, **2013**, *3*, 3857-3860.

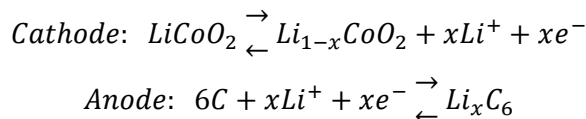
- [1.32] G. Hautier, A. Jain, S. P. Ong, B. Kang, C. Moore, R. Doe, G. Ceder, *Chem. Mater.*, **2011**, *23*, 3495-3508.
- [1.33] H. Kim, C. S. Park, J. W. Choi, Y. Jung, *Angew. Chem. Int. Ed.*, **2016**, *55*, 6662-6666.
- [1.34] H. Kim, C. S. Park, J. W. Choi, Y. Jung, *Chem. Mater.*, **2016**, *28*, 6724-6730.
- [1.35] S. Y. Hong, Y. Kim, Y. Park, A. Choi, N.-S. Choi, K. T. Lee, *Energy Environ. Sci.*, **2013**, *6*, 2067-2081.
- [1.36] B. D. Gates, *Science*, **2009**, *323*, 1566-1567.
- [1.37] S. Bauer, *Nat. Mater.*, **2013**, *12*, 871-872.
- [1.38] X. Wang, X. Lu, B. Liu, D. Chen, Y. Tong, G. Shen, *Adv. Mater.*, **2014**, *26*, 4763-4782.
- [1.39] A. Marschilok, C.-Y. Lee, A. Subramanian, K. J. Takeuchi, E. S. Takeuchi, *Energy Environ. Sci.*, **2011**, *4*, 2943-2951.
- [1.40] L. Hu, Y. Cui, *Energy Environ. Sci.*, **2012**, *5*, 6423-6435.
- [1.41] G. Zhou, F. Li, H.-M. Cheng, *Energy Environ. Sci.*, **2014**, *7*, 1307-1338.
- [1.42] M.-S. Balogun, W. Qiu, F. Lyu, Y. Luo, H. Meng, J. Li, W. Mai, L. Mai, Y. Tong, *Nano Energy*, **2016**, *26*, 446-455.
- [1.43] L. Hu, F. La Mantia, H. Wu, X. Xie, J. McDonough, M. Pasta, Y. Cui, *Adv. Energy Mater.*, **2011**, *1*, 1012-1017.
- [1.44] L. Hu, M. Pasta, F. L. Mantia, L. Cui, S. Jeong, H. D. Deshazer, J. W. Choi, S. M. Han, Y. Cui, *Nano. Lett.*, **2010**, *10*, 708-714.

[1.45] K. Jost, C. R. Perez, J. K. McDonough, V. Presser, M. Heon, G. Dion, Y. Gogotsi, *Energy Environ. Sci.*, **2011**, *4*, 5060-5067.

Chapter 2. Background and Literature Review

2.1 Li-Ion and Na-Ion Batteries

Rechargeable Li-ion batteries (LIBs) are electrochemical devices that converts chemical energy into electrical energy through the migration of Li-ions. Figure 2.1.1 shows the scheme of typical LIB illustrating its various components and the movement of Li ions. They are composed of positive electrode (cathode), negative electrode (anode), electrolyte and separator. Most commercialized material in cathode and anode in is a layered oxide such as LiCoO_2 , $\text{Li}(\text{Ni},\text{Mn},\text{Co})\text{O}_2$ and a graphitic carbon, respectively. The electrolyte consists of a Li salt (LiPF_6) dissolved in a mixture of non-aqueous, aprotic carbonate solvent. Li-ions move from the cathode to the anode through the ionically conducting electrolyte during charging, and in reverse during discharging. [2.1] The general electrochemical reaction in LIB during cycling is explained as follow.



During charging and discharging, electrical energy is stored and released in LIB, respectively.

The operating voltage of electrodes is determined as a function of the activity of Li ions, according to Nernst equation: [2.2]

$$V = V^0 - \frac{RT}{nF} \ln a_{Li+}$$

where, R is the universal gas constant, T is the temperature (K), and F is the Faraday constant.

In NIBs, Na-ions participate in electrochemical reaction instead of Li-ions. A brief comparison between Li and Na is tabulated in Table 2.1.1. [2.3,2.4] Despite some disadvantages of Na in terms of higher reducing potential than sodium ($V = -2.7$ V vs. S.H.E.) has over lithium ($V = -3.04$ V vs. S.H.E.), and its large ionic radius (R_{Li+} : 0.76 Å, R_{Na+} : 1.02 Å), the low cost and abundance of sodium resource can offer a tremendous advantages when a huge amount of alkali metal is required for large-scale EES applications.

For NIBs, cathodes is comprised of materials that can electrochemically react with Na-ions reversibly at a voltage greater than 2 V (vs. Na/Na^+). Materials reacting with Na-ions at lower operating voltages (< 2 V vs. Na/Na^+) are defined as anodes. The energy density of the NIBs can be maximized by increasing the cathode operating voltage, decreasing the anode operating voltage, increasing practical capacity and producing electrodes with high tap density. Cathodes for NIBs work best when they function as follows; the

volume change when sodiation/desodiation should be as negligible as possible for the materials (stability). Also, high rate capability (high power) and long-term cyclic stability (durability) are critical for high-performance NIBs. [2.3]

Table 2.1.1 Li-ion batteries vs. Na-ion batteries

Characteristics	Lithium (Li)	Sodium (Na)
Price (for carbonate)	\$5800/ton	\$250-300/ton
Deposites (Earth's crust)	Maldistribution (0.002-0.007%)	Infinite (2.6%; 6 th)
Weight	6.94 g mol ⁻¹	23.00 g mol ⁻¹
Voltage vs. S.H.E	-3.0 V	-2.7 V
Ionic radius	0.76 Å	1.02 Å

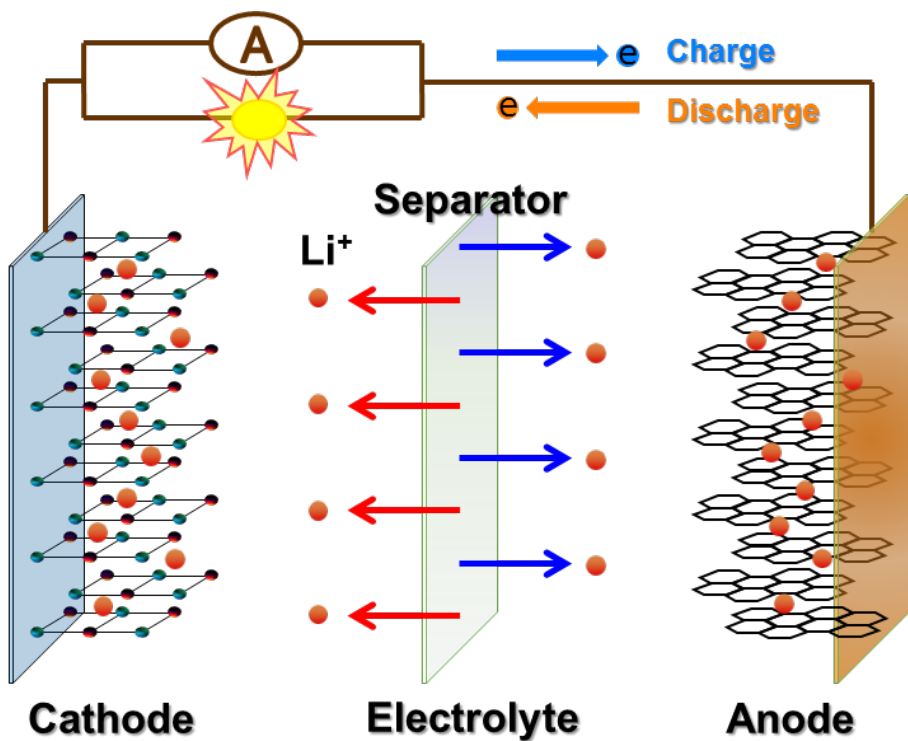


Figure 2.1.1 Schematic illustration of a typical Li-ion battery composed of positive electrode (cathode), negative electrode (anode), electrolyte and separator. The charging and discharging cycles are achieved through the exchange of Li-ions between the positive and negative electrode.

2.2 Polyanionic Cathode Materials for Na-Ion Battery

A variety of polyanionic compounds for NIB cathodes have been addressed such as phosphates, pyrophosphates, fluorophosphates, sulfates, and mixed phosphate/pyrophosphate. [2.5,2.6] After the introduction of LiFePO₄ by Goodenough et al., [2.7] various polyanionic materials have been extensively studied as cathode materials in LIBs. In particular, phosphate materials have been focused on due to the increase of redox potential and good stability caused by an inductive effect and a strong P-O covalent bond, respectively. The reversible capacity and operating voltage of LiFePO₄ are 170 mA h g⁻¹ and 3.4 V (vs. Li/Li⁺), respectively. Motived by this, NaMPO₄, which has a similar composition to LiFePO₄ has been researched. However, it is believed to be inappropriate as a cathode material for NIBs so far. In contrast to LiFePO₄, the thermodynamically stable polymorph of NaFePO₄ is the mineral maricite which is not electrochemically reacted with Na-ions due to its original structure form. [2.8] Electrochemically inactive olivine structure NaFePO₄ cannot be prepared directly under conventional synthetic conditions at high temperature, and accordingly, it has been obtained via electrochemical exchange of Na with Li. [2.9] However, the volume difference between Na-rich and Na-poor phases was 21%, which causes poor electrochemical performance. [2.8]

NASICON-type Na₃V₂(PO₄)₃ compounds have been most intensively researched as promising cathodes for NIBs because of their high

electrochemical performance [2.10-2.12] Tremendous efforts have been focused on improving the electrochemical performance of $\text{Na}_3\text{V}_2(\text{PO}_4)_3$. The reversible capacity and operating voltage of $\text{Na}_3\text{V}_2(\text{PO}_4)_3$ are 117 mA h g^{-1} and 3.6 V (vs. Na/Na^+), respectively, corresponding to two Na-ions reaction with a redox reaction of $\text{V}^{3+}/\text{V}^{4+}$, and it has a small volume change of 8.26% during charging/discharging [2.12] For these reasons, $\text{Na}_3\text{V}_2(\text{PO}_4)_3$ appear to be promising cathode in NIBs, however, the concerns on the use of toxic and costly vanadium also exist.

Inspired by the excellent electrochemical performance of $\text{Li}_2\text{FeP}_2\text{O}_7$, [2.13] $\text{Na}_2\text{FeP}_2\text{O}_7$ has been recently reported. It shows a reversible capacity and operating voltage of 90 mA h g^{-1} and 3.0 V (vs. Na/Na^+), respectively, and good cyclability. [2.14,2.15] Independently and simultaneously, a new pyrophosphate compound, $\text{Na}_{3.12}\text{Fe}_{2.44}(\text{P}_2\text{O}_7)_2$, was introduced. [2.16] The structure of $\text{Na}_{3.12}\text{Fe}_{2.44}(\text{P}_2\text{O}_7)_2$ is different from triclinic $\text{Na}_2\text{FeP}_2\text{O}_7$, however, the electrochemical behaviors of $\text{Na}_{3.12}\text{Fe}_{2.44}(\text{P}_2\text{O}_7)_2$ were observed to be very similar to those of $\text{Na}_2\text{FeP}_2\text{O}_7$, with a reversible capacity and operating voltage of 85 mA h g^{-1} and 3.0 V (vs. Na/Na^+), respectively, and exhibited a stable cyclic performance. Recently, two types of $\text{Na}_2\text{CoP}_2\text{O}_7$ polymorphs with an orthorhombic and triclinic framework have been introduced. Both orthorhombic and triclinic $\text{Na}_2\text{CoP}_2\text{O}_7$ delivered a reversible capacity close to 80 mA h g^{-1} involving a $\text{Co}^{2+}/\text{Co}^{3+}$ redox couple, but triclinic $\text{Na}_2\text{CoP}_2\text{O}_7$ exhibits higher operating voltage at 4.3 V (vs. Na/Na^+) than orthorhombic

$\text{Na}_2\text{CoP}_2\text{O}_7$ 3.0 V (vs. Na/Na^+). [2.17,2.18]

Fluorophosphates have been studied as promising new cathodes. In 2007, the Nazar group pioneered a new fluorophosphate material, $\text{Na}_2\text{FePO}_4\text{F}$, as a LIB cathode. [2.19] This compound shows good electrochemical performance including a reversible capacity of 124 mA h g^{-1} with stable cycle performance with a small volume change of 3.7% during charging/discharging. The Tarascon group reported $\text{Na}_2\text{FePO}_4\text{F}$ as a cathode for NIBs. [2.20] It exhibits high reversible Na-ion intercalation/deintercalation, but $\text{Na}_2\text{FePO}_4\text{F}$ shows higher polarization than the LIB application with a reversible capacity of 120 mA h g^{-1} . The volume change when one Na-ion charging/discharging was 4%.

A mixed phosphate/pyrophosphate cathode material has been studied. $\text{Na}_4\text{Fe}_3(\text{PO}_4)_2(\text{P}_2\text{O}_7)$ delivered an energy density of 380 W h kg^{-1} . Up to three Na-ions can be intercalated/deintercalated reversibly with a small volume change of 4%. [2.21]

Sulfates also considered potential candidates for NIB cathode. Barpanda et al. reported a new alluaudite $\text{Na}_2\text{Fe}_3(\text{SO}_4)_3$ as a cathode for NIBs. [2.22] $\text{Na}_2\text{Fe}_3(\text{SO}_4)_3$ is one of the highest $\text{Fe}^{2+}/\text{Fe}^{3+}$ redox reaction voltage at 3.8 V (vs. Na/Na^+) among all the Fe-based polyanionic compounds, and the electrode delivers a reversible capacity over 100 mA h g^{-1} . Also, it exhibits high power and cycle performances that originate from the small volume change of 1.6% during charging/discharging. Further investigations on the electrochemical mechanisms and Na diffusion kinetics of off-stoichiometric phases of

$\text{Na}_{2+2x}\text{Fe}_{2-x}(\text{SO}_4)_3$ were performed by the Yamada and Adam groups. [2.23,2.24]

While researchers have to solve some issues such as poor electrochemical performances and moisture sensitivity of these sulfate compounds.

2.3. Nanotechnologies for Battery Electrodes

An increase in the charge/discharge rate of rechargeable batteries of more than one order of magnitude is required to meet the future demands of hybrid electric vehicles and clean energy storage. Nanomaterials, so often hyped or misrepresented by claims of delivering new properties, have the genuine potential to make a significant impact on the performance of lithium-ion batteries, as their reduced dimensions enable far higher intercalation/deintercalation rates and hence high power. This is just one property that may be enhanced by the use of nanomaterials. According to the P. G. Bruce et al., some advantages and disadvantages of nanomaterials for rechargeable batteries are follow; [2.25]

Advantages

- i) They enable electrode reactions to occur that cannot take place for materials composed of micrometer-sized particles; In the case of TiO₂, for example, decreasing the particle size into the nano-regime (<100 nm) alternates the electrochemical reactions and increase the reactivity to Li. [2.26]
- ii) The dimensions reduction increases significantly the rate of alkali-ions intercalation/deintercalation, because of the short distances for alkali-ions transport within the particles. The characteristic time constant for diffusion

is given by $t = L^2/D$, where L is the diffusion length and D the diffusion constant. The time t for intercalation decreases with the square of the particle size on replacing micrometer with nanometer particles.[2.27]

- iii) Electron transport within the particles is also enhanced by nanometer-sized particles. [2.27]
- iv) The dimensions reduction increased the contact area between particles and electrolyte, resulting in a high alkali-ion flux across the interface.
- v) The range of composition over which solid solutions exist is often more extensive for nanoparticles, [2.28] and the strain associated with intercalation is often better accommodated.

Disadvantages

- i) It is difficult to synthesize nanoparticles and control their dimensions for purpose.
- ii) High electrolyte/electrode surface area may lead to more significant side reactions with the electrolyte, and more difficulty maintaining interparticle contact.
- iii) The density of a nanoparticles is generally less than the same material formed from micrometer-sized particles. Thus, electrode volume is increased for the same mass of material, resulting in degradation of volumetric energy density.

The last two decades have witnessed a great interest from various sections of the societies (academia, industry, government, and public) around the world to understand and explore the benefits of nanotechnology. The two most important aspects of nanotechnology are the ones that deal with the development of new materials and devices with reduced “nano” dimensions. In the last two decades, a wide variety of nanomaterials (sized or structured) were prepared in different forms by either physical or chemical “bottom-up” or “top-down” methods as shown in Figure 2.3.1 [2.2,2.29].

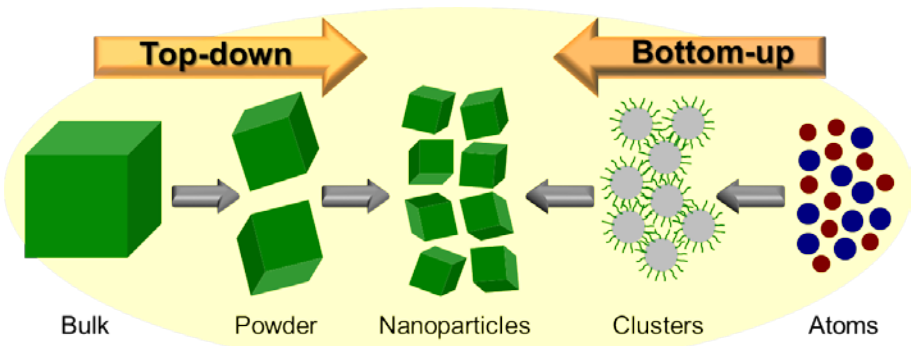


Figure 2.3.1 Schematic illustration of nanoparticles synthesis by top-down or bottom-up physical or chemical methods.

2.4 Flexible Batteries

Rechargeable LIBs have been widely used in portable devices as a power source due to their high power, high energy density. However, conventional LIBs are rigid and fragile and thus cannot meet the requirements of flexible, bendable, foldable and stretchable devices. In order to further facilitate in terms of portability, one of the trend in LIB development is spreading to light, thin, flexible and small systems. [30]

Unlike conventional batteries, flexible batteries require the evolution of flexible components, *i.e.* flexible electrodes, electrolytes and separators.

For the higher energy density in flexible batteries, they requires active materials with higher specific capacity in flexible electrodes, and non-active substances in the whole systems. So, flexible electrodes are usually fabricated by various functional organic and/or inorganic materials held on flexible conductive membrane substrates without any conductive additives and polymeric binders. Also, flexible polymeric solid electrolytes are generally used as both separator and electrolyte because they have good mechanical properties and flexibility. Thin polymeric materials are commonly used as packing materials for flexible batteries. The securement of suitable flexible electrodes, electrolyte and packaging are critical issues in developing high performance flexible batteries. Table 2.4.1 shows the structure and components of flexible and conventional batteries. In order to meet the flexible and thin

requirements of devices, various flexible electrode materials for flexible batteries have been prepared from carbonaceous and other membrane materials.
[2.29,2.30]

Table 2.4.1 Comparison of a flexible LIB with a traditional battery. [2.29]

Component	Flexible battery	Traditional battery
Active Materials	Thin, lightweight, flexible and integrated electrode materials	Anode: Graphite, $\text{Li}_4\text{Ti}_5\text{O}_{12}$, Si Cathode: LiCoO_2 , LiFePO_4 , LiMn_2O_4 , $\text{Li}(\text{Ni},\text{Mn},\text{Co})\text{O}_2$
Binder	No binders	PVDF, PTFE, PVA, CMC, SBR
Conductive agent	No conductive additives	Carbon based materials: carbon black, CNTs, graphite powder
Current collector	No current collector	Cu, Al foil
Electrolyte	Solid state, integration with polymer and salt electrolyte	Liquid or solution (organic solvent and lithium salt, electrolyte gel)
Separator		PP, PE, PA, PVDF, PVC
Seal and formats	Polymer package, pouch type	Aluminum plastic, aluminum or stainless steel seal, cylindrical, pouch, prismatic, coin type

2.5 Bibliography

- [2.1] M. Yoshio, R. J. Brodd, A. Kozawa, Lithium-Ion Batteries: Science and Technologies, Springer
- [2.2] Y. Abu-Lebdeh, I. Davidson, Nanotechnology for Lithium-Ion Batteries, Springer.
- [2.3] M. D. Slater, D. Kim, E. Lee, C. S. Johnson, *Adv. Funct. Mater.*, **2013**, *23*, 947-958.
- [2.4] L. P. Wang, L. Yu, X. Wang, M. Srinivasan, Z. J. Xu, *J. Mater. Chem. A*, **2015**, *3*, 9353-9378.
- [2.5] S. Y. Hong, Y. Kim, Y. Park, A. Choi, N.-S. Choi, K. T. Lee, *Energy Environ. Sci.*, **2013**, *6*, 2067-2081.
- [2.6] H. Kim, H. Kim, Z. Ding, M. H. Lee, K. Lim, G. Yoon, K. Kang, *Adv. Energy Mater.*, **2016**, *6*, 1600943.
- [2.7] A. K. Padhi, K. S. Nanjundaswamy, J. B. Goodenough, *J. Electrochem. Soc.*, **1997**, *144*, 1188-1194.
- [2.8] Y. Zhu, Y. Xu, Y. Liu, C. Luo, C. Wang, *Nanoscale*, **2013**, *5*, 780-787.
- [2.9] S.-M. Oh, S.-T. Myung, J. Hassoun, B. Scrosati, Y.-K. Sun, *Electrochem. Commun.*, **2012**, *22*, 149-152.
- [2.10] Z. Jian, L. Zhao, H. Pan, Y.-S. Hu, H. Li, W. Chen, L. Chen, *Electrochem. Commun.*, **2012**, *14*, 86-89.

- [2.11] S. Y. Lim, H. Kim, R. A. Shakoor, Y. Jung, J. W. Choi, *J. Electrochem. Soc.*, **2012**, *159*, A1393-A1397.
- [2.12] Z. Jian, W. Han, X. Lu, H. Yang, Y.-S. Hu, J. Zhou, Z. Zhou, J. Li, W. Chen, D. Chen, L. Chen, *Adv. Energy Mater.*, **2013**, *3*, 156-160.
- [2.13] S.-i. Nishimura, M. Nakamura, R. Natsui, A. Yamada, *J. Am. Chem. Soc.*, **2010**, *132*, 13596-13597.
- [2.14] P. Barpanda, T. Ye, S.-i. Nishimura, S.-C. Chung, Y. Yamada, M. Okubo, H. Zhou, A. Yamada, *Electrochem. Commun.*, **2012**, *24*, 116-119.
- [2.15] H. Kim, R. A. Shakoor, C. Park, S. Y. Lim, J.-S. Kim, Y. N. Jo, W. Cho, K. Miyasaka, R. Kahraman, Y. Jung, J. W. Choi, *Adv. Funct. Mater.*, **2013**, *23*, 1147-1155.
- [2.16] K.-H. Ha, S. H. Woo, D. Mok, N.-S. Choi, Y. Park, S. M. Oh, Y. Kim, J. Kim, J. Lee, L. F. Nazar, K. T. Lee, *Adv. Energy Mater.*, **2013**, *3*, 770-776.
- [2.17] P. Barpanda, J. Lu, T. Ye, M. Kajiyama, S.-C. Chung, N. Yabuuchi, S. Komaba, A. Yamada, *RSC Adv.*, **2013**, *3*, 3857-3860.
- [2.18] H. Kim, C. S. Park, J. W. Choi, Y. Jung, *Angew. Chem. Int. Ed.*, **2016**, *55*, 6662-6666.
- [2.19] B. L. Ellis, W. R. Makahnouk, Y. Makimura, K. Toghill, L. F. Nazar, *Nat. Mater.*, **2007**, *6*, 749-753.

- [2.20] N. Recham, J. N. Chotard, L. Dupont, K. Djellab, M. Armand, J. M. Tarascon, *J. Electrochem. Soc.*, **2009**, *156*, A993-A999.
- [2.21] H. Kim, I. Park, S. Lee, H. Kim, K.-Y. Park, Y.-U. Park, H. Kim, J. Kim, H.-D. Lim, W.-S. Yoon, K. Kang, *Chem. Mater.*, **2013**, *25*, 3614-3622.
- [2.22] P. Barpanda, G. Oyama, S. Nishimura, S. C. Chung, A. Yamada, *Nat. Commun.*, **2014**, *5*, 4358.
- [2.23] G. Oyama, S.-i. Nishimura, Y. Suzuki, M. Okubo, A. Yamada, *Chem. Electro. Chem.*, **2015**, *2*, 1019-1023.
- [2.24] J. Ming, P. Barpanda, S.-i. Nishimura, M. Okubo, A. Yamada, *Electrochem. Commun.*, **2015**, *51*, 19-22.
- [2.25] P. G. Bruce, B. Scrosati, J. M. Tarascon, *Angew. Chem. Int. Ed.*, **2008**, *47*, 2930-2946.
- [2.26] Z. Yang, D. Choi, S. Kerisit, K. M. Rosso, D. Wang, J. Zhang, G. Graff, J. Liu, *J. Power Sources*, **2009**, *192*, 588-598.
- [2.27] A. S. Arico, P. Bruce, B. Scrosati, J.-M. Tarascon, W. V. Schalkwijk, *Nat. Mater.*, **2005**, *4*, 366-377.
- [2.28] N. Meethong, H.-Y. S. Huang, W. C. Carter, Y.-M. Chiang, *Electrochem. Solid-State Lett.*, **2007**, *10*, A134-A138.
- [2.29] K. K. Fu, J. Cheng, T. Li, L. Hu, *ACS Energy Lett.*, **2016**, *1*, 1065-1079.
- [2.30] G. Zhou, F. Li, H.-M. Cheng, *Energy Environ. Sci.*, **2014**, *7*, 1307-1338.

Chapter 3. Na₂MP₂O₇/C Nanocomposites

3.1 Experiments

Synthesis of Fe-based Pyrophosphates

Sol-gel synthesis

All chemicals were obtained as reagent grade and used without further purification. Na₂MP₂O₇/C (M = Fe, Co, Ni) nanocomposites were synthesized via a sol-gel method using citric acid as a chelating agent as well as a carbon source. In a typical synthesis, metal-acetate source {Fe(CH₃COO)₂ (Fe 29.5%, Alfa Aesar), Mn(CH₃COO)₂·4H₂O (99%, Sigma-Aldrich), Co(CH₃COO)₂·4H₂O (98%, Sigma-Aldrich), Ni(CH₃COO)₂·4H₂O (99%, Sigma-Aldrich)} and citric acid (CA; 99.5%, Sigma-Aldrich) were dissolved in 50 mL of distilled water. Na(CH₃COO) (99%, Sigma-Aldrich) and NH₄H₂PO₄ (98%, Sigma-Aldrich) were dissolved in another 50 mL of distilled water. These two solutions were then mixed in a three-neck round-bottom flask, and then, refluxed at 80 °C for 12 h under magnetic stirring. After reflux, the solution was kept on a hotplate at 70 °C to evaporate the solvent. The wet gel was then completely dried in a vacuum oven. The resultant dried gel was first heat-treated in a tube furnace at 600 °C for 3 h flowing Ar gas or 5% H₂/Ar balance gas. The product was ball-milled with ZrO₂ balls and ethanol, dried, and heat-treated again at the same condition. In the case of synthesizing

$\text{Na}_2\text{MP}_2\text{O}_7$ NPs/C-rGO composite, GO solution (GO 2 wt% in water, Angstrom Materials) was added in mixed solution before reflux.

Solid-state reaction

All chemicals were obtained as reagent grade and used without further purification. Micro-sized bulk $\text{Na}_2\text{FeP}_2\text{O}_7$ was synthesized by a conventional solid-state reaction method. The starting materials were Na_2CO_3 (99%, Kojundo), $\text{FeC}_2\text{O}_4 \cdot 2\text{H}_2\text{O}$ (99%, Sigma-Aldrich) and $\text{NH}_4\text{H}_2\text{PO}_4$ (98%, Sigma-Aldrich). After the starting materials were mixed in a polypropylene bottle with ZrO_2 balls and absolute ethanol (99.9%, Daejung) as a medium for 24 h, they were dried and ground by an agate mortar. The mixture was heat-treated in a tube furnace at 650 °C for 6 h under reduction atmosphere flowing 5% H_2/Ar balance gas. Carbon-coated micro-sized $\text{Na}_2\text{FeP}_2\text{O}_7$ were synthesized by a 1-step process. Na_2CO_3 , $\text{FeC}_2\text{O}_4 \cdot 2\text{H}_2\text{O}$, $\text{NH}_4\text{H}_2\text{PO}_4$ and glucose (anhydrous, Sigma-Aldrich) were mixed and then heat-treated.

Materials Characterization

X-ray diffraction (XRD) patterns of the powder samples were measured with a Bruker D8-Advance using Cu $\text{K}\alpha$ radiation. Field-emission scanning electron microscopy (FESEM) images were taken by a Hitachi SU-70. High-resolution transmission electron microscopy (HRTEM) analysis, with energy-dispersive spectrometer (EDS) mapping, was conducted by a JEOL JEM-2100F.

The Brunauer–Emmett–Teller (BET) specific surface area and pore size distribution of the products were examined by a nitrogen adsorption–desorption process at 77 K using a Micromeritics ASAP 2010. The amount of carbon contents was measured by C, H, N elemental analyzer (Flash EA 1112, Thermo Electron Co.) and thermogravimetric analysis (TGA; DTG-60H, Shimadzu Co.). The samples were heated at temperatures ranging from room temperature to 750 °C at 10 °C min⁻¹ under air atmosphere. X-ray photoelectron spectroscopy (XPS) was performed with a Thermo Scientific Sigma Probe, using an Al K α X-ray source. The Na, Fe and P concentration dissolved in the solutions was determined using inductively coupled plasma-optical emission spectroscopy (ICP-OES; ICP-730 ES, Varian). The three-dimensional visualization crystal structure of Na₂MP₂O₇ was illustrated using the VESTA program.

3.2 Synthesis of $\text{Na}_2\text{MP}_2\text{O}_7/\text{C}$ Nanocomposites

3.2.1 $\text{Na}_2\text{MP}_2\text{O}_7\text{-NPs/C}$ ($\text{M} = \text{Fe}$)

$\text{Na}_2\text{FeP}_2\text{O}_7$ NPs embedded in carbon matrix, namely $\text{Na}_2\text{FeP}_2\text{O}_7\text{-NPs/C}$ nanocomposite was synthesized via a sol-gel method, followed by a post-heat treatment, ball milling and re-heat treatment process (HT \rightarrow BM \rightarrow HT). For the comparison of electrochemical performance, micro-sized bulk $\text{Na}_2\text{FeP}_2\text{O}_7$ with and without carbon coating (B- $\text{Na}_2\text{FeP}_2\text{O}_7$ and $\text{Na}_2\text{FeP}_2\text{O}_7/\text{C}$, respectively) were synthesized by a conventional solid-state reaction method.

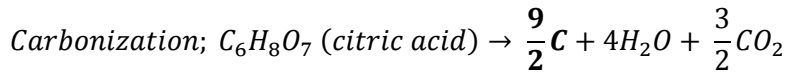
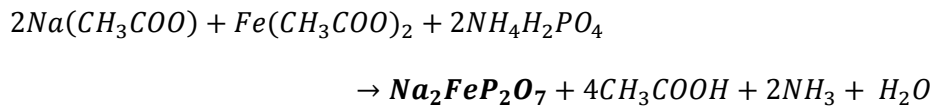
First, we synthesized the $\text{Na}_2\text{FeP}_2\text{O}_7\text{-NPs/C}$. The ratio of Na/Fe/P/CA in solution was 2:1:2:3. Figure 3.2.1a shows the FESEM images of $\text{Na}_2\text{FeP}_2\text{O}_7\text{-NPs/C}$ that were prepared by heat treatment of dried gel. $\text{Na}_2\text{FeP}_2\text{O}_7\text{-NPs/C}$, whose size was tens of nanometers, were synthesized after heat treatment at 600 °C for 3 h. However, as shown in Figure 3.2.1b, an unidentified substance covered the surface of the as-prepared $\text{Na}_2\text{FeP}_2\text{O}_7\text{-NPs/C}$ (A- $\text{Na}_2\text{FeP}_2\text{O}_7\text{-NPs/C}$), similar to an aggregation. This severe agglomeration of $\text{Na}_2\text{FeP}_2\text{O}_7\text{-NPs/C}$ would cause several drawbacks when fabricated in electrodes; *e.g.* insufficient permeation of electrolyte into active materials or interference of Na-ion desorption/insertion when charging/discharging. Hence, this surface substance needs to be removed, and separated $\text{Na}_2\text{FeP}_2\text{O}_7\text{-NPs/C}$ with less agglomeration need to be formed. These could be prepared by additional ball milling, and then, a re-heat treatment process. Substances on the surface of A-

$\text{Na}_2\text{FeP}_2\text{O}_7$ -NPs/C could be considerably eliminated by the ball milling process (Figure 3.2.1c and 3.2.1d). After heat treatment again, the unidentified substrate was not observed, while the $\text{Na}_2\text{FeP}_2\text{O}_7$ -NPs/C maintained their initial nano-shape and size (milled $\text{Na}_2\text{FeP}_2\text{O}_7$ -NPs/C; M- $\text{Na}_2\text{FeP}_2\text{O}_7$ -NPs/C in Figure 3.2.1e and 3.2.1f).

A- $\text{Na}_2\text{FeP}_2\text{O}_7$ -NPs/C was still observed upon heat-treating the dried gel at 600 °C for 6 h continuously without the ball milling process (Figure 3.2.2), indicating that it is essential that the ball milling process should be performed between the first heat treatment and re-heat treatment process to obtain M- $\text{Na}_2\text{FeP}_2\text{O}_7$ -NPs/C. When adding a lesser amount of citric acid in the Na-Fe-P-O solution (*i.e.*, Na:Fe:P:CA = 2:1:2:1), both nanoparticles and submicron-sized particles were observed after the first heat treatment, ball milling, and re-heat treatment process (Figure 3.2.3), implying that the amount of citric acid plays a significant role in the synthesis of $\text{Na}_2\text{FeP}_2\text{O}_7$ -NPs/C of uniform size.

Figure 3.2.4 shows the XRD patterns of B- $\text{Na}_2\text{FeP}_2\text{O}_7$ /C and $\text{Na}_2\text{FeP}_2\text{O}_7$ -NPs/C (both A- $\text{Na}_2\text{FeP}_2\text{O}_7$ -NPs/C and M- $\text{Na}_2\text{FeP}_2\text{O}_7$ -NPs/C) synthesized by the solid-state reaction and the sol-gel method, respectively. As shown in the XRD pattern of B- $\text{Na}_2\text{FeP}_2\text{O}_7$ /C (bottom), all the reflected peaks in the pattern coincided with those $\text{Na}_2\text{FeP}_2\text{O}_7$ peaks that were analyzed using the Rietveld refinement method. [3.1] Using this, the XRD patterns of A- $\text{Na}_2\text{FeP}_2\text{O}_7$ -NPs/C (middle) and M- $\text{Na}_2\text{FeP}_2\text{O}_7$ -NPs/C (top) were estimated. It can be seen that the reflection peaks in the patterns for A- $\text{Na}_2\text{FeP}_2\text{O}_7$ -NPs/C were in agreement with

those of B-Na₂FeP₂O₇-NPs/C. The Na₂FeP₂O₇-NPs/C were therefore formed by reaction equation as follows:



The peaks for the M-Na₂FeP₂O₇-NPs/C also matched well with B-Na₂FeP₂O₇ and A-Na₂FeP₂O₇-NPs/C, indicating that phase-pure Na₂FeP₂O₇-NPs/C could be synthesized and further processing (ball milling and re-heat treatment) did not affect the phase of the Na₂FeP₂O₇-NPs/C.

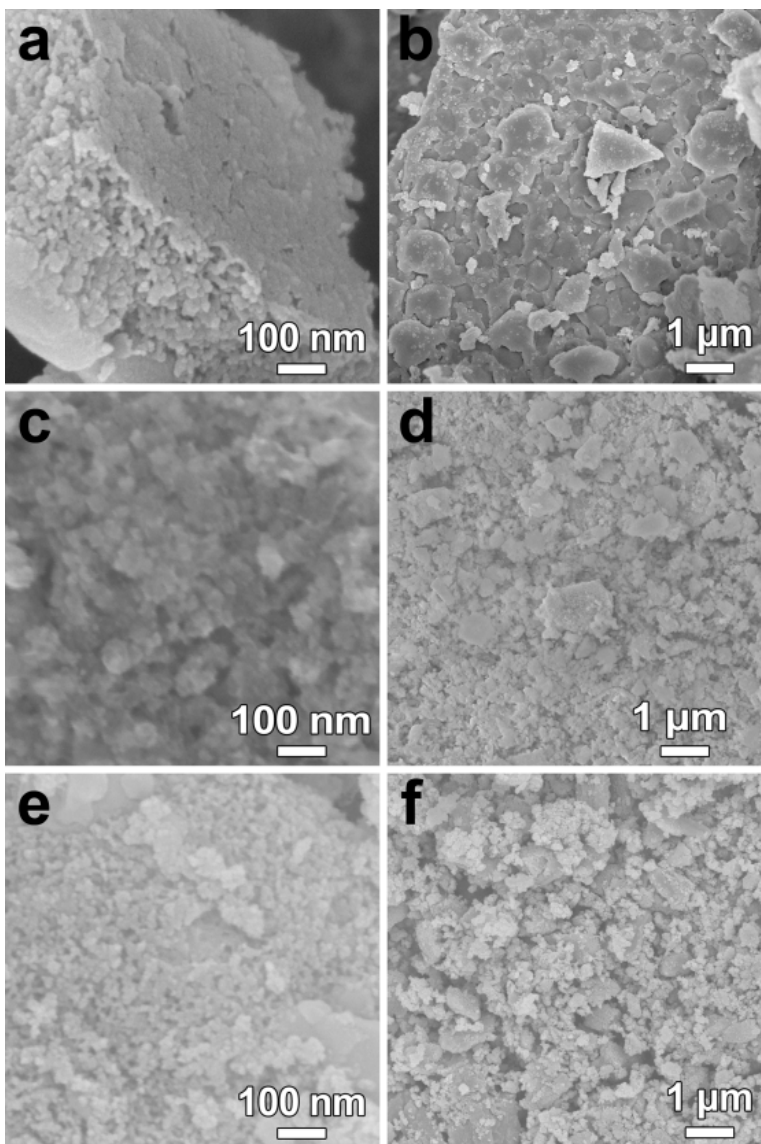


Figure 3.2.1 (a-b) High- and low-magnification FESEM images of A- $\text{Na}_2\text{FeP}_2\text{O}_7$ -NPs/C. (c-d) High- and low-magnification FESEM images of A- $\text{Na}_2\text{FeP}_2\text{O}_7$ -NPs/C after ball milling. (e-f) High- and low-magnification FESEM images of M- $\text{Na}_2\text{FeP}_2\text{O}_7$ -NPs/C.

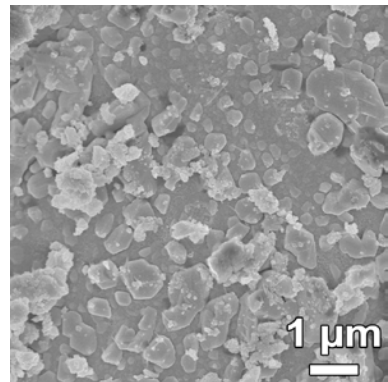


Figure 3.2.2 FESEM image of Na₂FeP₂O₇-NPs/C surface after heat treatment at 600 °C for 6 h.

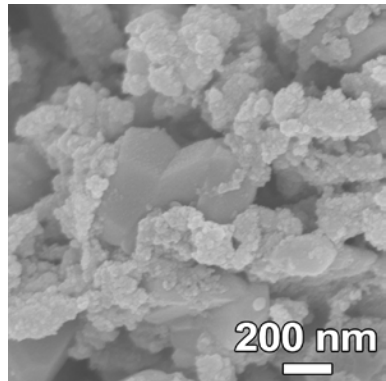


Figure 3.2.3 FESEM image of $\text{Na}_2\text{FeP}_2\text{O}_7$ -NPs/C synthesized by a sol-gel method with low amounts of citric acid.

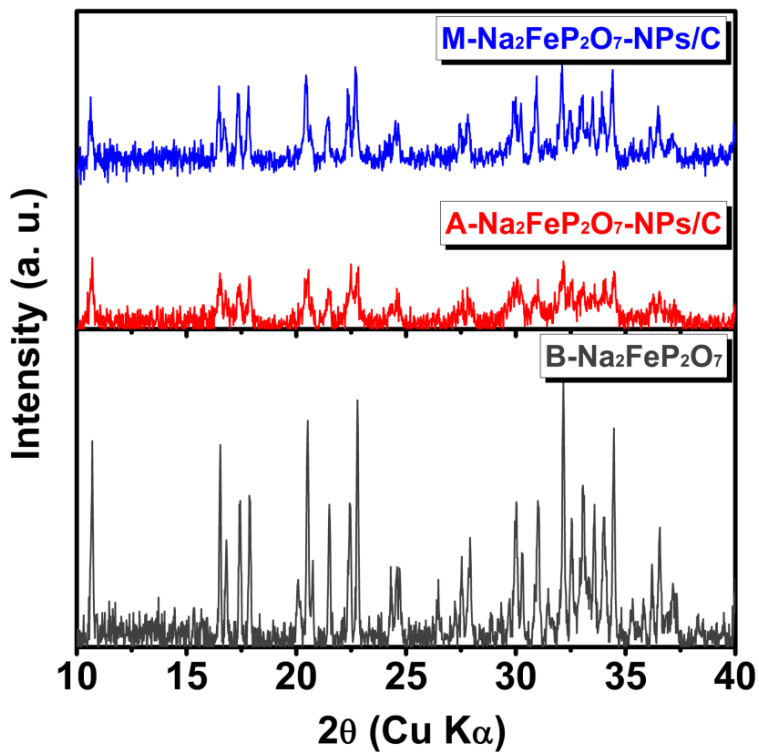


Figure 3.2.4 XRD patterns of B-Na₂FeP₂O₇ (bottom), A-Na₂FeP₂O₇-NPs/C (middle), and M-Na₂FeP₂O₇-NPs/C (top).

3.2.2 Na₂MP₂O₇-NPs/C (M = Co, Ni)

Na₂MP₂O₇-NPs/C (M = Co, Ni, Mn) nanocomposite were also synthesized for the same synthetic process. Figure 3.2.5 and 3.2.6 show the FESEM images of Na₂CoP₂O₇-NPs/C and Na₂NiP₂O₇-NPs/C, respectively. Similar to Na₂FeP₂O₇, agglomerated Na₂CoP₂O₇/C and Na₂NiP₂O₇/C nanocomposites (A-Na₂CoP₂O₇-NPs/C and A-Na₂NiP₂O₇-NPs/C), whose size was tens of nanometers, were also synthesized after heat treatment at 600 °C for 3 h (Figure 3.2.5a, 3.2.5b and 3.2.6a, 3.2.6b). After HT→BM→HT process, less-agglomerated and uniform-sized Na₂CoP₂O₇-NPs/C and Na₂NiP₂O₇-NPs/C can be obtained (M-Na₂CoP₂O₇-NPs/C and M-Na₂NiP₂O₇-NPs/C shown in Figure 3.2.5c, 3.2.5d and 3.2.6c, 3.2.6d). On the other hand, uniform-sized Na₂MnP₂O₇/C nanocomposite was not synthesized (FESEM images in Figure 3.2.7).

XRD patterns of Na₂MP₂O₇-NPs/C (M = Co, Ni, Mn) nanocomposite were investigated (Figure 3.2.8). Triclinic phase Na₂CoP₂O₇ and Na₂NiP₂O₇ which is similar to that of Na₂FeP₂O₇ were synthesized. Also, all the reflected peaks both Na₂CoP₂O₇-NPs/C and Na₂NiP₂O₇-NPs/C in the pattern coincided with each reference data (Na₂CoP₂O₇ with triclinic polymorph; JCPDS No. 13-3867, Na₂NiP₂O₇ with triclinic polymorph Na₂NiP₂O₇; JCPDS No. 52-1256), indicating that phase-pure Na₂CoP₂O₇-NPs/C and Na₂NiP₂O₇-NPs/C were synthesized. On the other hand, even though phase-pure and triclinic-phase Na₂MnP₂O₇ was synthesized, its phase is not the triclinic phase which is known to electrochemically inactive. It is known that Na₂MnP₂O₇ exists in two triclinic

polymorphs; space group of P1 and P-1. It is considered that $\text{Na}_2\text{MnP}_2\text{O}_7$ synthesized in this work is stable triclinic polymorph with P-1 space group, while triclinic polymorph with P1 space group which is similar to that of $\text{Na}_2\text{FeP}_2\text{O}_7$ is metastable phase in $\text{Na}_2\text{MnP}_2\text{O}_7$. Unfortunately, it is hard to synthesize metastable triclinic polymorph using this synthetic process. Therefore, it can be said that this synthetic strategy is appropriate for preparing the uniform-size and triclinic-phase $\text{Na}_2\text{MP}_2\text{O}_7$ (M = Fe, Co, Ni) nanocomposites.

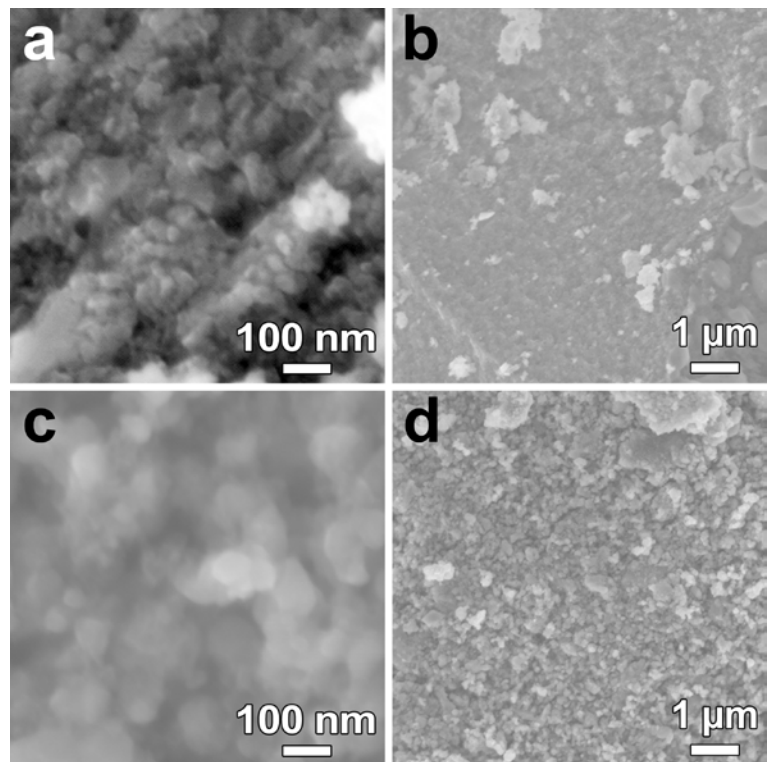


Figure 3.2.5 (a-b) High- and low-magnification FESEM images of A-
 $\text{Na}_2\text{CoP}_2\text{O}_7$ -NPs/C. (c-d) High- and low-magnification FESEM images of M-
 $\text{Na}_2\text{CoP}_2\text{O}_7$ -NPs/C.

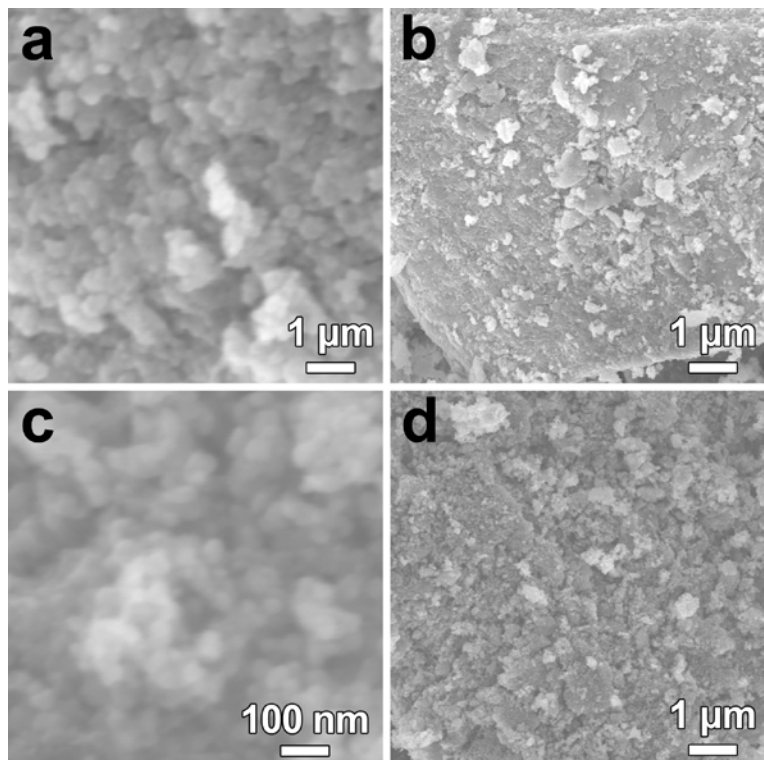


Figure 3.2.6 (a-b) High- and low-magnification FESEM images of A-
 $\text{Na}_2\text{NiP}_2\text{O}_7$ -NPs/C. (c-d) High- and low-magnification FESEM images of M-
 $\text{Na}_2\text{NiP}_2\text{O}_7$ -NPs/C.

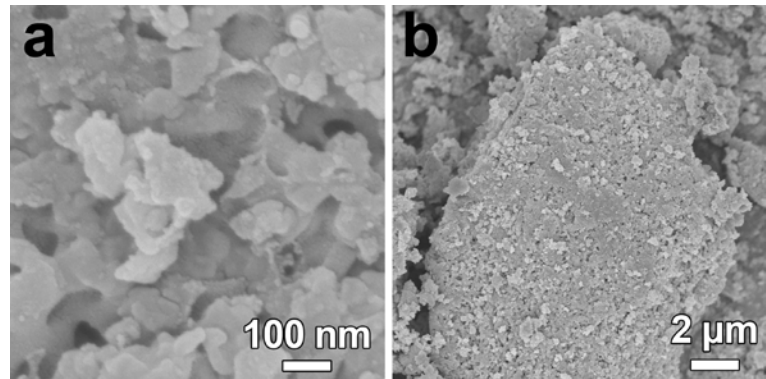


Figure 3.2.7 (a-b) High- and low-magnification FESEM images of $\text{Na}_2\text{MnP}_2\text{O}_7/\text{C}$.

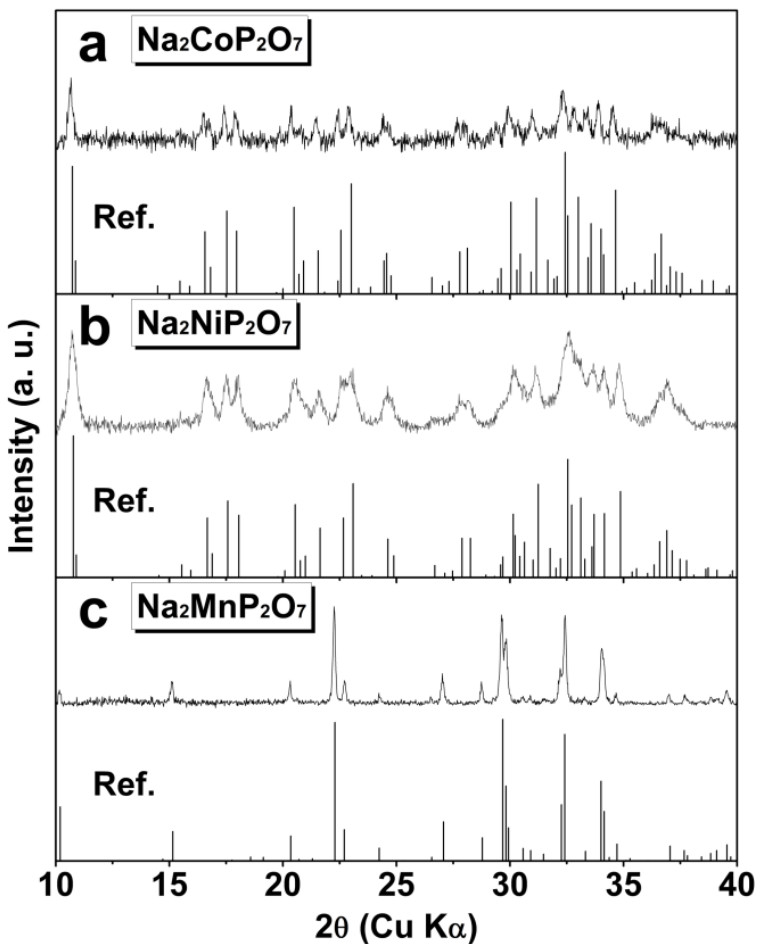


Figure 3.2.8 XRD patterns of (a) Na₂CoP₂O₇-NPs/C, (b) Na₂NiP₂O₇-NPs/C (middle), and (c) Na₂MnP₂O₇/C.

3.2.3 Nanocomposites Characterization

Nitrogen adsorption–desorption isotherms

The nitrogen adsorption (solid symbol)–desorption (open symbol) isotherms and their cumulative pore size distribution (inset) of $\text{Na}_2\text{FeP}_2\text{O}_7$ -NPs/C measured at 77 K are shown in Figure 3.2.9. All samples exhibit type II isotherms. According to the Barrett–Joyner–Halenda (BJH) and BET model, a few pores were detected in A- $\text{Na}_2\text{FeP}_2\text{O}_7$ -NPs/C, and their BET specific surface area was estimated to be $2.3 \text{ m}^2 \text{ g}^{-1}$, which seems to be too small despite the size of the $\text{Na}_2\text{FeP}_2\text{O}_7$ -NPs/C being tens of nanometers. The presence of a dense substance on the surface of the $\text{Na}_2\text{FeP}_2\text{O}_7$ -NPs/C resulted in this value. On the contrary, some pores were distributed in M- $\text{Na}_2\text{FeP}_2\text{O}_7$ -NPs/C and their BET specific surface area dramatically increased to $74 \text{ m}^2 \text{ g}^{-1}$, corresponding to the FESEM images in Figure 3.2.1. This large surface area is caused by not only less-agglomeration in NP-NFP, but also tiny flake-shaped carbon surrounding the $\text{Na}_2\text{FeP}_2\text{O}_7$ -NPs/C from the SEM and TEM (Figure 3.2.13) images. Although the $\text{Na}_2\text{FeP}_2\text{O}_7$ -NPs/C prepared in this study did not form a porous structure, the porosity and surface area analysis showed that the dense substance on the surface of A- $\text{Na}_2\text{FeP}_2\text{O}_7$ -NPs/C was removed by ball milling and re-heat treatment process. Meanwhile, the nitrogen adsorption (solid symbol)–desorption (open symbol) isotherms of M- $\text{Na}_2\text{CoP}_2\text{O}_7$ -NPs/C and $\text{Na}_2\text{NiP}_2\text{O}_7$ -NPs/C were measured (Figure 3.2.10). Both exhibit the same type II isotherms with that of M- $\text{Na}_2\text{FeP}_2\text{O}_7$ -NPs/C. Also, their BET specific surface

area was estimated to be 56 and 104 m² g⁻¹, respectively, corresponding to the FESEM images in Figure 3.2.5 and 3.2.6.

Powder packing

Meanwhile, in Figure 3.2.11, tightly packed B-Na₂FeP₂O₇/C (left), A-Na₂FeP₂O₇-NPs/C (middle) and M-Na₂FeP₂O₇-NPs/C (right) are shown in 4 mL glass vials. A-Na₂FeP₂O₇-NPs/C occupy less volume due to the severe agglomeration. In the case of M-Na₂FeP₂O₇-NPs/C, even though they display large surface area of 74.04 m² g⁻¹ as mentioned above, it is worth mentioning that they can form compact powder and exhibit higher powder packing compared to that of B-Na₂FeP₂O₇/C which has micro-sized irregular shape (inset of Figure 3.2.11). Therefore, our synthetic strategy can produce Na₂FeP₂O₇-NPs/C electrode that offer excellent electrochemical performance without sacrificing the volumetric energy density. More detailed packing density is under investigation.

Carbon contents

The TGA curves of A-Na₂FeP₂O₇-NPs/C and M-Na₂FeP₂O₇-NPs/C up to 750 °C, heated at a rate of 10 °C min⁻¹ in air atmosphere are shown in Figure 3.2.12. The starting point of weight loss was designated at 300 °C because weight loss between RT and 300 °C resulted from the removal of physisorbed water. Weight loss of both samples after 400 °C was attributed to the oxidation

of C. However, an additional gradual weight loss between 500 and 700 °C was observed in A-Na₂FeP₂O₇-NPs/C (green region), whereas there was no further weight loss in M-Na₂FeP₂O₇-NPs/C over 500 °C. It is estimated that the 4 wt% difference in the weight between both samples resulted from the presence of the unidentified substance on the surface of A-Na₂FeP₂O₇-NPs/C. Here, this unidentified substance is considered as one of the two: *(I) a substance related to NFP, or (II) a substance related to carbon*. Oxide-based Na₂FeP₂O₇ is hardly pulverized to less than 50 nm in size through the conventional ZrO₂ ball milling process. Based on this, the eliminated substance can be mainly considered as carbon-related materials that were not fully carbonized at the first heat treatment process. Also, carbon content in M-Na₂FeP₂O₇-NPs/C from elemental analysis was measured to be 16.2 wt%. Therefore, final carbon content in M-Na₂FeP₂O₇-NPs/C was 16-17 wt%. Meanwhile, carbon content in B-Na₂FeP₂O₇/C was estimated to be 15 wt% by TG analysis.

TEM analysis

Figure 3.2.13 shows the TEM images of M-Na₂FeP₂O₇-NPs/C. In Figure 3.2.13a, M-Na₂FeP₂O₇-NPs/C with particle sizes between 20 and 50 nm were homogeneously embedded in carbon (dark region in Figure 3.2.13a). Calculation by the Debye-Scherrer equation gives a grain size of 40 nm for M-Na₂FeP₂O₇-NPs/C, which is consistent with SEM (Figure 3.2.1) and TEM images. In the HRTEM image, the (011) plane corresponding to a lattice

spacing of 0.83 nm is consistent with the d-spacing of a triclinic $\text{Na}_2\text{FeP}_2\text{O}_7$ structure (Figure 3.2.13b). Further inspection of the reduced fast Fourier transform (FFT) revealed that these are $\text{Na}_2\text{FeP}_2\text{O}_7$ particles (Figure 3.2.13c). The elemental composition of M- $\text{Na}_2\text{FeP}_2\text{O}_7$ -NPs/C was determined via TEM EDS elemental mapping of C, Na, Fe, P, and O K α (Figure 3.2.14). All the elements were detected in the selected area, revealing that the particles are composed of elemental Na, Fe, P, and O that is homogeneously distributed in carbon.

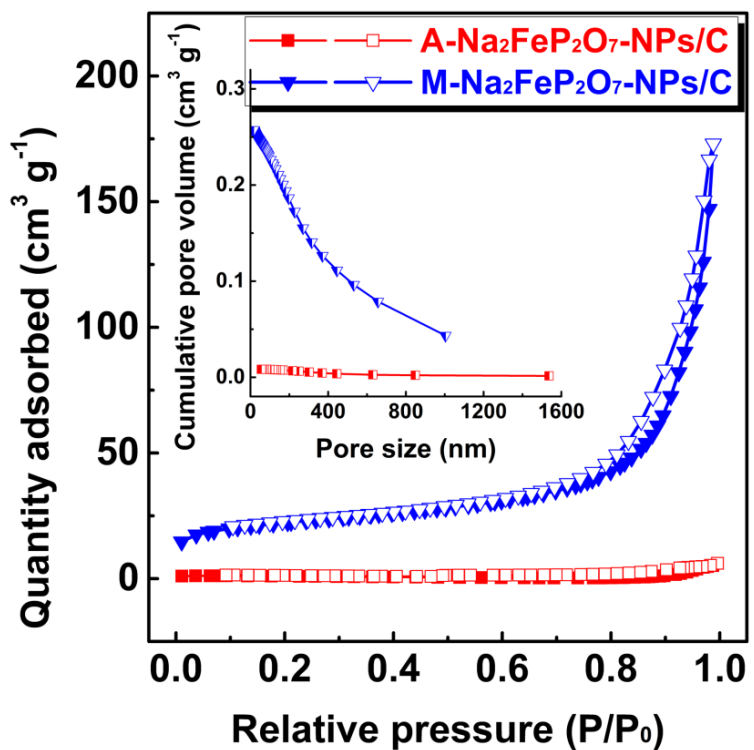


Figure 3.2.9 Nitrogen adsorption-desorption isotherms and their pore size distributions (inset) of A- $\text{Na}_2\text{FeP}_2\text{O}_7\text{-NPs/C}$ and M- $\text{Na}_2\text{FeP}_2\text{O}_7\text{-NPs/C}$.

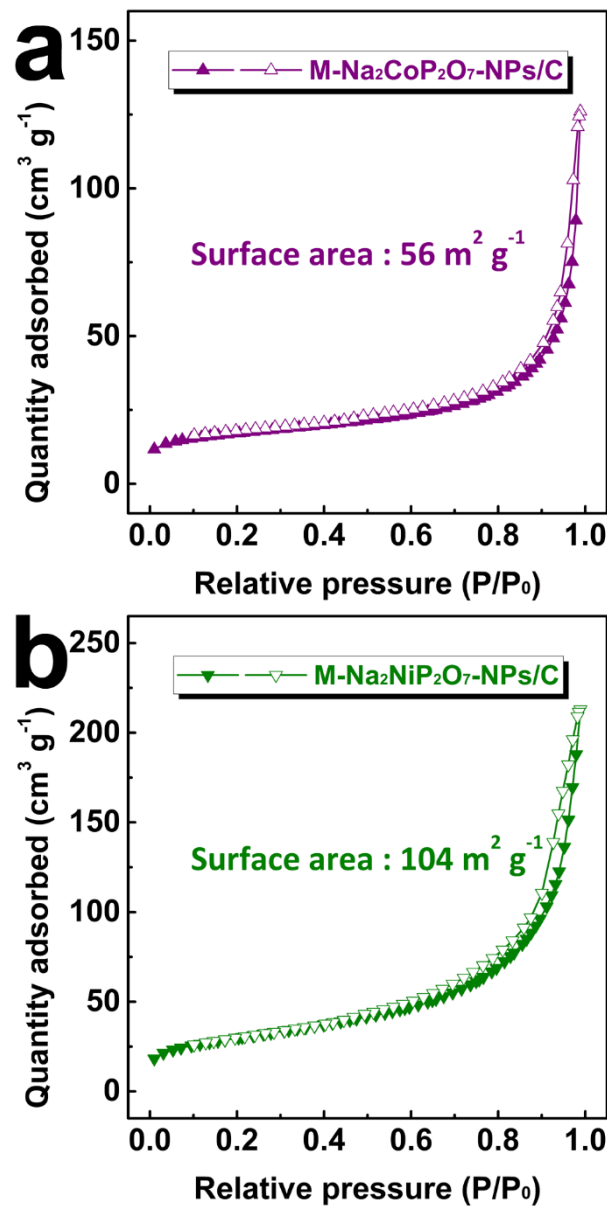


Figure 3.2.10 Nitrogen adsorption-desorption isotherms of (a) M-Na₂CoP₂O₇-NPs/C and (b) M-Na₂NiP₂O₇-NPs/C.

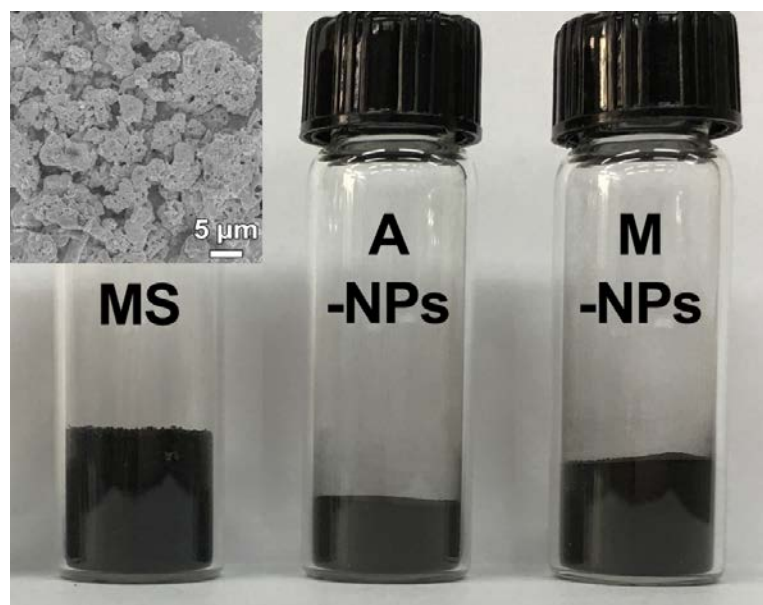


Figure 3.2.11 Digital photographs of B- $\text{Na}_2\text{FeP}_2\text{O}_7/\text{C}$, A- $\text{Na}_2\text{FeP}_2\text{O}_7\text{-NPs}/\text{C}$ and M- $\text{Na}_2\text{FeP}_2\text{O}_7\text{-NPs}/\text{C}$ powder in glass 4 ml vials (1 g each). Inset shows the FESEM image of B- $\text{Na}_2\text{FeP}_2\text{O}_7/\text{C}$.

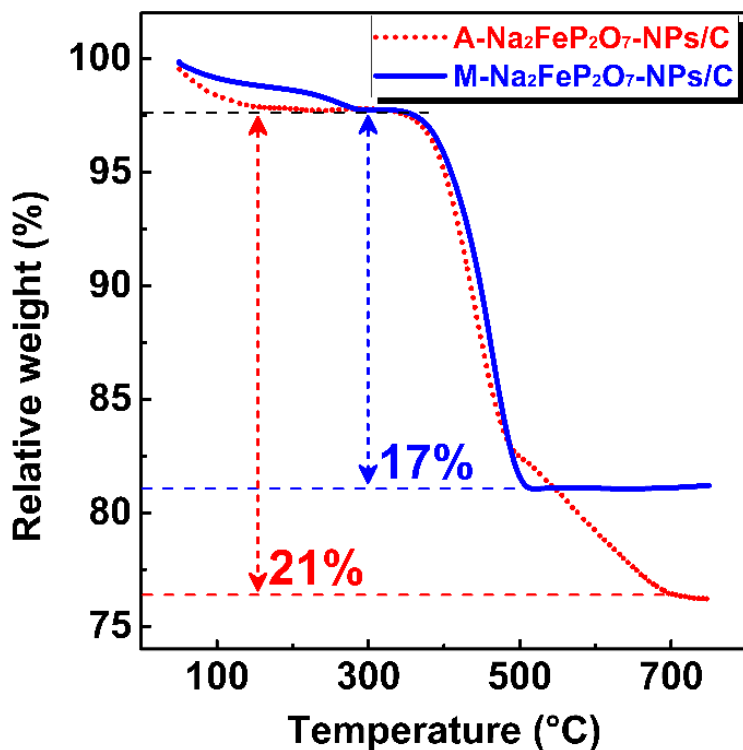


Figure 3.2.12 TGA (weight loss) curves of A- $\text{Na}_2\text{FeP}_2\text{O}_7$ -NPs/C and M- $\text{Na}_2\text{FeP}_2\text{O}_7$ -NPs/C.

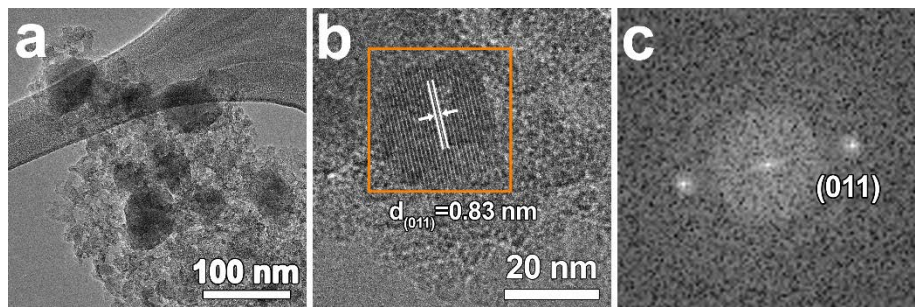


Figure 3.2.13 (a-b) Low-and high-resolution TEM images of M-Na₂FeP₂O₇-NPs/C and (c) reduced FFT of the area enclosed in the square in (b).

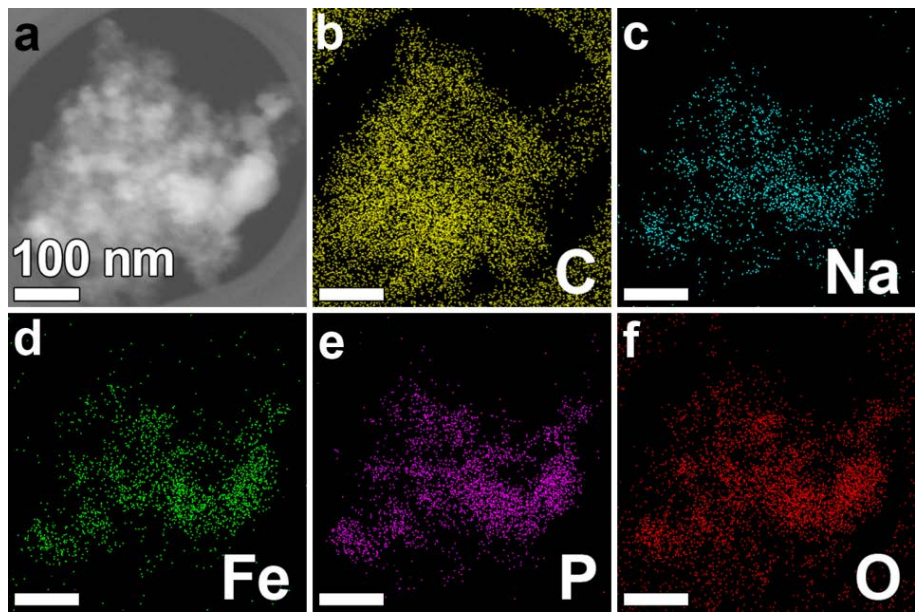


Figure 3.2.14 TEM EDS elemental mapping of M- $\text{Na}_2\text{FeP}_2\text{O}_7$ -NPs/C.

3.3 Bibliography

- [3.1] P. Barpanda, T. Ye, S.-i. Nishimura, S.-C. Chung, Y. Yamada, M. Okubo, H. Zhou, A. Yamada, *Electrochem. Commun.*, **2012**, *24*, 116-119.

Chapter 4. Fe-Based Pyrophosphate

4.1 Experiments

Synthesis of $\text{Na}_{3.12}\text{Fe}_{2.44}(\text{P}_2\text{O}_7)_2/\text{C}$ and $\text{Na}_{3.12}\text{Fe}_{2.44}(\text{P}_2\text{O}_7)_2/\text{C/rGO}$ Nanocomposites

Sol-gel synthesis

All chemicals were obtained as reagent grade and used without further purification. $\text{Na}_{3.12}\text{Fe}_{2.44}(\text{P}_2\text{O}_7)_2/\text{C}$ Nanocomposite were synthesized via a sol-gel method using citric acid as a chelating agent as well as a carbon source. In a typical synthesis, metal-acetate source $\{\text{Fe}(\text{CH}_3\text{COO})_2$ (Fe 29.5%, Alfa Aesar) and citric acid (CA; 99.5%, Sigma-Aldrich) were dissolved in 50 mL of distilled water. $\text{Na}(\text{CH}_3\text{COO})$ (99%, Sigma-Aldrich) and $\text{NH}_4\text{H}_2\text{PO}_4$ (98%, Sigma-Aldrich) were dissolved in another 50 mL of distilled water. These two solutions were then mixed in a three-neck round-bottom flask, and then, refluxed at 80 °C for 12 h under magnetic stirring. After reflux, the solution was kept on a hotplate at 70 °C to evaporate the solvent. The wet gel was then completely dried in a vacuum oven. The resultant dried gel was first heat-treated in a tube furnace at 600 °C for 3 h flowing Ar gas or 5% H_2/Ar balance gas. The product was ball-milled with ZrO_2 balls and ethanol, dried, and heat-treated again at the same condition. In the case of synthesizing $\text{Na}_{3.12}\text{Fe}_{2.44}(\text{P}_2\text{O}_7)_2/\text{C-rGO}$ composite, GO solution (GO 2 wt% in water,

Angstrom Materials) was added in mixed solution before reflux.

Electrochemical Measurements

The electrochemical properties of all Fe-based pyrophosphate samples were evaluated using coin-type (CR2032) half cells that were fabricated in an Ar-filled glove box. Working electrodes were prepared active materials, Super P carbon black (MMM Carbon, Belgium), and PVDF binder (Sigma-Aldrich) with weight ratios of 70:15:15, 80:5:15 or 85:5:10, and were cast onto Al foil. The average mass loading of the active materials on Al foil was 0.5-1.5 mg cm⁻². The cells were assembled with a working electrode, a separator film (glass microfiber), and Na-metal foil as the counter electrode saturated with a liquid electrolyte consisting of 1 M NaClO₄ dissolved in a solution of ethylene carbonate and propylene carbonate (EC/PC), at a volume ratio of 1:1. The fabricated cells were galvanostatically cycled using an automatic battery cycler (WBCS3000, WonATech, Korea). Fe-based pyrophosphate electrodes were cycled at voltages ranging from 2.0 to 4.0 V. Cyclic voltammetry (CV) measurements were obtained at a scan rate of 0.03 or 0.05 mV s⁻¹. For the galvanostatic intermittent titration technique (GITT), a constant current of 0.1 C was applied for 20-25 min and then interrupted to open circuit condition for 60 min. This process was repeated until the cathode potential exceeded the cut-off voltage. Electrochemical impedance spectroscopy (EIS) measurements were conducted at a frequency range of 100 kHz to 10 mHz with AC amplitude

of 10 mV, on an Ivium-n-Stat (Ivium Technologies, Netherlands) electrochemical test system.

4.2 Na₂FeP₂O₇/C Nanocomposite for Na-Ion Batteries

Cyclic voltammetry

The electrochemical properties of the B-Na₂FeP₂O₇/C and Na₂FeP₂O₇-NPs/C electrodes were evaluated for the NIB cathode, over the voltage range of 2.0–4.0 V (vs. Na/Na⁺). Figure 4.2.1 shows the cyclic voltammograms of B-Na₂FeP₂O₇/C and M-Na₂FeP₂O₇-NPs/C after the 2nd scan measured at a scan rate of 0.03 mV s⁻¹ to identify the electrochemical reactions. It is known that Na₂FeP₂O₇ exhibits four pairs of redox peaks, one near 2.5 V and three near 3.0 V. [4.1] It can be seen that a greater current density was observed in M-Na₂FeP₂O₇-NPs/C than B-Na₂FeP₂O₇/C in almost all the redox peaks, indicating a higher reactivity of M-Na₂FeP₂O₇-NPs/C with Na ions than B-Na₂FeP₂O₇/C. Furthermore, although both B-Na₂FeP₂O₇/C and M-Na₂FeP₂O₇-NPs/C exhibited a clear redox peak near 2.5, only the M-Na₂FeP₂O₇-NPs/C displayed three well-defined redox peaks at 2.98/2.88, 3.10/2.99 and 3.23/3.12 in CV, contrary to B-Na₂FeP₂O₇/C. These peak positions were consistent with previous studies. [4.1]

Cyclic performance

Figure 4.2.2 shows a comparison of the galvanostatic charging/discharging profiles of B-Na₂FeP₂O₇/C and M-Na₂FeP₂O₇-NPs/C at 0.05 C (1 C = 97 mA g⁻¹) for the 2nd and 5th cycle. Both B-Na₂FeP₂O₇/C and M-

$\text{Na}_2\text{FeP}_2\text{O}_7$ -NPs/C have coupled flat charge/discharge plateaus at around 2.5 and 3 V, corresponding to the redox pair of $\text{Fe}^{2+}/\text{Fe}^{3+}$. [4.1-4.3] At the 2nd discharging cycle, B- $\text{Na}_2\text{FeP}_2\text{O}_7$ /C exhibits a similar discharge profile and capacity as reported in previous research, which investigated the electrochemical properties of B- $\text{Na}_2\text{FeP}_2\text{O}_7$ /C. [4.1-4.3] Compared to B- $\text{Na}_2\text{FeP}_2\text{O}_7$ /C, the 2nd discharge capacity of M- $\text{Na}_2\text{FeP}_2\text{O}_7$ -NPs/C is increased and was measured as 96 mA h g^{-1} , which is close to the theoretical capacity of $\text{Na}_2\text{FeP}_2\text{O}_7$, indicating that one Na ion was inserted per formula unit cell during discharging, and the insertion of Na ions increased as the particle size was reduced to the nanoscale. Furthermore, M- $\text{Na}_2\text{FeP}_2\text{O}_7$ -NPs/C exhibit almost identical discharge profiles in the subsequent 5 cycles, indicating an equivalent Na insertion behavior at the initial discharging cycles. Meanwhile, the atomic ratio of Fe/P in two $\text{Na}_2\text{FeP}_2\text{O}_7$ samples were measured to be 0.5 by ICP-OES, implying that all the synthesized $\text{Na}_2\text{FeP}_2\text{O}_7$ samples could exhibit at most one $\text{Fe}^{2+}/\text{Fe}^{3+}$ redox reaction in the unit cell when charging/discharging, contrary to the Fe-excess $\text{Na}_2\text{FeP}_2\text{O}_7$ compounds, $\text{Na}_{4-2x}\text{Fe}_{2+x}(\text{P}_2\text{O}_7)_2$, in which more than one $\text{Fe}^{2+}/\text{Fe}^{3+}$ redox reaction is possible. (Table 4.2.1).

Figure 4.2.3 shows a comparison between the specific capacities of the B- $\text{Na}_2\text{FeP}_2\text{O}_7$ /C (at 0.2 C), A- $\text{Na}_2\text{FeP}_2\text{O}_7$ -NPs/C (at 0.05 C), and M- $\text{Na}_2\text{FeP}_2\text{O}_7$ -NPs/C (at 0.2 C) electrodes over 100 charging-discharging cycles. B- $\text{Na}_2\text{FeP}_2\text{O}_7$ /C maintains specific discharge capacities of 72–77 mA h g^{-1} up to the 30th cycle, and then, gradually decreased. A- $\text{Na}_2\text{FeP}_2\text{O}_7$ -NPs/C, in spite of

the nanoscale particles and being measured at a slow rate, delivered lower initial specific discharge capacities of 51–55 mA h g⁻¹ compared to those of B-Na₂FeP₂O₇/C. As mentioned before, the carbon-related substance on the surface of Na₂FeP₂O₇-NPs/C interfered with the insertion/desertion of Na ions. Contrary to B-Na₂FeP₂O₇/C, however, no significant capacity degradation occurred in A-Na₂FeP₂O₇-NPs/C. Interestingly, M-Na₂FeP₂O₇-NPs/C exhibits superior specific capacity and stable cyclability at 0.2 C. During the initial cycles, the discharge capacities were measured to be 96 mA h g⁻¹, indicative of ~1 Na ion insertion per formula unit cell. After several cycles, M-Na₂FeP₂O₇-NPs/C exhibit stable discharge capacities of 95 mA h g⁻¹ up to the 100th cycle. Particle size reduction to the nanoscale level resulted in a shortening of the diffusion distance of the Na ions, increasing the contact area between M-Na₂FeP₂O₇-NPs/C and the electrolyte, which activates more Na ion reactions with M-Na₂FeP₂O₇-NPs/C. Additionally, the homogeneous distribution of M-Na₂FeP₂O₇-NPs in carbon improved their electrochemical performance. Coulombic efficiency of M-Na₂FeP₂O₇-NPs/C increases to more than 99% after several initial cycles, indicating a reversible Na ion insertion/desertion reaction with Na₂FeP₂O₇-NPs/C. The structure of the M-Na₂FeP₂O₇-NPs/C after multiple cycles was evaluated by disassembling the testing cell. All the peaks in the ex-situ XRD pattern of the M-Na₂FeP₂O₇-NPs/C cell after 100 cycles coincided with those of M-Na₂FeP₂O₇-NPs/C prior to cycling (Figure 4.2.4). From these results, it was confirmed that M-Na₂FeP₂O₇-NPs/C shows a high

microstructural stability with reversible reaction after 100 charging/discharging cycles.

Rate capability

Comparison of rare performance between B-Na₂FeP₂O₇/C and M-Na₂FeP₂O₇-NPs/C at 0.1, 1 and 10 C are shown in Figure 4.2.5, and their discharge capacities around 2.5 and 3 V are summarized in Table 4.2.2. When increasing the rate from 0.1 to 10 C, discharge capacity of B-Na₂FeP₂O₇/C and M-Na₂FeP₂O₇-NPs/C at the voltage of 2.5 V was decreased from 26 to 23 mA h g⁻¹ and from 29 to 25 mA h g⁻¹, respectively, indicative of a little capacity drop both micro-sized particle and nano-sized Na₂FeP₂O₇ particle. However, at 3.0 V plateau, discharge capacity of B-Na₂FeP₂O₇/C was significantly decreased from 50 to 13 mA h g⁻¹, while relatively little discharge capacity decrease of M-Na₂FeP₂O₇-NPs/C from 65 to 52 mA h g⁻¹. According to H. Kim et al., [4.1] calculated migration energy of Na-ions at 2.5 V is lower than that at 3.0 V, indicating that Na-ion can easily inserted/deserted at 2.5 V than at 3.0 V both thermodynamically and kinetically. For this reason, it is considered that particle size have little influence on the capacity drop as the rate is increased at 2.5 V. At 3.0 V, in the case of micro-sized particles, accessibility of Na-ions to the center of particles is worse as the rate is increased due to the relatively higher migration energy, which resulted in fast capacity drop. On the other hand, even though higher migration energy at 3.0 V, less capacity drop occurred in nano-

sized particles as the rate was increased because Na-ions can easily reach the center of particles due to the short diffusion length of Na-ions.

Electrochemical impedance spectroscopy (EIS) was performed at a frequency ranging between 100 kHz and 10 mHz to compare the charge transfer resistances of B-Na₂FeP₂O₇/C and Na₂FeP₂O₇-NPs/C at 3.0 V (Figure 4.2.6). All the plots show a semicircle in the high-frequency region, corresponding to the charge transfer resistance at the electrode/electrolyte interface. The lower charge transfer resistance enables a more rapid charge transfer, resulting in faster kinetics of the faradic reaction. [4.4] Shown in Figure 4.2.6, Na₂FeP₂O₇-NPs/C exhibited a smaller diameter of the high-frequency semicircle than that of B-Na₂FeP₂O₇/C at the 2nd and 10th charged and discharged states at 3.0 V. Also, the fitted R_{ct} values of Na₂FeP₂O₇-NPs/C were 278, 279 Ω and at 2nd charged and discharged states and 380, 306 Ω at 10th charged and discharged states, respectively, which are lower than those of B-Na₂FeP₂O₇/C in all charged and discharged states (572, 584 Ω and 850, 724 Ω at 2nd and 10th charged and discharged state, respectively). Due to the fact that Na₂FeP₂O₇-NPs/C has a lower charge transfer resistance compared to B-Na₂FeP₂O₇/C, Na₂FeP₂O₇-NPs/C exhibited the better rate capability than B-Na₂FeP₂O₇/C at 3.0 V.

The rate performance of M-Na₂FeP₂O₇-NPs/C from 0.1 to 60 C are presented in Figure 4.2.7. With increasing rates of 0.1, 0.2, 0.5, 1, 2, and 5 C, the discharge capacities of M-Na₂FeP₂O₇-NPs/C were measured to be 95, 93, 89, 87, 84 and 81 mA h g⁻¹, respectively. Interestingly, with more increasing

rates of 10, 15 20, 30 and 60 C, the discharge capacities were measured to be 77, 73, 70, 66 and 55 mA h g⁻¹, respectively, indicating that significant capacities were obtained even at high rates. This superior performance at low and high rates is unprecedented for a state-of-the-art non-aqueous electrolyte, Na₂FeP₂O₇ cathode operating at room temperature in NIB (Figure 4.2.8). [4.4-4.6]

Meanwhile, although M-Na₂FeP₂O₇-NPs/C showed a superior rate capability, carbon content in this composite was relatively higher than that of other commercial active materials, which means that the amount of active material contributing actual capacity is small. But it is difficult to control the carbon content in M-Na₂FeP₂O₇-NPs/C. However, it is considered that tiny carbon flakes in M-Na₂FeP₂O₇-NPs/C can compensate the low electrical conductivity of Na₂FeP₂O₇-NPs. So, by decreasing ratios of carbon black and/or binder, M-Na₂FeP₂O₇-NPs/C electrode which has higher loading amount of active material was tested. Figure 4.2.9 shows the rate capability of M-Na₂FeP₂O₇-NPs/C that weight ratios of active material/carbon black/binder in working electrodes are 70:15:15, 80:5:15 and 85:5:10 at different rates from 0.1 to 10 C. With increasing rates of 0.1, 0.2, 0.5, 1, 2, 5 and 10 C, the discharge capacities of M-Na₂FeP₂O₇-NPs/C were measured to be 95, 94, 90, 87, 83, 78, 74 mA h g⁻¹ (in case of 80:5:15) and 95, 94, 90, 87, 83, 78, 71 mA h g⁻¹ (in case of 80:5:10), respectively. As the ratio of active material was increased to 85 wt% and carbon black and binder was decreased to 5 and 10 wt%, respectively, they

exhibited almost the same rate performance up to the high rate of 10 C. That is, higher loading ratio of active material in electrode have little influence on the rate performance due to the sufficient amount of carbon content in M-Na₂FeP₂O₇-NPs/C which can replace the role of carbon black that promotes the charge transfer in electrode.

Also, it is important to evaluate the electrode which has a high loading of active material. So, M-Na₂FeP₂O₇-NPs/C electrodes with higher amount of active material were evaluated. Figure 4.2.10 shows the rate capability of M-Na₂FeP₂O₇-NPs/C with different loading of active material (0.5 and 1.5 mg cm⁻²) at different rates from 0.1 to 10 C. With increasing rates of 0.1, 0.2, 0.5, 1, 2, 5 and 10 C, the discharge capacities of M-Na₂FeP₂O₇-NPs/C were measured to be 95, 93, 90, 88, 85, 82, 78 mA h g⁻¹ (in case of 0.5 mg cm⁻²) and 95, 91, 88, 86, 82, 76, 71 mA h g⁻¹ (in case of 1.5 mg cm⁻²), respectively. By increasing the loading amount of active material in working electrode for three times, they exhibited the similar rate performance up to 1 C, and a little capacity differences at high rate, but not much. That is, it can be said that this M-Na₂FeP₂O₇-NPs/C have good reliability even if it has a high loading of active material.

Long-term cyclability

In addition to superior rate capability, M-Na₂FeP₂O₇-NPs/C showed the remarkable long-term cyclic stability at 10 C and 60 C after 10000 cycles which capacity retention were 83 and 84% (0.00186 and 0.00174% capacity

degradation per cycle), respectively, indicative of superior fast charge/discharge capability and long-term cyclability (Figure 4.2.8). It is one of the few material in polyanionic cathodes to exhibit high rate capability and long-term cyclability. Note that large-scale energy storage systems mainly require high rate capability and long-term cyclability, which corresponds to these $\text{Na}_2\text{FeP}_2\text{O}_7$ -NPs/C. [4.7]

Table 4.2.1 Atomic ratio of Na, Fe, and P in each B-Na₂FeP₂O₇/C and M-Na₂FeP₂O₇-NPs/C by ICP analysis.

Sample	Element	# of Moles	Atomic Ratio
B- Na ₂ FeP ₂ O ₇ /C	Na	0.371	2.08
	Fe	0.175	0.98
	P	0.357	2.00
M- Na ₂ FeP ₂ O ₇ - NPs/C	Na	0.338	2.10
	Fe	0.159	0.99
	P	0.322	2.00

Table 4.2.2 Discharge capacities of B-Na₂FeP₂O₇/C and M-Na₂FeP₂O₇-NPs/C at different rates of 0.1, 1 and 10 C obtained from Figure 4.2.5.

Sample	Discharge capacity (mA h g ⁻¹)					
	0.1 C		1 C		10 C	
	2.5 V	3.1 V	2.5 V	3.1 V	2.5 V	3.1 V
Bulk	26	50	24	43	23	13
NPs	29	65	26	61	25	52

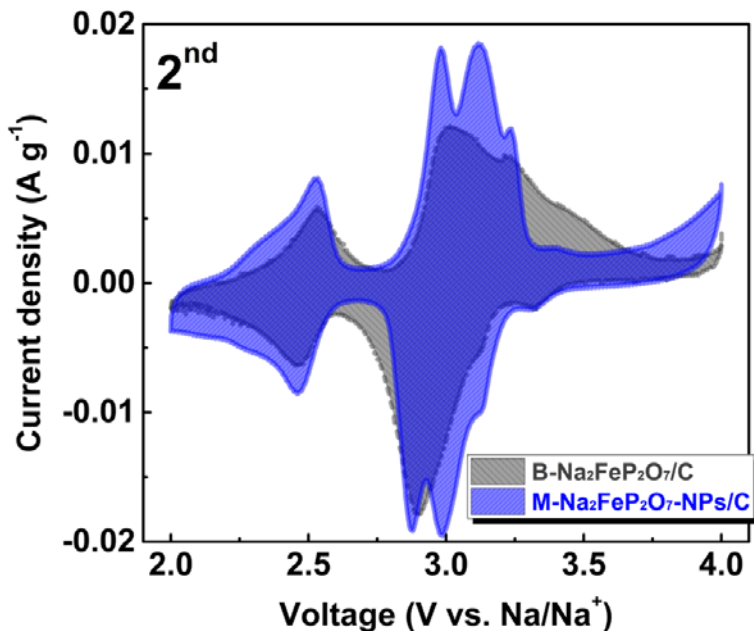


Figure 4.2.1 Cyclic voltammetry of B- $\text{Na}_2\text{FeP}_2\text{O}_7/\text{C}$ and M- $\text{Na}_2\text{FeP}_2\text{O}_7\text{-NPs}/\text{C}$

at a scan rate of 0.03 mV s^{-1} .

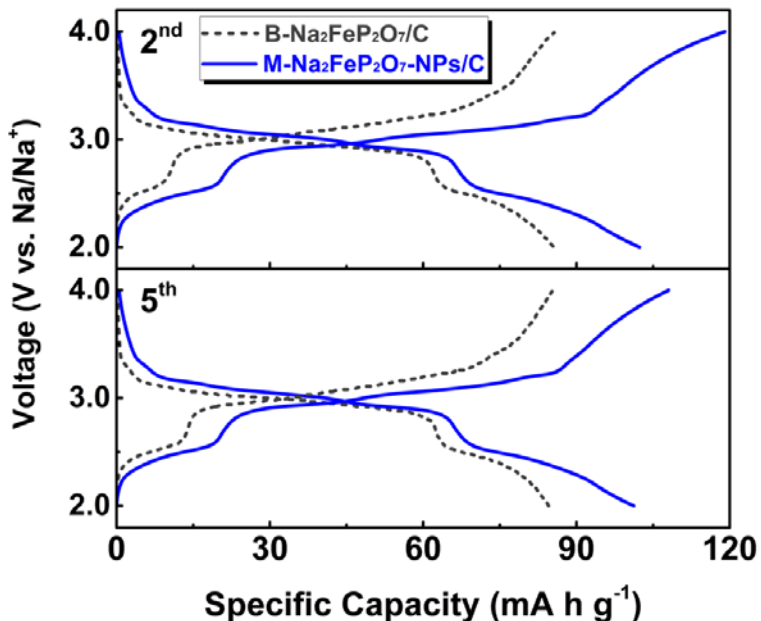


Figure 4.2.2 2nd and 5th galvanostatic voltage profiles of B-Na₂FeP₂O₇/C and M-Na₂FeP₂O₇-NPs/C at 0.05 C.

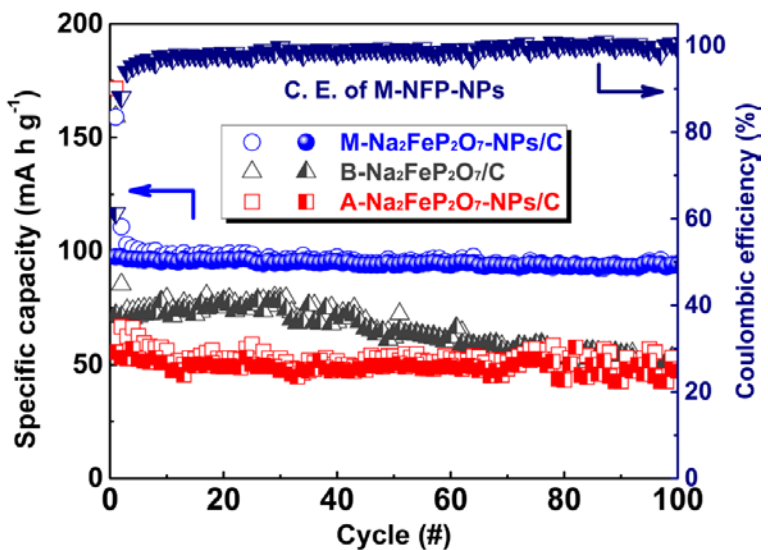


Figure 4.2.3 Specific capacities of B-Na₂FeP₂O₇/C (0.2 C), A-Na₂FeP₂O₇-NPs/C (0.05 C) and M-Na₂FeP₂O₇-NPs/C (0.2 C).

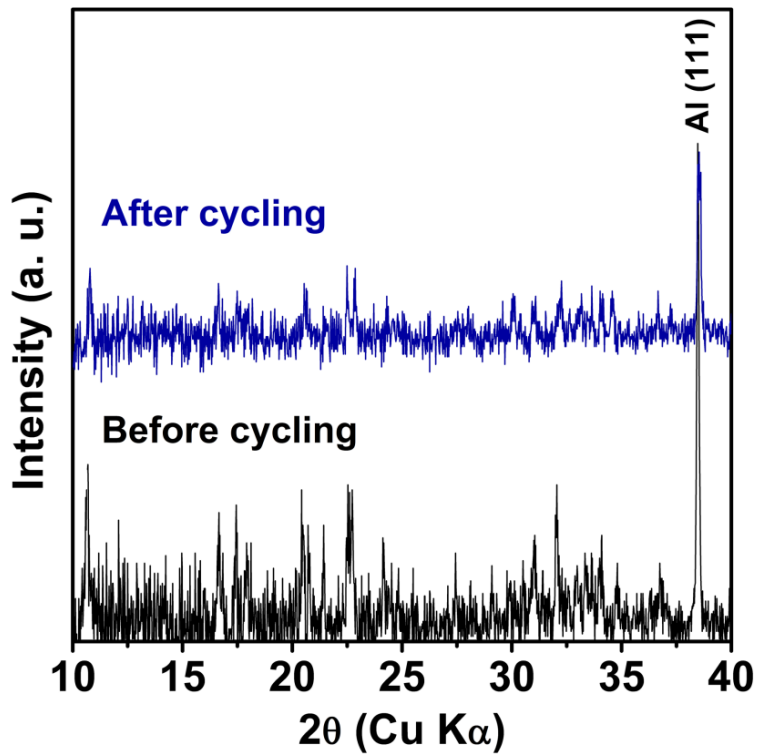


Figure 4.2.4 XRD patterns of M-Na₂FeP₂O₇-NPs/C before cycling and after 100 cycles.

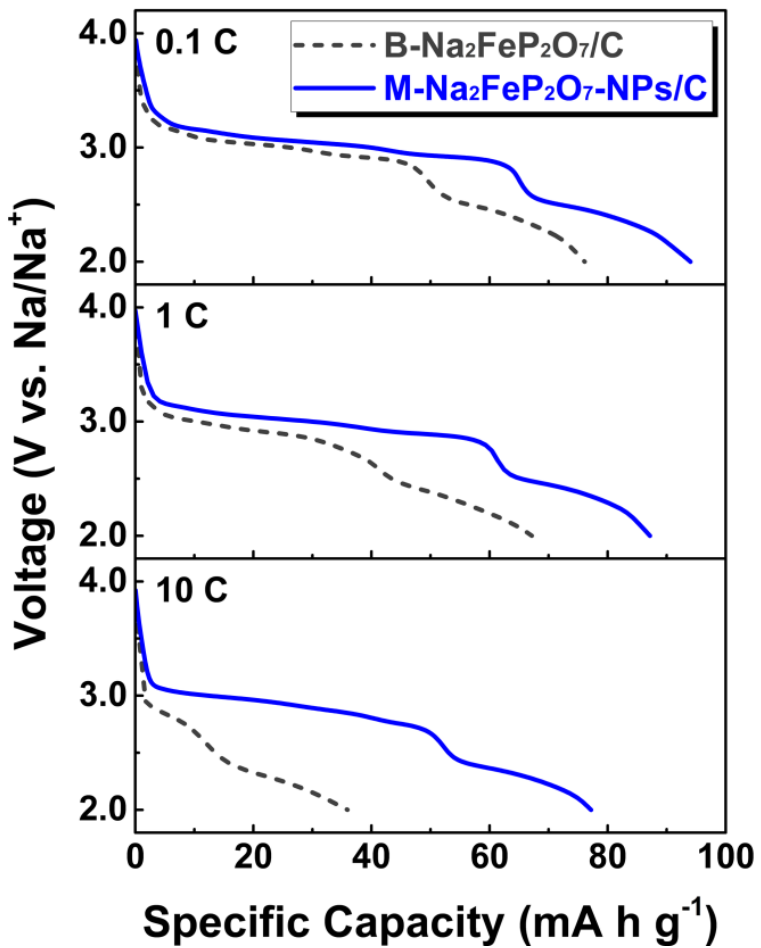


Figure 4.2.5 Comparison of rate capability of B- $\text{Na}_2\text{FeP}_2\text{O}_7/\text{C}$ and M- $\text{Na}_2\text{FeP}_2\text{O}_7$ -NPs/C at different rates of 0.1, 1 and 10 C.

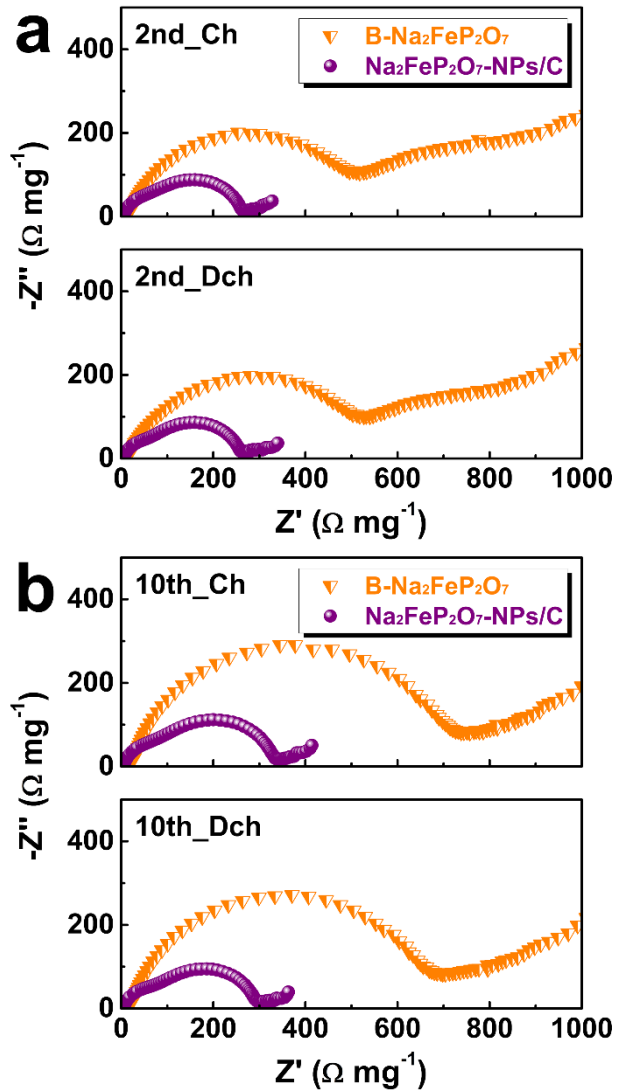


Figure 4.2.6 Nyquist plots for B-Na₂FeP₂O₇/C and Na₂FeP₂O₇-NPs/C at (a) 2nd and (b) 10th charged and discharged states at 3.0 V.

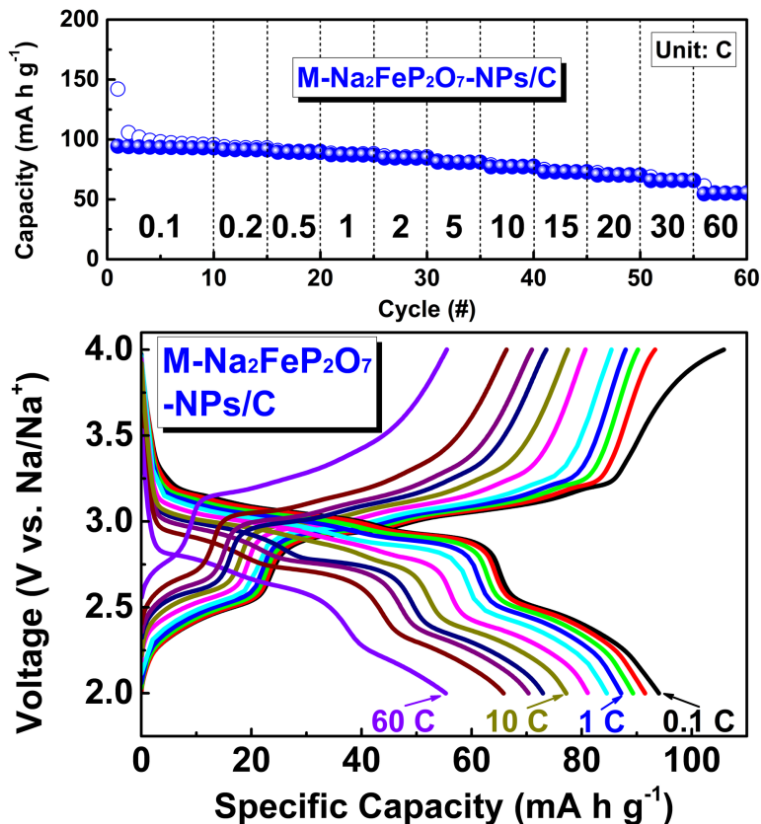


Figure 4.2.7 Rate capability of $\text{M-Na}_2\text{FeP}_2\text{O}_7\text{-NPs/C}$ at different rates from 0.1 to 60 C.

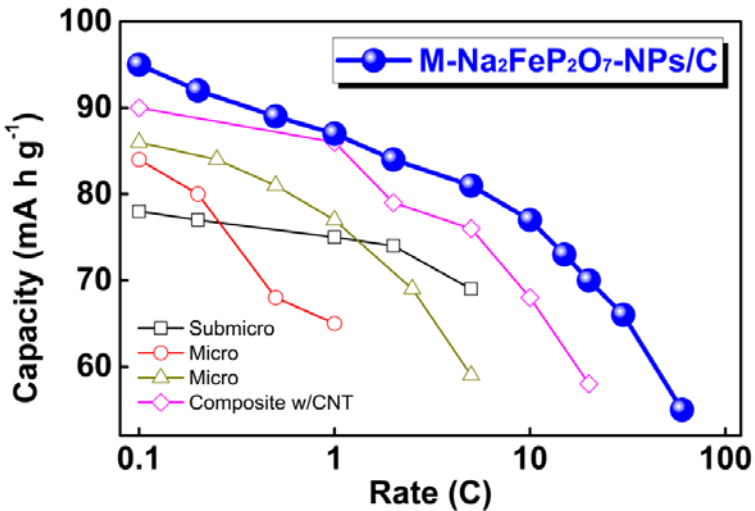


Figure 4.2.8 Comparison of rate performance to the recently results in the literature for Na₂FeP₂O₇.

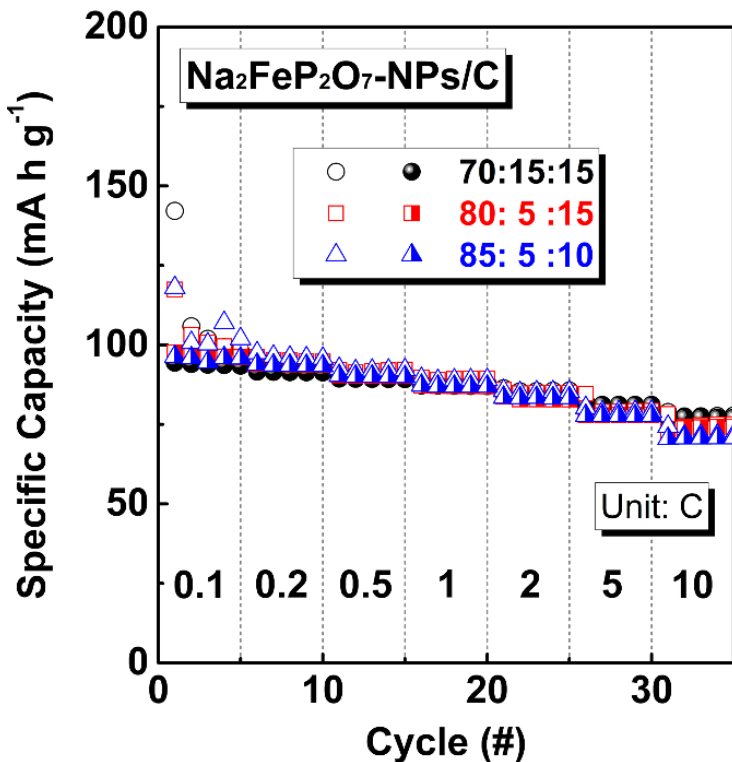


Figure 4.2.9 Rate capability of $\text{Na}_2\text{FeP}_2\text{O}_7$ -NPs/C with various ratios of active material, carbon black and binder at different rate from 0.1 to 10 C.

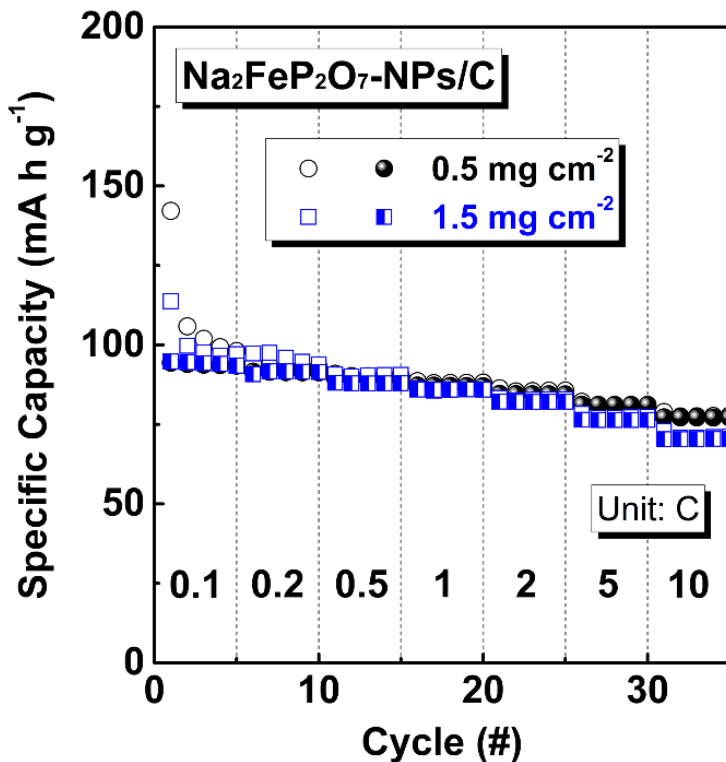


Figure 4.2.10 Rate capability of $\text{Na}_2\text{FeP}_2\text{O}_7\text{-NPs/C}$ w with different loading of active material at different rate from 0.1 to 10 C.

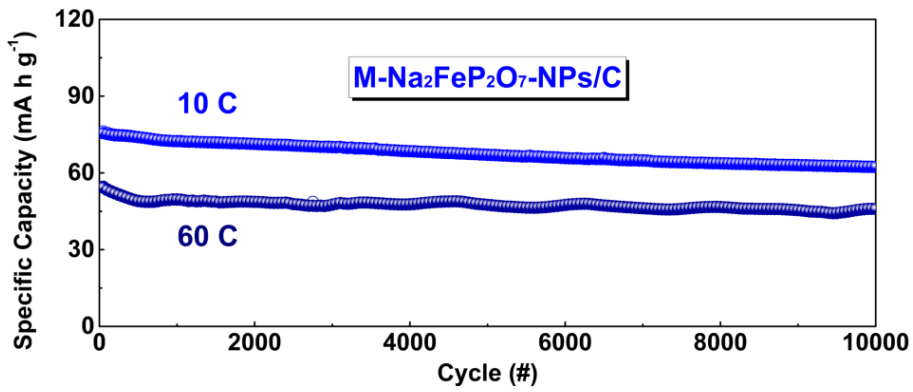


Figure 4.2.11 Long-term cyclability of M-Na₂FeP₂O₇-NPs/C at both 10 and 60 C.

4.3 Na_{3.12}Fe_{2.44}(P₂O₇)₂/C Nanocomposites

4.3.1 Na_{3.12}Fe_{2.44}(P₂O₇)₂/C Nanocomposite for Na-Ion Batteries

Synthesis of Na_{3.12}Fe_{2.44}(P₂O₇)₂-NPs/C

Due to more electrochemical Fe²⁺/Fe³⁺ redox reaction in Na_{3.12}Fe_{2.44}(P₂O₇)₂ when charging/discharging, theoretical capacity of Na_{3.12}Fe_{2.44}(P₂O₇)₂ (117 mA h g⁻¹) is higher than that of Na₂FeP₂O₇ (97 mA h g⁻¹), resulting in increase of energy density. So, Na_{3.12}Fe_{2.44}(P₂O₇)₂/C nanocomposite (Na_{3.12}Fe_{2.44}(P₂O₇)₂-NPs/C) was synthesized for the same synthetic process.

Figure 4.3.1 shows the FESEM images of Na_{3.12}Fe_{2.44}(P₂O₇)₂-NPs/C. Similar to Na₂FeP₂O₇-NPs/C, less-agglomerated and uniform-sized Na_{3.12}Fe_{2.44}(P₂O₇)₂-NPs/C was synthesized after HT→BM→HT process (Figure 4.3.1a and 4.3.1b). Figure 4.3.2 shows the XRD pattern of the Na_{3.12}Fe_{2.44}(P₂O₇)₂-NPs/C. All reflection peaks in the patterns were in agreement with those of the Na_{3.12}Fe_{2.44}(P₂O₇)₂ reference data (JCPDS No. 12-4802; triclinic polymorph). The atomic ratio of Na/Fe/P in Na_{3.12}Fe_{2.44}(P₂O₇)₂/C was measured to be 3.22:2.43:4.00 by ICP-OES (Table 4.3.1). That is, phase-pure Na_{3.12}Fe_{2.44}(P₂O₇)₂/C were successfully synthesized.

Na_{3.12}Fe_{2.44}(P₂O₇)₂-NPs/C for NIBs

Figure 4.3.3 shows the CV of Na_{3.12}Fe_{2.44}(P₂O₇)₂-NPs/C measured at a scan rate of 0.05 mV s⁻¹ to identify the electrochemical reactions. It can be seen

that well-defined redox peaks in CV which were consistent with previous study [4.8]. Also, all redox peaks remained unchanged after the 1st scan, indicative of a fairly high intercalation/deintercalation reversibility of Na-ions in $\text{Na}_{3.12}\text{Fe}_{2.44}(\text{P}_2\text{O}_7)_2$ -NPs/C.

Figure 4.3.4 shows the cyclic performance of $\text{Na}_{3.12}\text{Fe}_{2.44}(\text{P}_2\text{O}_7)_2$ -NPs/C and its similar compound, $\text{Na}_2\text{FeP}_2\text{O}_7$ -NPs/C measured up to 100th cycle at 0.2 C. Specific capacity of $\text{Na}_{3.12}\text{Fe}_{2.44}(\text{P}_2\text{O}_7)_2$ -NPs/C was measured to be 107 mA h g⁻¹ which is higher than that of $\text{Na}_2\text{FeP}_2\text{O}_7$ -NPs/C (95 mA h g⁻¹). So, it is confirmed that $\text{Na}_{3.12}\text{Fe}_{2.44}(\text{P}_2\text{O}_7)_2$ exhibits more electrochemical $\text{Fe}^{2+}/\text{Fe}^{3+}$ redox reaction than $\text{Na}_{3.12}\text{Fe}_{2.44}(\text{P}_2\text{O}_7)_2$. Likewise, $\text{Na}_{3.12}\text{Fe}_{2.44}(\text{P}_2\text{O}_7)_2$ -NPs/C exhibited higher specific capacity at low rates, but its rate performance was less-impressive than $\text{Na}_2\text{FeP}_2\text{O}_7$ -NPs/C (Figure 4.3.5), possibly due to the Fe defect in Na site resulting from the Fe-excess in $\text{Na}_{3.12}\text{Fe}_{2.44}(\text{P}_2\text{O}_7)_2$, which has the possibility to interrupt the migration of Na-ion.

In order to identify this, Na-ion intercalation kinetics of the $\text{Na}_2\text{FeP}_2\text{O}_7$ -NPs/C and $\text{Na}_{3.12}\text{Fe}_{2.44}(\text{P}_2\text{O}_7)_2$ -NPs/C are investigated by GITT measurements. Figure 4.3.6a-b show the GITT curves and corresponding quasi open-circuit voltage (QOCV) curves of the $\text{Na}_2\text{FeP}_2\text{O}_7$ -NPs/C and $\text{Na}_{3.12}\text{Fe}_{2.44}(\text{P}_2\text{O}_7)_2$ -NPs/C, respectively. The apparent Na-ion diffusion coefficients (D_{Na}) are calculated based on the GITT results according to the modified Fick's second law as below equation; [4.9]

$$D_{Na} = \frac{4}{\pi\tau} \left(\frac{m_B V_M}{M_B S}\right)^2 \left(\frac{\Delta E_s}{\Delta E_t}\right)^2$$

where τ is the constant current pulse time, m_B , V_M , and M_B are the mass, the molar volume, and the molar mass of the insertion electrode material, respectively, S is the area of the electrode–electrolyte interface, ΔE_s the change of the steady-state voltage during a single-step GITT experiment, and ΔE_t the total change of cell voltage during a constant current pulse τ of a single-step GITT experiment neglecting the IR-drop.

Figure 4.3.7a-b show the variation of D_{Na} values as a function of voltage for $Na_2FeP_2O_7$ -NPs/C and $Na_{3.12}Fe_{2.44}(P_2O_7)_2$ -NPs/C when charging and discharging, respectively. The D_{Na} values of $Na_2FeP_2O_7$ -NPs/C were measured to be higher than those of $Na_{3.12}Fe_{2.44}(P_2O_7)_2$ -NPs/C in both charged and discharged state except for near 3.3 V. Figure 4.3.7a-b show the variation of D_{Na} values as a function of voltage for $Na_2FeP_2O_7$ -NPs/C and $Na_{3.12}Fe_{2.44}(P_2O_7)_2$ -NPs/C when charging and discharging, respectively. The D_{Na} values of $Na_2FeP_2O_7$ -NPs/C were measured to be higher than those of $Na_{3.12}Fe_{2.44}(P_2O_7)_2$ -NPs/C in both charged and discharged state except for near 3.3 V. In other words, Na-ions can move more favorably in $Na_2FeP_2O_7$ -NPs/C than $Na_{3.12}Fe_{2.44}(P_2O_7)_2$ -NPs/C which affected the different rate performance in both composites.

Table 4.3.1 Atomic ratio of Na, Fe, and P in $\text{Na}_{3.12}\text{Fe}_{2.44}(\text{P}_2\text{O}_7)_2$ -NPs/C by ICP analysis.

Sample	Element	# of Moles	Atomic Ratio
$\text{Na}_{3.12}\text{Fe}_{2.44}(\text{P}_2\text{O}_7)_2$ -NPs/C	Na	1.306	3.22
	Fe	0.984	2.43
	P	1.620	4.00

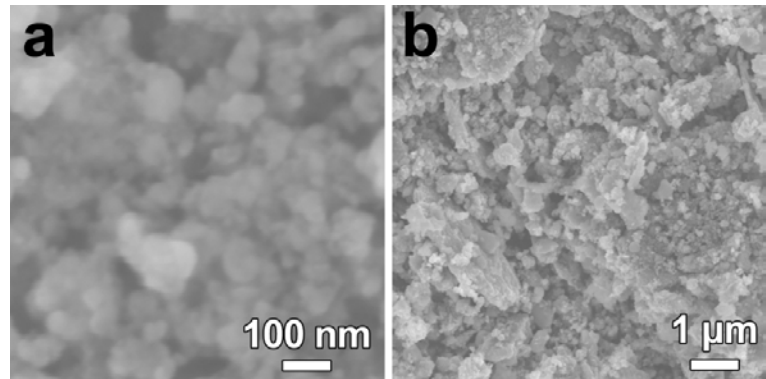


Figure 4.3.1 (a-b) High- and low-magnification FESEM images of M-
 $\text{Na}_{3.12}\text{Fe}_{2.44}(\text{P}_2\text{O}_7)_2$ -NPs/C.

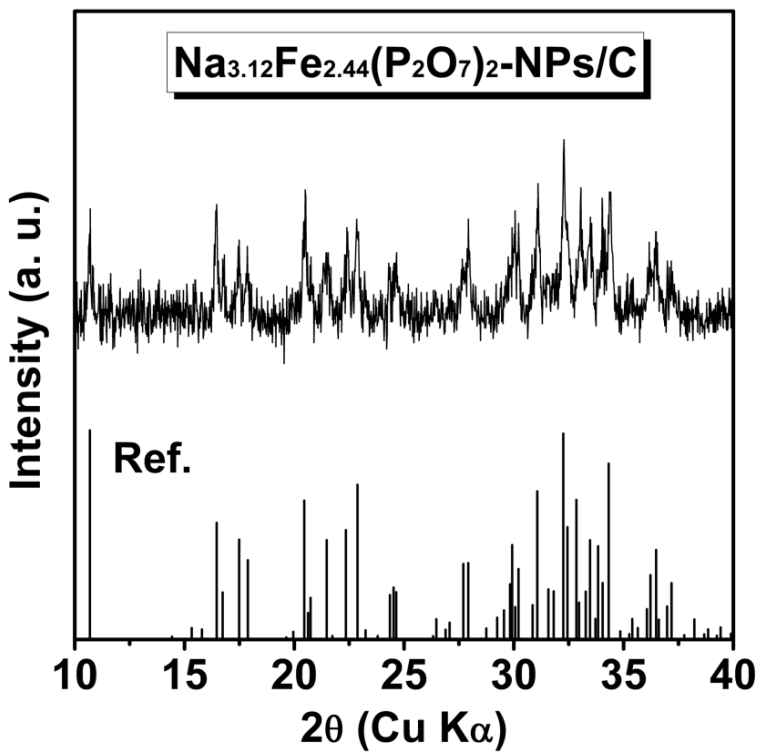


Figure 4.3.2 XRD pattern of Na_{3.12}Fe_{2.44}(P₂O₇)₂-NPs/C.

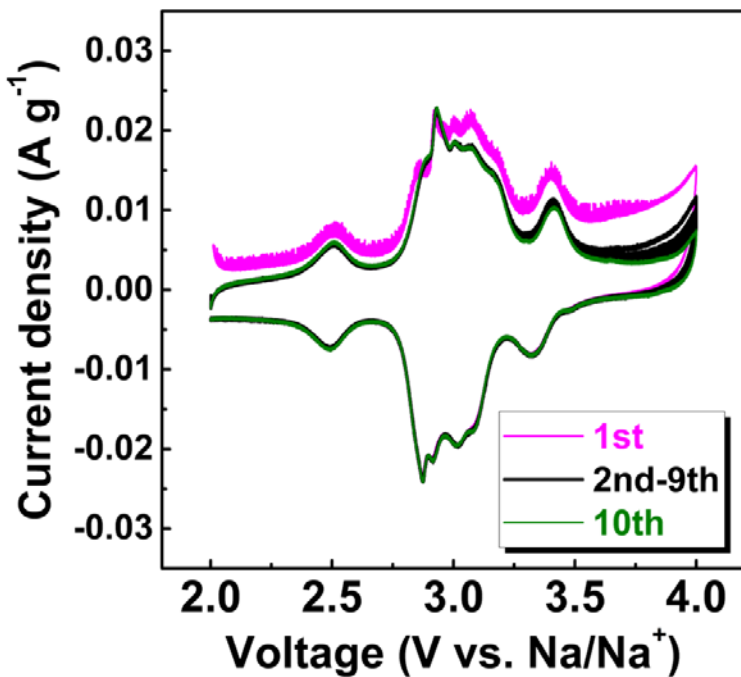


Figure 4.3.3 Cyclic voltammetry of $\text{Na}_{3.12}\text{Fe}_{2.44}(\text{P}_2\text{O}_7)_2$ -NPs/C at a scan rate of 0.05 mV s^{-1} .

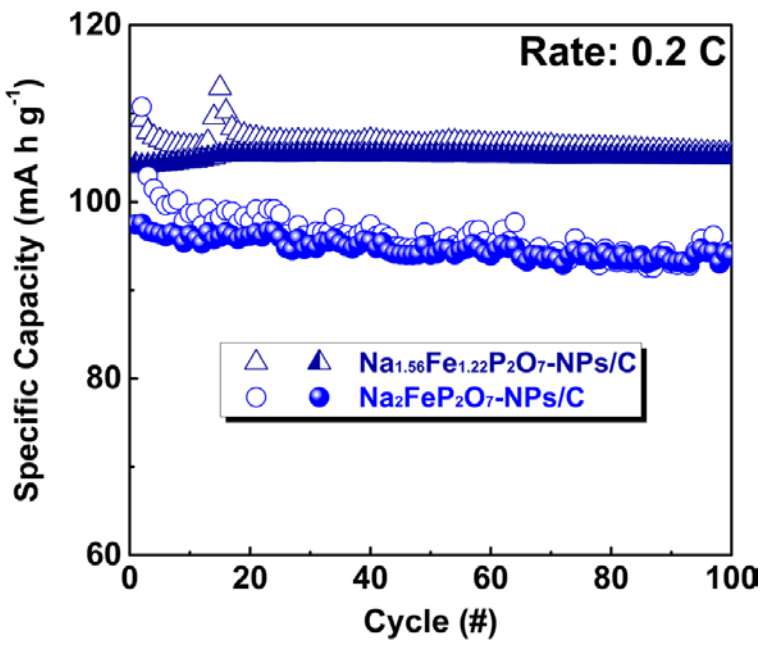


Figure 4.3.4 Comparison of specific capacity between $\text{Na}_2\text{FeP}_2\text{O}_7\text{-NPs/C}$ and $\text{Na}_{3.12}\text{Fe}_{2.44}(\text{P}_2\text{O}_7)_2\text{-NPs/C}$ at 0.2 C.

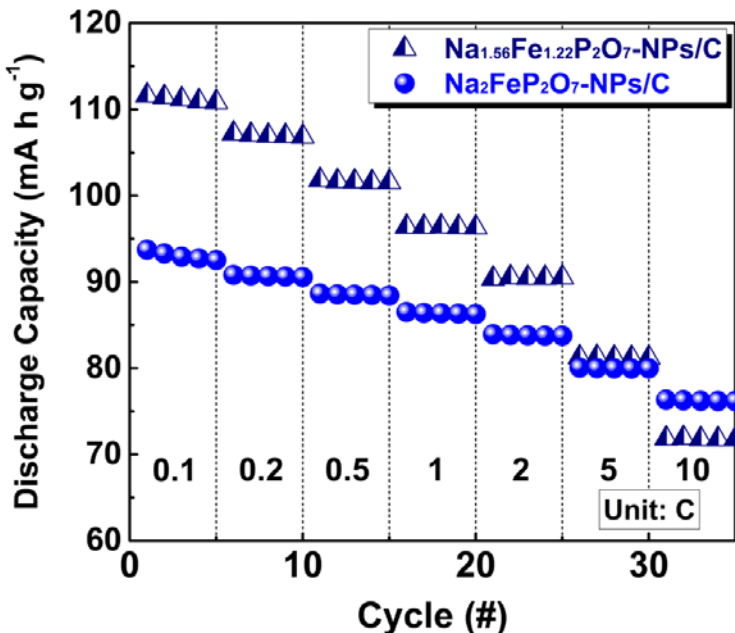


Figure 4.3.5 Comparison of rate capability between Na₂FeP₂O₇-NPs/C and Na_{3.12}Fe_{2.44}(P₂O₇)₂-NPs/C from 0.1 to 10 C.

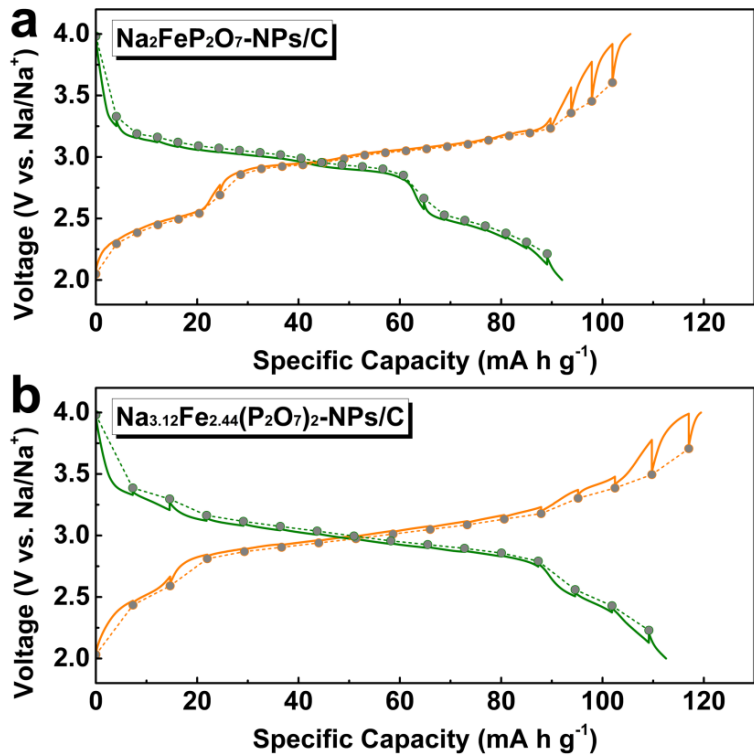
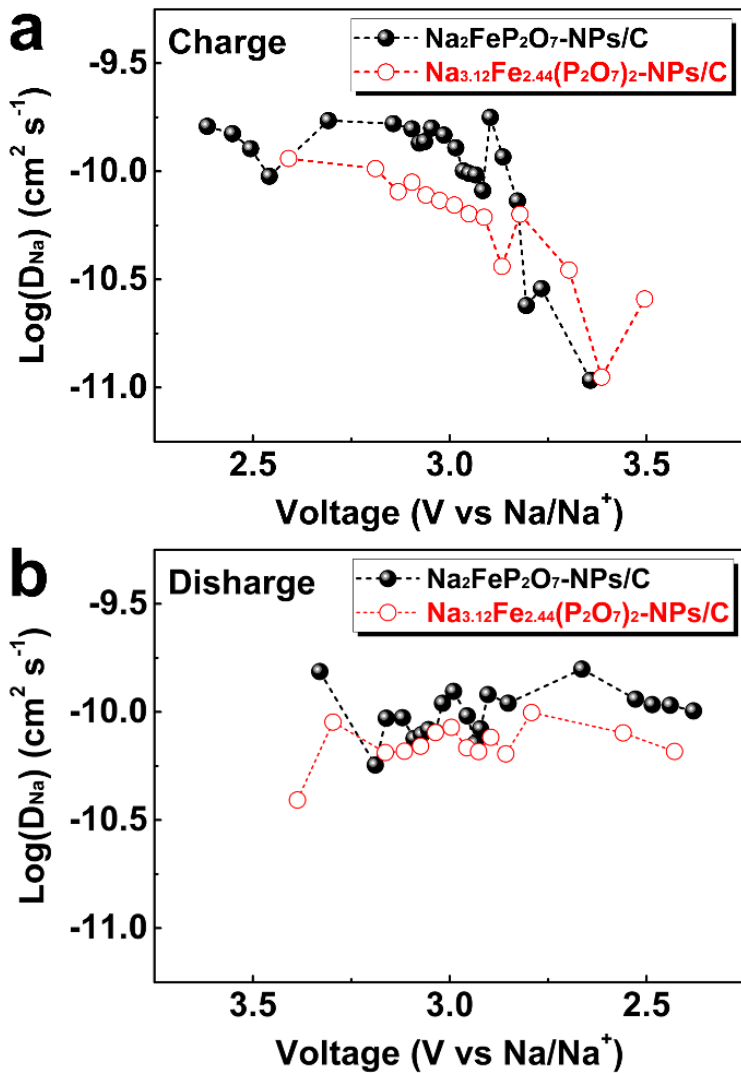


Figure 4.3.6 GITT and corresponding QOCP curves of the (a) Na₂FeP₂O₇-NPs/C and (b) Na_{3.12}Fe_{2.44}(P₂O₇)₂-NPs/C.



4.3.2 Na_{3.12}Fe_{2.44}(P₂O₇)₂/C/rGO Nanocomposite for Na-Ion Batteries

Synthesis of Na_{3.12}Fe_{2.44}(P₂O₇)₂-NPs/C/rGO

Small amount of rGO was added in Na_{3.12}Fe_{2.44}(P₂O₇)₂-NPs/C to improve the electrical conductivity of composite. Figure 4.3.8 shows the morphology and size of Na_{3.12}Fe_{2.44}(P₂O₇)₂-NPs/C/rGO. Less-agglomerated and uniform-sized Na_{3.12}Fe_{2.44}(P₂O₇)₂-NPs/C were obtained after HT→BM→HT process. Also shown in Figure 4.3.8b, it can be seen that rGO was well mixed in Na_{3.12}Fe_{2.44}(P₂O₇)₂-NPs/C to form the Na_{3.12}Fe_{2.44}(P₂O₇)₂-NPs/C/rGO composite.

Figures 4.3.9a show a TEM image of Na_{3.12}Fe_{2.44}(P₂O₇)₂-NPs/C/rGO after the sol-gel and subsequent HT→BM→HT processes. The sheet-like GO used in this study had a size of less than 1 μm (Figure 4.3.9b). Further, as can be seen from Figure 4.3.9a, Na_{3.12}Fe_{2.44}(P₂O₇)₂-NPs/C is well-incorporated on the surfaces of the rGO sheets. In addition, it can be seen that the Na_{3.12}Fe_{2.44}(P₂O₇)₂ NPs are smaller than 50 nm and are surrounded by tiny flakes of amorphous carbon (Figure 4.3.9c). The high-resolution TEM image in Figure 4.3.9d (corresponding to the area marked in red in Figure 4.3.9c) shows clearly that lattice fringes are present in all the regions, indicating the high crystallinity of the NPs without an amorphous layer. The lattice spacing, which is 0.41 nm and corresponds to the (022) plane, is consistent with the d-spacing of the Na_{3.12}Fe_{2.44}(P₂O₇)₂ structure.

Figure 4.3.10 shows the XRD patterns of the $\text{Na}_{3.12}\text{Fe}_{2.44}(\text{P}_2\text{O}_7)_2$ -NPs/C/rGO. All the reflection peaks in the patterns agree with those of $\text{Na}_{3.12}\text{Fe}_{2.44}(\text{P}_2\text{O}_7)_2$ given in the reference data (JCPDS No. 12-4802; triclinic unit cell). The Na/Fe/P atomic ratios in $\text{Na}_{3.12}\text{Fe}_{2.44}(\text{P}_2\text{O}_7)_2$ -NPs/C/rGO were measured to be 3.22:2.43:4.00 and 3.29:2.39:4.00, respectively, using ICP-OES (Table 4.3.2). From these results, it can be concluded that $\text{Na}_{3.12}\text{Fe}_{2.44}(\text{P}_2\text{O}_7)_2$ -NPs/C/rGO were synthesized successfully. Meanwhile, based on the Debye-Scherrer equation, the grain size for $\text{Na}_{3.12}\text{Fe}_{2.44}(\text{P}_2\text{O}_7)_2$ -NPs was calculated to be 40 nm, which was consistent with the results of the SEM and TEM analyses. Thus, it can be concluded that GO did not affect the formation of the $\text{Na}_{3.12}\text{Fe}_{2.44}(\text{P}_2\text{O}_7)_2$ -NPs.

To confirm the reduction of GO, the XPS spectra of $\text{Na}_{3.12}\text{Fe}_{2.44}(\text{P}_2\text{O}_7)_2$ -NPs/C/rGO were investigated. The C 1s level XPS spectrum of pristine GO generally shows strong peaks related to oxygen-containing functional groups such as the C-O, C=O and O-C=O groups [4.10,4.11]. However, as can be seen from Figure 4.3.11, the intensities of the peaks related to these groups are significantly lower in the case of the $\text{Na}_{3.12}\text{Fe}_{2.44}(\text{P}_2\text{O}_7)_2$ -NPs/C/rGO sample. In contrast, a strong C=C (284.5 eV) peak is still observed, indicating the successful reduction of GO to rGO through the reduction-atmosphere HT process.

Figure 4.3.12 shows the nitrogen adsorption (solid symbols)-desorption (open symbols) isotherms of the samples measured at 77 K. The specific surface

area of $\text{Na}_{3.12}\text{Fe}_{2.44}(\text{P}_2\text{O}_7)_2$ -NPs/C, determined using the BET model, was estimated to be $70 \text{ m}^2 \text{ g}^{-1}$. A surface area this large can be attributed to not only the low degree of agglomeration of $\text{Na}_{3.12}\text{Fe}_{2.44}(\text{P}_2\text{O}_7)_2$ -NPs/C but also to the tiny carbon flakes surrounding $\text{Na}_{3.12}\text{Fe}_{2.44}(\text{P}_2\text{O}_7)_2$ -NPs/C, as is evident from the SEM and TEM images. Moreover, the specific surface area of $\text{Na}_{3.12}\text{Fe}_{2.44}(\text{P}_2\text{O}_7)_2$ -NPs/C/rGO was even higher at $102 \text{ m}^2 \text{ g}^{-1}$, owing to the incorporation of the two-dimensional rGO, which is known to have a large surface area [4.12]. Meanwhile, the overall carbon contents in the $\text{Na}_{3.12}\text{Fe}_{2.44}(\text{P}_2\text{O}_7)_2$ -NPs/C and $\text{Na}_{3.12}\text{Fe}_{2.44}(\text{P}_2\text{O}_7)_2$ -NPs/C/rGO samples were estimated to be 16–17 and 19–19.5 wt%, respectively, from the TG (Figure 4.3.13) and elemental analyses. Based on these results, the rGO content of the NFP-NPs/C/rGO composite was determined to be approximately 3 wt%.

$\text{Na}_{3.12}\text{Fe}_{2.44}(\text{P}_2\text{O}_7)_2$ -NPs/C/rGO for NIBs

Figure 4.3.14a shows the galvanostatic charging/discharging profiles and rate capabilities of $\text{Na}_{3.12}\text{Fe}_{2.44}(\text{P}_2\text{O}_7)_2$ -NPs/C/rGO at different rates (0.1–10 C). When the measurements were performed at 0.1 C, plateaus were observed in the voltage profiles at approximately 2.5, 3.0, and 3.3 V; these were in good agreement with the redox peaks seen in the CV curves. With an increase in the C-rate to 0.1, 0.2, 0.5, 1, 2, 5, and 10 C (5 cycles were performed at each rate), the discharge capacities of $\text{Na}_{3.12}\text{Fe}_{2.44}(\text{P}_2\text{O}_7)_2$ -NPs/C/rGO were measured to be 109, 104, 100, 96, 92, 85, and 78 mA h g^{-1} , respectively. This superior rate

capability of $\text{Na}_{3.12}\text{Fe}_{2.44}(\text{P}_2\text{O}_7)_2$ -NPs/C/rGO can be attributed to the nanoscale size of NFP-NPs/C/rGO and the proper embedding of carbon in them. [4.13] Further, as shown in Figures 4.3.14b, $\text{Na}_{3.12}\text{Fe}_{2.44}(\text{P}_2\text{O}_7)_2$ -NPs/C/rGO displays a smaller decrease in capacity as compared to $\text{Na}_{3.12}\text{Fe}_{2.44}(\text{P}_2\text{O}_7)_2$ -NPs/C even at high rates, indicating that the rate capability was improved with the addition of rGO to $\text{Na}_{3.12}\text{Fe}_{2.44}(\text{P}_2\text{O}_7)_2$ -NPs/C. The difference in the capacities of $\text{Na}_{3.12}\text{Fe}_{2.44}(\text{P}_2\text{O}_7)_2$ -NPs/C and $\text{Na}_{3.12}\text{Fe}_{2.44}(\text{P}_2\text{O}_7)_2$ -NPs/C/rGO increased gradually as the C-rate was increased to 2, 5, and 10 C (green region in Figure 4.3.14b). Thus, one can surmise that the addition of even a small amount of rGO to $\text{Na}_{3.12}\text{Fe}_{2.44}(\text{P}_2\text{O}_7)_2$ -NPs/C can induce a capacity improvement of 10% at a high rate (10 C).

It is likely that the observed improvement in the rate performance is caused by the increase in the electrical conductivity resulting from the lowering of the charge-transfer resistance by the addition of rGO. Thus, in order to compare the charge-transfer resistances of $\text{Na}_{3.12}\text{Fe}_{2.44}(\text{P}_2\text{O}_7)_2$ -NPs/C and $\text{Na}_{3.12}\text{Fe}_{2.44}(\text{P}_2\text{O}_7)_2$ -NPs/C/rGO, EIS measurements were performed at frequencies ranging from 100 kHz to 10 mHz. Smaller semicircles in the high-frequency region indicate a lower charge-transfer resistance (R_{ct}) at the electrode/electrolyte interface. As can be seen from the Nyquist plots in Figure 4.3.15, the plot of $\text{Na}_{3.12}\text{Fe}_{2.44}(\text{P}_2\text{O}_7)_2$ -NPs/C/rGO contains smaller semicircles than does that of $\text{Na}_{3.12}\text{Fe}_{2.44}(\text{P}_2\text{O}_7)_2$ -NPs/C after the 1st charging cycle. Through fitting, the R_{ct} values of $\text{Na}_{3.12}\text{Fe}_{2.44}(\text{P}_2\text{O}_7)_2$ -NPs/C and $\text{Na}_{3.12}\text{Fe}_{2.44}(\text{P}_2\text{O}_7)_2$ -

NPs/C/rGO after the 1st, 5th, and 10th charging cycles were estimated to be 1750, 1648, and 1648, respectively, and 746, 1488, and 1418 Ω, respectively. Thus, the addition of rGO, which exhibits high electrical conductivity, ensured that charge transfer in the NFP-NPs/C/rGO electrode was faster than that in the NFP-NPs/C electrode, owing to faster faradic reaction kinetics and higher capacity in the former case, especially at high rates [4.14].

Finally, the long-term cyclic performances of the two electrode materials were investigated. As expected, Na_{3.12}Fe_{2.44}(P₂O₇)₂-NPs/C/rGO showed a higher specific capacity and more stable cyclability than did Na_{3.12}Fe_{2.44}(P₂O₇)₂-NPs, meaning that rGO has a positive effect on the long-term cyclic performance (Figure 4.3.16a). In addition, as shown in Figure 4.3.16b, Na_{3.12}Fe_{2.44}(P₂O₇)₂-NPs/C/rGO exhibited long-term cyclic stability at 10 C after 5000 cycles, with the capacity retention being 70% (capacity degradation of 0.0076% per cycle).

The rate and cyclic performances shown by Na_{3.12}Fe_{2.44}(P₂O₇)₂-NPs/C/rGO are among the best for Na₂FeP₂O₇- and Na_{3.12}Fe_{2.44}(P₂O₇)₂-based cathode materials for nonaqueous NIBs (Table 4.3.3). [4.1,4.2,4.5,4.6,4.8,4.15-4.18] In addition, the Na_{3.12}Fe_{2.44}(P₂O₇)₂-NPs/C/rGO composite synthesized in this study meets some of the critical requirements determining suitability for use as a cathode material in large-scale electrical energy storage systems: the low costs and high abundance of the constituent elements (Na, Fe, and P); relatively high specific capacity (109 mA h g⁻¹); superior rate capability at high

rates; and long-term cyclic stability. Therefore, it is suggested that the synthesis strategy used in this study is an effective one for ensuring both high sodium intercalation kinetics and good long-term cyclic performance in NIB electrodes.

Table 4.3.2 Atomic ratio of Na, Fe, and P in $\text{Na}_{3.12}\text{Fe}_{2.44}(\text{P}_2\text{O}_7)_2$ -NPs/C/rGO by ICP analysis.

Sample	Element	# of Moles	Atomic Ratio
$\text{Na}_{3.12}\text{Fe}_{2.44}(\text{P}_2\text{O}_7)_2$ -NPs/C/rGO	Na	1.338	3.29
	Fe	0.969	2.39
	P	1.624	4.00

Table 4.3.3 Comparison of the electrochemical performance with various reported $\text{Na}_2\text{FeP}_2\text{O}_7$ - and $\text{Na}_{3.12}\text{Fe}_{2.44}(\text{P}_2\text{O}_7)_2$ -based cathode materials for NIBs.

Material		Voltage (V)	Cycle (No.)	Rate (C)	Capacity (mAh g ⁻¹)	Ref.
$\text{Na}_2\text{FeP}_2\text{O}_7$	Submicron	2.0-4.0	10	0.05	82	[4.2]
$\text{Na}_2\text{FeP}_2\text{O}_7$	Micro	2.0-4.5	80	0.05	92	[4.1]
$\text{Na}_2\text{FeP}_2\text{O}_7$	Micro	2.0-3.8	50	0.05	80	[4.5]
$\text{Na}_2\text{FeP}_2\text{O}_7$	CNT composite	2.0-4.0	140	1	86	[4.6]
$\text{Na}_{3.12}\text{Fe}_{2.44}(\text{P}_2\text{O}_7)_2$	Micro	1.7-4.0	60	0.05	80	[4.15]
$\text{Na}_{3.12}\text{Fe}_{2.44}(\text{P}_2\text{O}_7)_2$	Graphene composite	1.7-4.0	80	0.2	100	[4.16]
$\text{Na}_{3.12}\text{Fe}_{2.44}(\text{P}_2\text{O}_7)_2$	CNT composite	1.7-4.0	120	0.15	100	[4.17]
$\text{Na}_{3.12}\text{Fe}_{2.44}(\text{P}_2\text{O}_7)_2$	Coral-like	2.0-4.0	200	5	80	[4.8]
$\text{Na}_{3.12}\text{Fe}_{2.44}(\text{P}_2\text{O}_7)_2$	Hollow microspheres	1.5-4.0	500	10	60	[4.18]

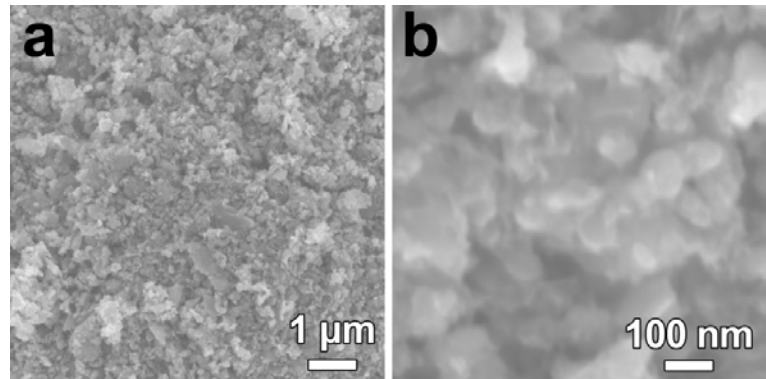


Figure 4.3.8 Low- and High-magnification FESEM images of M-
 $\text{Na}_{3.12}\text{Fe}_{2.44}(\text{P}_2\text{O}_7)_2$ -NPs/C/rGO.

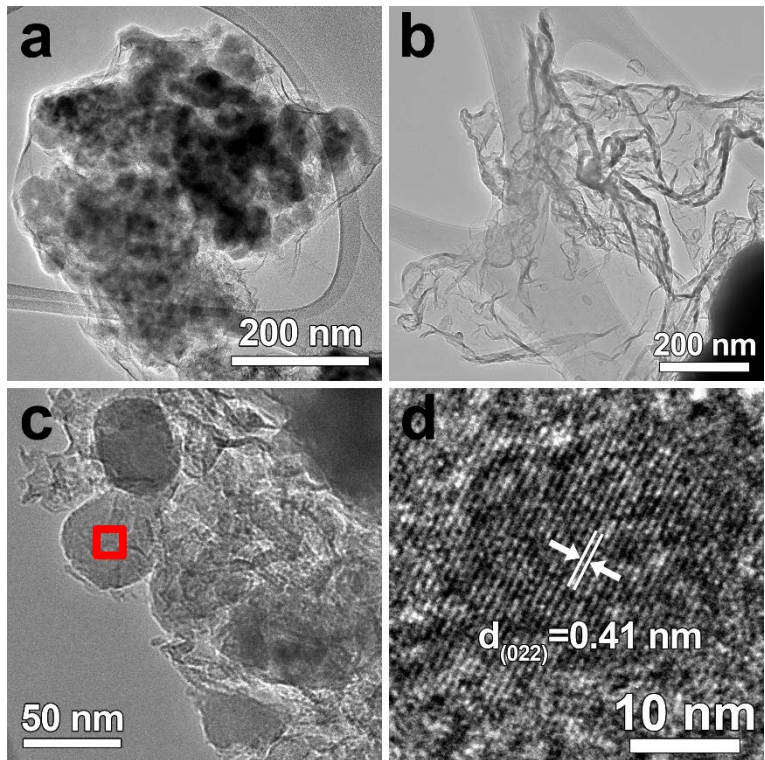


Figure 4.3.9 (a) TEM image of $\text{Na}_{3.12}\text{Fe}_{2.44}(\text{P}_2\text{O}_7)_2$ -NPs/C/rGO. (b) TEM image of GO. (c) TEM image of $\text{Na}_{3.12}\text{Fe}_{2.44}(\text{P}_2\text{O}_7)_2$ -NPs/C/rGO and HR image obtained from the marked region in (c).

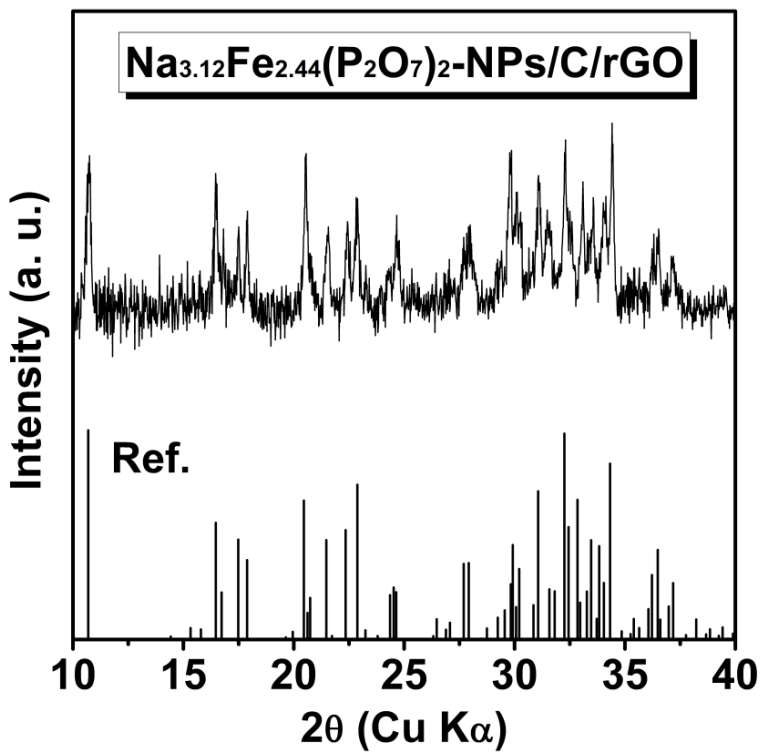


Figure 4.3.10 XRD pattern of Na_{3.12}Fe_{2.44}(P₂O₇)₂-NPs/C/rGO.

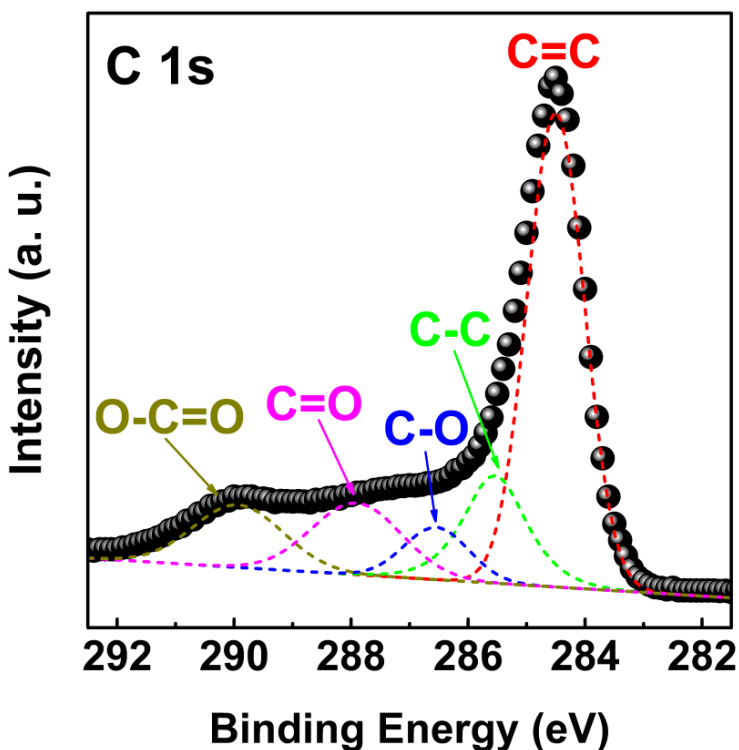


Figure 4.3.11 C 1s level XPS spectra of $\text{Na}_{3.12}\text{Fe}_{2.44}(\text{P}_2\text{O}_7)_2$ -NPs/C/rGO.

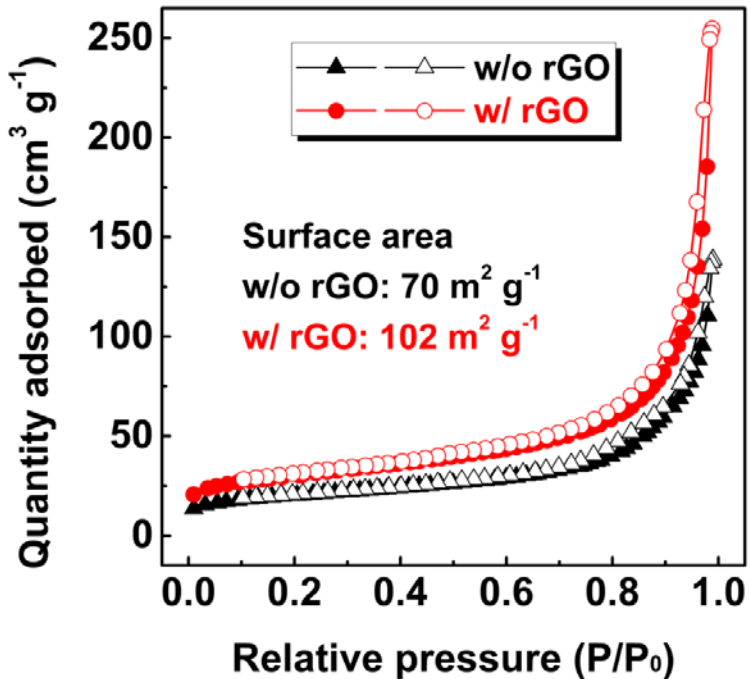


Figure 4.3.12 Nitrogen adsorption-desorption isotherms of $\text{Na}_{3.12}\text{Fe}_{2.44}(\text{P}_2\text{O}_7)_2$ -NPs/C and $\text{Na}_{3.12}\text{Fe}_{2.44}(\text{P}_2\text{O}_7)_2$ -NPs/C/rGO.

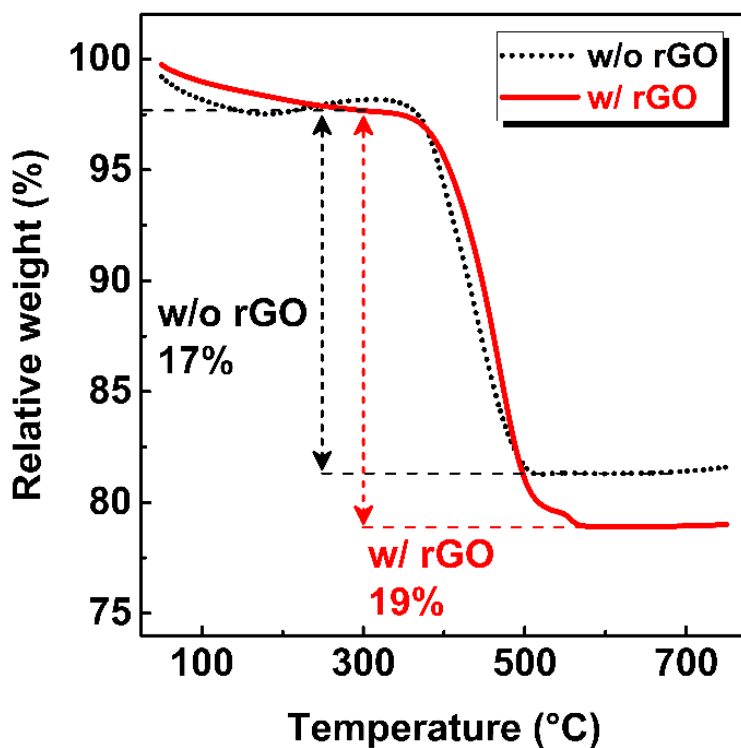


Figure 4.3.13 TGA (weight loss) curves of $\text{Na}_{3.12}\text{Fe}_{2.44}(\text{P}_2\text{O}_7)_2$ -NPs/C and $\text{Na}_{3.12}\text{Fe}_{2.44}(\text{P}_2\text{O}_7)_2$ -NPs/C/rGO.

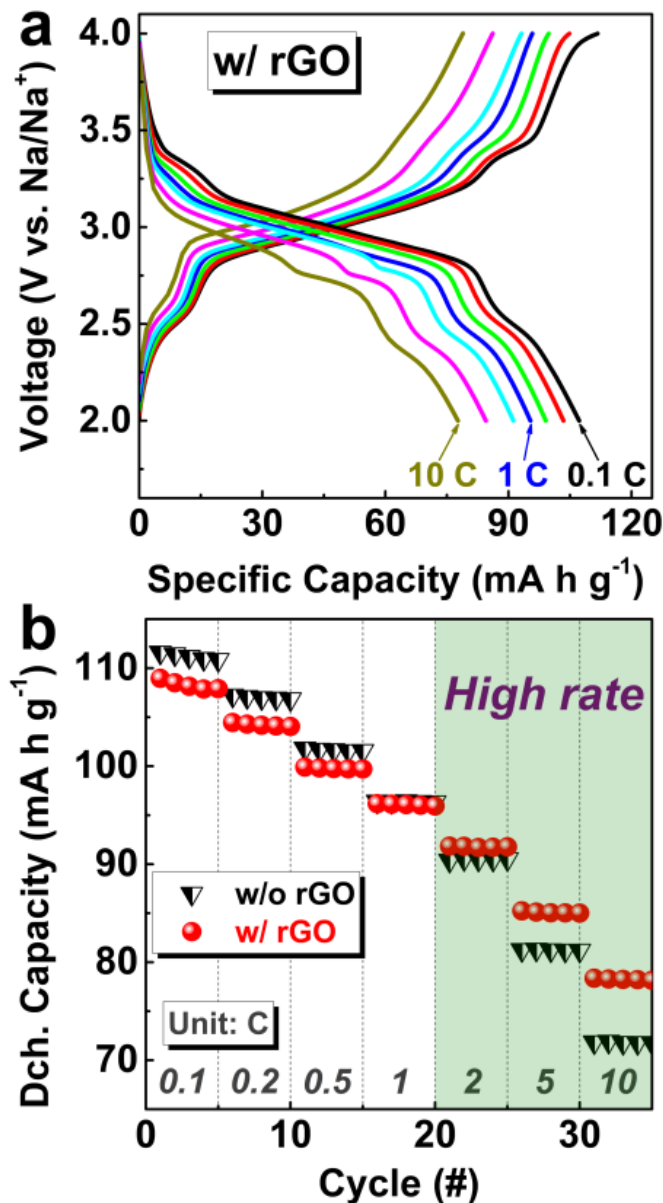


Figure 4.3.14 (a) Voltage–capacity profiles of $\text{Na}_{3.12}\text{Fe}_{2.44}(\text{P}_2\text{O}_7)_2\text{-NPs/C/rGO}$.
(b) Comparison of rate performance between $\text{Na}_{3.12}\text{Fe}_{2.44}(\text{P}_2\text{O}_7)_2\text{-NPs/C}$ and $\text{Na}_{3.12}\text{Fe}_{2.44}(\text{P}_2\text{O}_7)_2\text{-NPs/C/rGO}$ from 0.1 to 10 C.

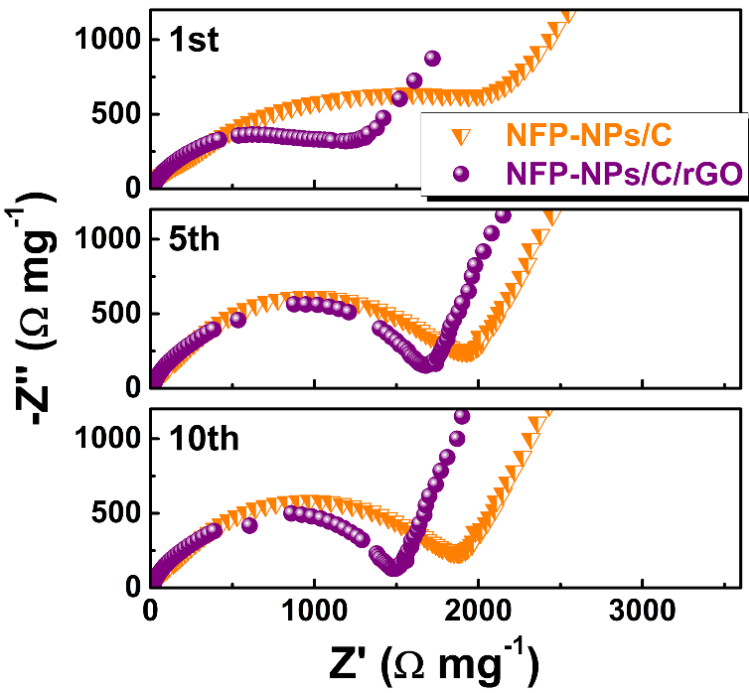


Figure 4.3.15 Nyquist plots for $\text{Na}_{3.12}\text{Fe}_{2.44}(\text{P}_2\text{O}_7)_2\text{-NPs/C}$ and $\text{Na}_{3.12}\text{Fe}_{2.44}(\text{P}_2\text{O}_7)_2\text{-NPs/C/rGO}$ at the 1st, 5th and 10th charged states.

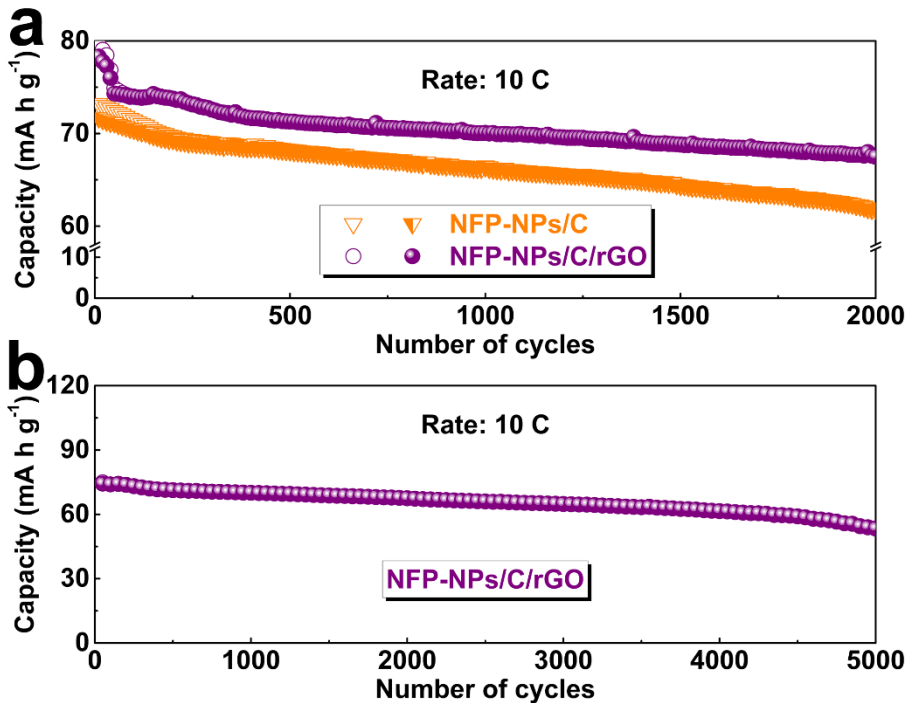


Figure 4.3.16 Comparison of long-term cyclability (a) between $\text{Na}_{3.12}\text{Fe}_{2.44}(\text{P}_2\text{O}_7)_2\text{-NPs/C}$ and $\text{Na}_{3.12}\text{Fe}_{2.44}(\text{P}_2\text{O}_7)_2\text{-NPs/C/rGO}$ at 10 C. (b) Further cyclic performance of $\text{Na}_{3.12}\text{Fe}_{2.44}(\text{P}_2\text{O}_7)_2\text{-NPs/C/rGO}$ up to 5000 cycles.

4.4 Bibliography

- [4.1] H. Kim, R. A. Shakoor, C. Park, S. Y. Lim, J.-S. Kim, Y. N. Jo, W. Cho, K. Miyasaka, R. Kahraman, Y. Jung, J. W. Choi, *Adv. Funct. Mater.*, **2013**, 23, 1147-1155.
- [4.2] P. Barpanda, T. Ye, S.-i. Nishimura, S.-C. Chung, Y. Yamada, M. Okubo, H. Zhou, A. Yamada, *Electrochim. Commun.*, **2012**, 24, 116-119.
- [4.3] P. Barpanda, G. Liu, C. D. Ling, M. Tamaru, M. Avdeev, S.-C. Chung, Y. Yamada, A. Yamada, *Chem. Mater.*, **2013**, 25, 3480-3487.
- [4.4] X. Zhou, G. Wu, G. Gao, C. Cui, H. Yang, J. Shen, B. Zhou, Z Zhang, *Electrochim. Acta*, **2012**, 74, 32-38.
- [4.5] T. Honma, N. Ito, T. Togashi, A. Sato, T. Komatsu, *J. Power Sources*, **2013**, 227, 31-34.
- [4.6] G. Longoni, J. E. Wang, Y. H. Jung, D. K. Kim, C. M. Mari, R. Ruffo, *J. Power Sources*, **2016**, 302, 61-69.
- [4.7] K. Saravanan , C. W. Mason , A. Rudola , K. H. Wong, P. Balaya, *Adv. Energy Mater.*, **2013**, 3, 444-450.
- [4.8] B. Lin, S. Zhang, C. Deng, *J. Mater. Chem. A*, **2016**, 4, 2550-2559.
- [4.9] E. Deiss, *Electrochim. Acta*, **2005**, 50, 2927-2932.
- [4.10] S. Park, J. An, J. R. Potts, A. Velamakanni, S. Murali, R. S. Ruoff, *Carbon*, **2011**, 49, 3019-3023.

- [4.11] H.-J. Shin, K. K. Kim, A. Benayad, S.-M. Yoon, H. K. Park, I.-S. Jung, M. H. Jin, H.-K. Jeong, J. M. Kim, J.-Y. Choi, Y. H. Lee, *Adv. Funct. Mater.*, **2009**, *19*, 1987-1992.
- [4.12] D. R. Dreyer, S. Park, C. W. Bielawski, R. S. Ruoff, *Chem. Soc. Rev.*, **2010**, *39*, 228-240.
- [4.13] G.-N. Zhu, Y.-G. Wang, Y.-Y. Xia, *Energy Environ. Sci.*, **2012**, *5*, 6652.
- [4.14] X. Zhou, G. Wu, G. Gao, C. Cui, H. Yang, J. Shen, B. Zhou, Z. Zhang, *Electrochim. Acta*, **2012**, *74*, 32-38.
- [4.15] K.-H. Ha, S. H. Woo, D. Mok, N.-S. Choi, Y. Park, S. M. Oh, Y. Kim, J. Kim, J. Lee, L. F. Nazar, K. T. Lee, *Adv. Energy Mater.*, **2013**, *3*, 770-776.
- [4.16] Y. Niu, M. Xu, S. J. Bao, C. M. Li, *Chem. Commun.*, **2015**, *51*, 13120-13122.
- [4.17] Y. Niu, M. Xu, C. Cheng, S. Bao, J. Hou, S. Liu, F. Yi, H. He, C. M. Li, *J. Mater. Chem. A*, **2015**, *3*, 17224-17229.
- [4.18] B. Lin, Q. Li, B. Liu, S. Zhang, C. Deng, *Nanoscale*, **2016**, *8*, 8178-8188.

Chapter 5. Co-Based Pyrophosphate

5.1 Experiments

Synthesis of Co-based Pyrophosphates

Solid-state reaction

All chemicals were obtained as reagent grade and used without further purification. Micro-sized $\text{Na}_{2-2x}\text{Co}_{1+x}\text{P}_2\text{O}_7$ series were synthesized by a conventional solid-state reaction method. The starting materials were Na_2CO_3 (99%, Kojundo), CoO (99%, Acros Organics) and $\text{NH}_4\text{H}_2\text{PO}_4$ (98%, Sigma-Aldrich). After the starting materials were mixed in a polypropylene bottle with ZrO_2 balls and absolute ethanol (99.9%, Daejung) as a medium for 24 h, they were dried and ground by an agate mortar. The mixture was heat-treated in a tube furnace at 500-680 °C for 1-6 h under inert atmosphere flowing Ar gas. Carbon-coated micro-sized $\text{Na}_{1.8}\text{Co}_{1.1}\text{P}_2\text{O}_7$ were synthesized by a 2-step process. The as-synthesized $\text{Na}_{1.8}\text{Co}_{1.1}\text{P}_2\text{O}_7$ was mixed with graphite in 7:3 weight ratio with ZrO_2 balls and ethanol for 24 h, and then drying.

Sol-gel synthesis

All chemicals were obtained as reagent grade and used without further purification. $\text{Na}_{2-2x}\text{Co}_{1+x}\text{P}_2\text{O}_7/\text{C}$ nanocomposites were synthesized via a sol-gel method using citric acid as a chelating agent as well as a carbon source. In a

typical synthesis, metal-acetate source $\text{Co}(\text{CH}_3\text{COO})_2 \cdot 4\text{H}_2\text{O}$ (98%, Sigma-Aldrich), and citric acid (CA; 99.5%, Sigma-Aldrich) were dissolved in 50 mL of distilled water. $\text{Na}(\text{CH}_3\text{COO})$ (99%, Sigma-Aldrich) and $\text{NH}_4\text{H}_2\text{PO}_4$ (98%, Sigma-Aldrich) were dissolved in another 50 mL of distilled water. These two solutions were then mixed in a three-neck round-bottom flask, and then, refluxed at 80 °C for 12 h under magnetic stirring. After reflux, the solution was kept on a hotplate at 70 °C to evaporate the solvent. The wet gel was then completely dried in a vacuum oven. The resultant dried gel was first heat-treated in a tube furnace at 600 °C for 3 h flowing Ar gas. The product was ball-milled with ZrO_2 balls and ethanol, dried, and heat-treated again at the same condition.

Materials Characterization

X-ray diffraction (XRD) patterns of the powder samples were measured with a Bruker D8-Advance using $\text{Cu K}\alpha$ radiation. Field-emission scanning electron microscopy (FESEM) images were taken by a Hitachi SU-70. High-resolution transmission electron microscopy (HRTEM) analysis was conducted by a JEOL JEM-2100F. The Brunauer–Emmett–Teller (BET) specific surface area and pore size distribution of the products were examined by a nitrogen adsorption–desorption process at 77 K using a Micromeritics ASAP 2010. The Na, Co and P concentration dissolved in the solutions was determined using inductively coupled plasma-optical emission spectroscopy (ICP-OES; ICP-730

ES, Varian).

Electrochemical Measurements

The electrochemical properties of all $\text{Na}_{2-2x}\text{Co}_{1+x}\text{P}_2\text{O}_7$ samples were evaluated using coin-type (CR2032) half cells that were fabricated in an Ar-filled glove box. All working electrodes were prepared with 70 wt% active materials, 15 wt% Super P carbon black (MMM Carbon, Belgium), and 15 wt% PVDF binder (Sigma-Aldrich), and were cast onto Al foil. The average mass loading of the active materials on Al foil was 1 mg cm^{-2} . The cells were assembled with a working electrode, a separator film (glass microfiber), and Na-metal foil as the counter electrode saturated with a liquid electrolyte consisting of 0.8 M NaPF_6 dissolved in a solution of ethylene carbonate and diethyl carbonate (EC/DEC), at a volume ratio of 1:1. The fabricated cells were galvanostatically cycled using an automatic battery cycler (WBCS3000, WonATech, Korea). Co-based pyrophosphate electrodes were cycled at voltages ranging from 1.5 to 4.7 V (or charged to $100\text{-}120 \text{ mA h g}^{-1}$ and discharged to 1.5 V). Cyclic voltammetry (CV) measurements were obtained at voltages ranging from 3.0 to 5.0 V at a scan rate of 0.05 mV s^{-1} .

5.2 Triclinic Phase $\text{Na}_{2-2x}\text{Co}_{1+x}\text{P}_2\text{O}_7$

Prior to synthesize rose phase $\text{Na}_2\text{CoP}_2\text{O}_7/\text{C}$ nanocomposites ($\text{Na}_2\text{CoP}_2\text{O}_7$ -NPs/C), phase information of micro-sized bulk $\text{Na}_2\text{CoP}_2\text{O}_7$ (B- $\text{Na}_2\text{CoP}_2\text{O}_7$) synthesized by a conventional solid-state reaction method was investigated. Among three distinct phase in $\text{Na}_2\text{CoP}_2\text{O}_7$, it is known that blue or rose phase are synthesized by a solid-state reaction. Also, non-stoichiometric factor in $\text{Na}_2\text{CoP}_2\text{O}_7$ compound, *i.e.* $\text{Na}_{2-2x}\text{Co}_{1+x}\text{P}_2\text{O}_7$ (Co-excess and Na-deficiency for charge balance), can affect the formation of $\text{Na}_2\text{CoP}_2\text{O}_7$ polymorphs. Therefore, phase dependence of the $\text{Na}_{2-2x}\text{Co}_{1+x}\text{P}_2\text{O}_7$ ($x = 0, 0.1, 0.2$) as a function of elements (Co, Na), annealing temperature and holding time was investigated. All the $\text{Na}_{2-2x}\text{Co}_{1+x}\text{P}_2\text{O}_7$ were annealed in inert atmosphere flowing Ar gas. For the XRD reference data, well-known JCPDS data (blue phase; JCPDS No. 13-3868, rose phase; JCPDS No. 13-3867) were used.

5.2.1 Temperature Dependence

First, phase dependence of the $\text{Na}_{2-2x}\text{Co}_{1+x}\text{P}_2\text{O}_7$ on the annealing temperature fixing the holding time for 1 h was investigated. Figure 5.2.1 shows the XRD patterns of $\text{Na}_2\text{CoP}_2\text{O}_7$ at the annealing temperature ranging from 500 and 650 °C for 1h. According to the previous researches, [5.1-5.3] general synthesized form in stoichiometric compound is blue phase, while rose phase is hardly synthesized at ambient condition. However, it can be seen that rose

phase was identified when annealed under 500 °C for 1 h, although some secondary peaks related to blue phase were also detected. However, blue phase was obtained annealed above 500 °C. In other words, because rose phase is relatively unstable compared to blue phase, metastable rose phase can be synthesized at low annealing temperature in stoichiometric compound.

Figure 5.2.2 shows the XRD patterns of $\text{Na}_{1.8}\text{Co}_{1.1}\text{P}_2\text{O}_7$ at the annealing temperature ranging from 500 and 650 °C for 1h. Rose phase was identified when annealed at 500 °C for 1 h. In contrast to stoichiometric compound, secondary peaks related to blue phase were not detected in XRD pattern annealed at 500 °C for 1 h, although unidentified peak (*) at $2\theta = 14.3^\circ$ which is probably related to Co was also detected. However, annealed at 600 °C for 1 h, pure rose can be synthesized. With an increase of annealing temperature above 600 °C and below melting point, small amount of blue phase was obtained.

Figure 5.2.3 shows the XRD patterns $\text{Na}_{1.6}\text{Co}_{1.2}\text{P}_2\text{O}_7$ at the annealing temperature ranging from 500 and 680 °C for 1 h. Even though $\text{Na}_{1.6}\text{Co}_{1.2}\text{P}_2\text{O}_7$ was annealed above 600 °C for 1h, no blue peak was obtained. That is, all rose phases included unidentified peak (*) at $2\theta = 14.3^\circ$ in these annealing temperature ranges. Considering above XRD patterns in Figure 5.2.1, 5.2.2 and 5.2.3, phase diagram of $\text{Na}_{2-2x}\text{Co}_{1+x}\text{P}_2\text{O}_7$ synthesized by solid-state reaction when holding time is fixed in 1 h was tabulated in Table 5.2.1.

Table 5.2.1 Phase diagram of $\text{Na}_{2-2x}\text{Co}_{1+x}\text{P}_2\text{O}_7$ synthesized by solid-state reaction obtained from XRD patterns in Figure 5.2.1, 5.2.2 and 5.2.3 (holding time: 1 h).

$\text{Na}_{2-2x}\text{Co}_{1+x}\text{P}_2\text{O}_7$ (Holding time: 1 h)			
Temperature	$\text{Na}_2\text{CoP}_2\text{O}_7$	$\text{Na}_{1.8}\text{Co}_{1.1}\text{P}_2\text{O}_7$	$\text{Na}_{1.6}\text{Co}_{1.2}\text{P}_2\text{O}_7$
Over 650 °C	-	-	rose + impurity
650 °C	blue	rose (major) + blue (minor)	rose + impurity
600 °C	blue	rose	rose + impurity
550 °C	blue	rose + Impurity	rose + impurity
Below 650 °C	rose (major) + blue (minor)	rose + impurity	rose + impurity

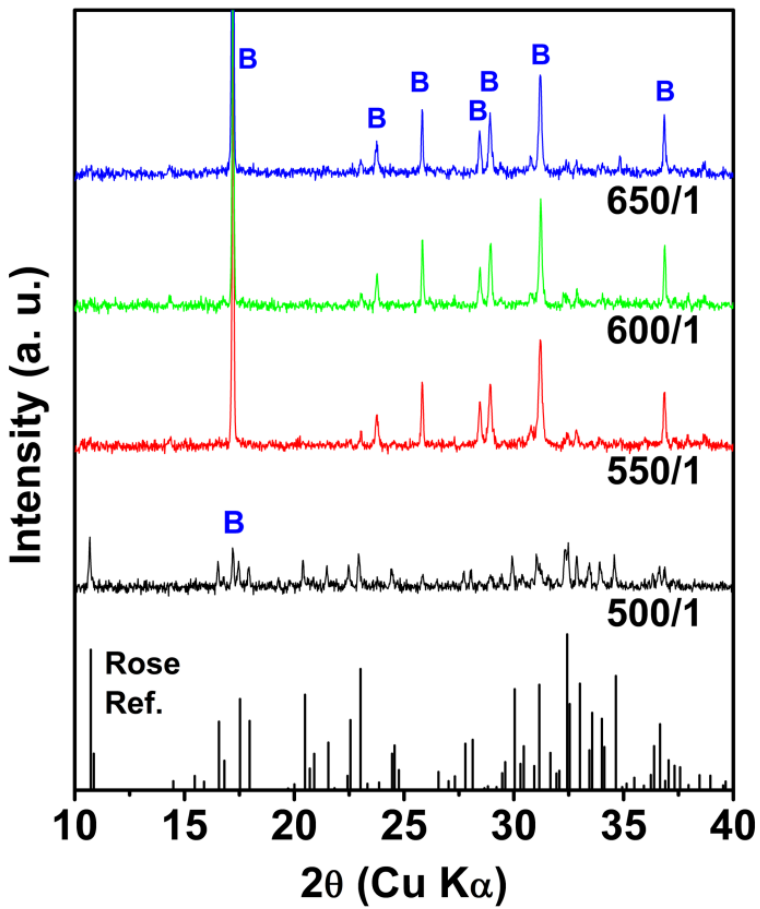


Figure 5.2.1 XRD patterns of $\text{Na}_2\text{CoP}_2\text{O}_7$ with various annealing temperature from 500 to 650 °C for 1 h.

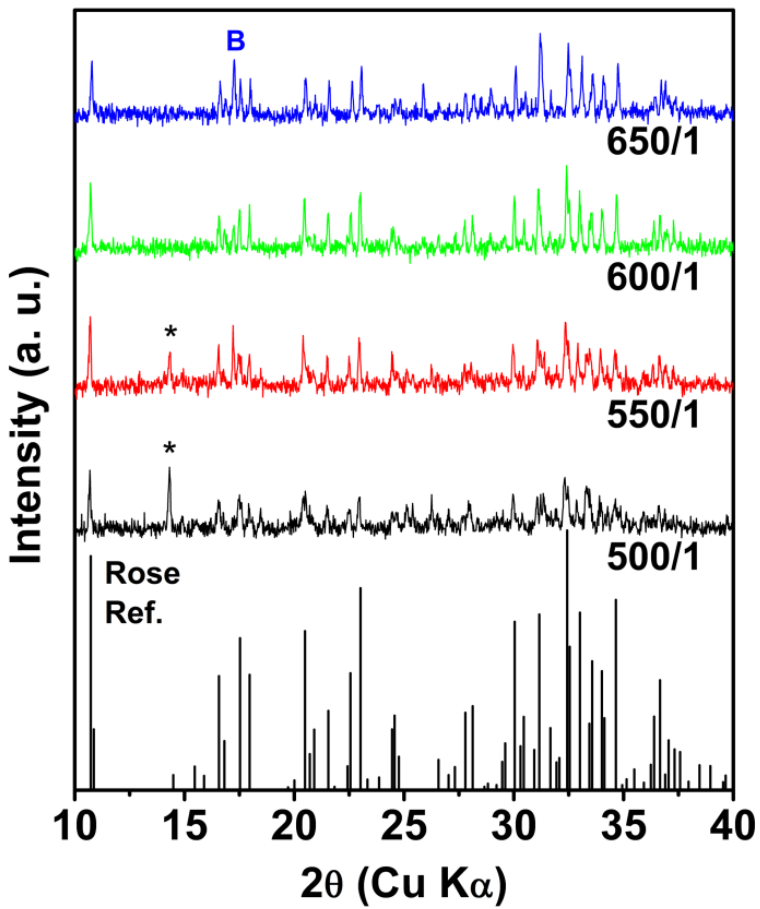


Figure 5.2.2 XRD patterns of $\text{Na}_{1.8}\text{Co}_{1.1}\text{P}_2\text{O}_7$ with various annealing temperature from 500 to 650 °C for 1 h.

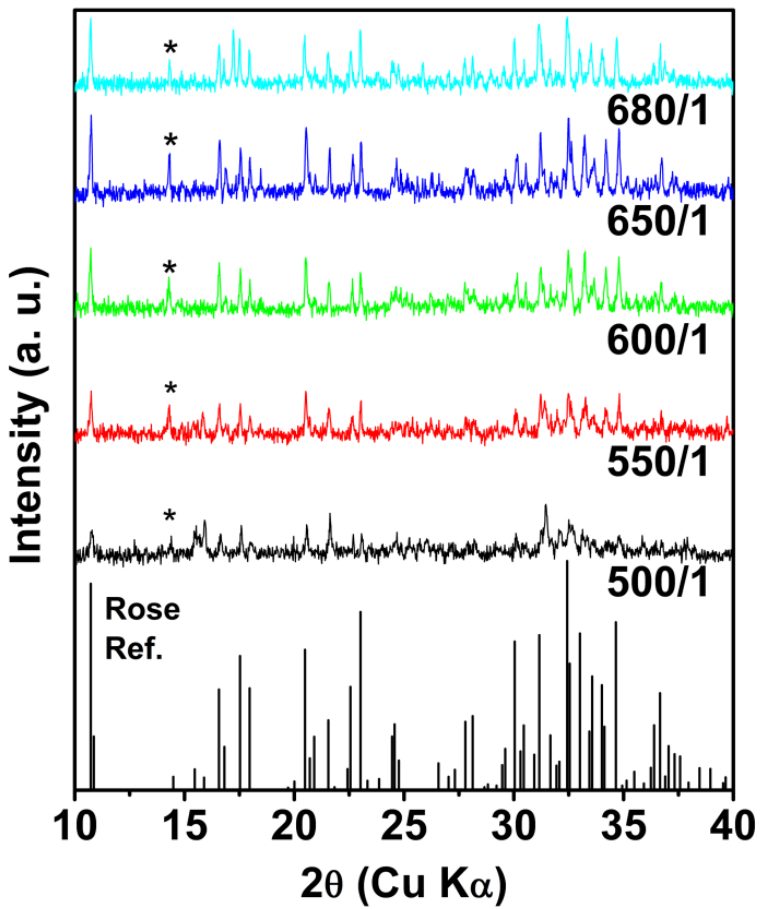


Figure 5.2.3 XRD patterns of $\text{Na}_{1.6}\text{Co}_{1.2}\text{P}_2\text{O}_7$ with various annealing temperature from 500 to 680 °C for 1 h.

5.2.2 Time Dependence

Phase dependence of the $\text{Na}_{1.8}\text{Co}_{1.1}\text{P}_2\text{O}_7$ and $\text{Na}_{1.6}\text{Co}_{1.2}\text{P}_2\text{O}_7$ on the holding times fixing the annealing temperature was investigated. First, $\text{Na}_{1.8}\text{Co}_{1.1}\text{P}_2\text{O}_7$ was synthesized at 600 °C with increasing holding times from 1 to 6 h. Figure 5.2.4 shows the XRD patterns of $\text{Na}_{1.8}\text{Co}_{1.1}\text{P}_2\text{O}_7$ annealed at 600 °C with increasing holding times from 1 to 6 h. Even though pure rose was synthesized annealed at 600 °C for 1 h, blue phase as well as rose phase were obtained in product when annealed for more than 2 h, meaning that metastable rose phase was transformed to stable blue phase as increasing the holding time. But, all the rose phase was transformed to blue phase.

Figure 5.2.5 shows the XRD patterns of $\text{Na}_{1.6}\text{Co}_{1.2}\text{P}_2\text{O}_7$ annealed at 650 and 680 °C with increasing holding times from 1 to 6 h. Unidentified peak at $2\theta = 14.3^\circ$ (*) which is probably related to Co was still detected in XRD pattern annealed at 650 °C for 6 h. However, pure rose without any secondary peak such as blue phase (B) and unidentified phase (*) can be synthesized annealed at 680 °C for 6 h. Interestingly, in non-stoichiometric $\text{Na}_{1.6}\text{Co}_{1.2}\text{P}_2\text{O}_7$ compound, blue phase was not obtained even annealed at high temperature for a longer holding time. Considering above XRD patterns in Figure 5.2.4, and 5.2.5, phase diagram of $\text{Na}_{2-2x}\text{Co}_{1+x}\text{P}_2\text{O}_7$ synthesized by solid-state reaction when holding time is fixed in 6 h was tabulated in Table 5.2.2.

In sum, considering above XRD patterns in chapter 5.2.1 and 5.2.2, phase dependence of the $\text{Na}_{2-2x}\text{Co}_{1+x}\text{P}_2\text{O}_7$ on the annealing temperature and holding time is as follows;

- i) In contrast to previous research, rose phase can be synthesized in stoichiometric $\text{Na}_2\text{CoP}_2\text{O}_7$ compound. In order to obtain rose phase, it has to be annealed at low temperature under 500 °C. However, pure rose was not obtained.
- ii) With the increasing of Co element and decreasing of Na element for charge balance in non-stoichiometric $\text{Na}_{2-2x}\text{Co}_{1+x}\text{P}_2\text{O}_7$ compounds, metastable rose phase can be obtained stably at higher annealing temperature over 500 °C compared to stoichiometric compound.
- iii) Pure rose can be obtained in $\text{Na}_{1.8}\text{Co}_{1.1}\text{P}_2\text{O}_7$ annealed at 600 °C for 1 h. But, blue phase becomes to appear as increasing annealing temperature or holding time.
- iv) As the x is increased to 1.2 ($\text{Na}_{1.6}\text{Co}_{1.2}\text{P}_2\text{O}_7$), blue phase is not synthesized and rose phase is always obtained annealed under melting point. Also, pure rose $\text{Na}_{1.6}\text{Co}_{1.2}\text{P}_2\text{O}_7$ can be obtained annealed at higher temperature for a longer holding time.

Meanwhile, the atomic ratios of Na/Co/P in $\text{Na}_2\text{CoP}_2\text{O}_7$, $\text{Na}_{1.8}\text{Co}_{1.1}\text{P}_2\text{O}_7$ and $\text{Na}_{1.6}\text{Co}_{1.2}\text{P}_2\text{O}_7$ synthesized at 500 °C for 1 h, 600 °C for 1 h and 680 °C for

6 h, respectively, were measured and their values were tabulated in Table 5.2.3.

Shown in table 5.2.3, each elemental ratio is 2.01:0.99:2, 1.82:1.11:2 and 1.64:1.20:2, respectively, by ICP-OES. From these results, the elemental ratio in all products almost coincides with the elemental ratio in starting materials mixture before annealing.

Table 5.2.2 Phase diagram of $\text{Na}_{2-2x}\text{Co}_{1+x}\text{P}_2\text{O}_7$ synthesized by solid-state reaction obtained from XRD patterns in Figure 5.2.4 and 5.2.5 (holding time: 6 h).

$\text{Na}_{2-2x}\text{Co}_{1+x}\text{P}_2\text{O}_7$ (Holding time: 6 h)			
Temperature	$\text{Na}_2\text{CoP}_2\text{O}_7$	$\text{Na}_{1.8}\text{Co}_{1.1}\text{P}_2\text{O}_7$	$\text{Na}_{1.6}\text{Co}_{1.2}\text{P}_2\text{O}_7$
680 °C	-		rose
			rose
650 °C	-	-	+ impurity
600 °C		rose (major) + blue (minor)	-

Table 5.2.3 Atomic ratio of Na, Co and P in each $\text{Na}_2\text{CoP}_2\text{O}_7$, $\text{Na}_{1.8}\text{Co}_{1.1}\text{P}_2\text{O}_7$ and $\text{Na}_{1.6}\text{Co}_{1.2}\text{P}_2\text{O}_7$ synthesized at 500 °C for 1 h, 600 °C for 1 h and 680 °C for 6 h, respectively by ICP analysis.

Sample	Element	# of Moles	Atomic Ratio
$\text{Na}_2\text{CoP}_2\text{O}_7$	Na	1.547	2.01
	Co	0.767	0.99
	P	1.543	2.00
$\text{Na}_{1.8}\text{Co}_{1.1}\text{P}_2\text{O}_7$	Na	0.987	1.82
	Co	0.604	1.11
	P	1.087	2.00
$\text{Na}_{1.6}\text{Co}_{1.2}\text{P}_2\text{O}_7$	Na	1.294	1.64
	Co	0.941	1.20
	P	1.574	2.00

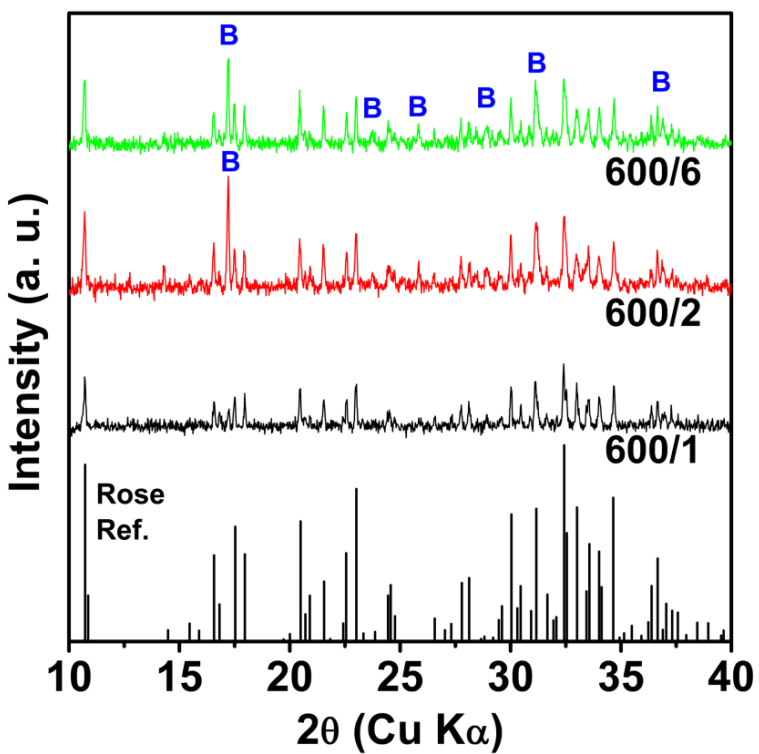


Figure 5.2.4 XRD patterns of $\text{Na}_{1.8}\text{Co}_{1.1}\text{P}_2\text{O}_7$ annealed at $600\text{ }^{\circ}\text{C}$ with increasing holding times from 1 to 6 h.

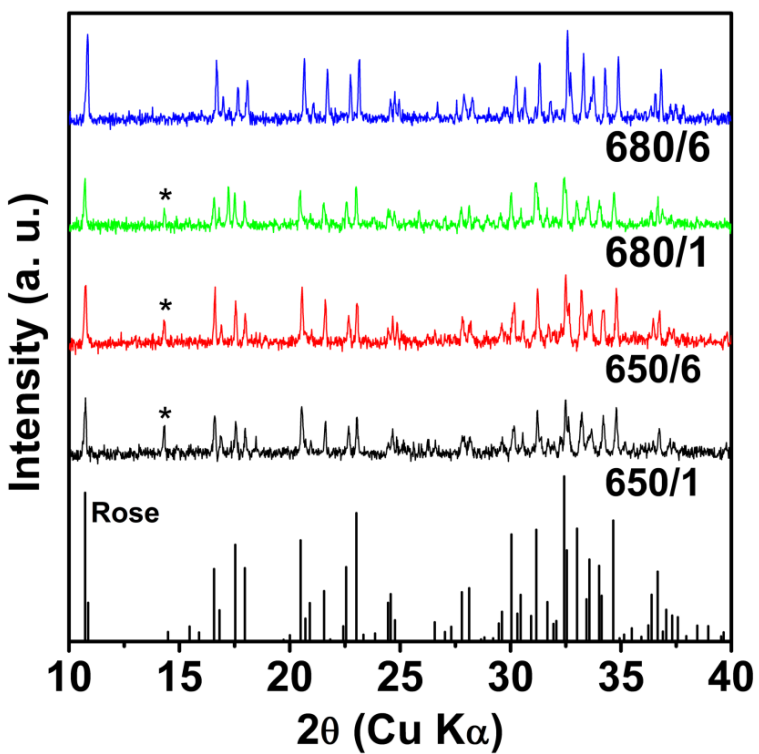


Figure 5.2.5 XRD patterns of $\text{Na}_{1.6}\text{Co}_{1.2}\text{P}_2\text{O}_7$ annealed at 650 and 680 °C with increasing holding times from 1 to 6 h.

5.3 $\text{Na}_{2-2x}\text{Co}_{1+x}\text{P}_2\text{O}_7/\text{C}$ Nanocomposites

5.3.1 Synthesis of $\text{Na}_{2-2x}\text{Co}_{1+x}\text{P}_2\text{O}_7/\text{C}$ Nanocomposites

Using the same synthetic process with Fe-based pyrophosphate nanocomposites in chapter 4 (gelation \rightarrow HT \rightarrow BM \rightarrow HT process), $\text{Na}_{2-2x}\text{Co}_{1+x}\text{P}_2\text{O}_7/\text{C}$ nanocomposites ($\text{Na}_{2-2x}\text{Co}_{1+x}\text{P}_2\text{O}_7\text{-NPs/C}$) were also synthesized in this chapter.

Figure 5.3.1a shows the XRD patterns of $\text{Na}_2\text{CoP}_2\text{O}_7\text{-NPs/C}$ heat-treated at 600 °C for 1 h. In the case of synthesizing B- $\text{Na}_2\text{CoP}_2\text{O}_7$, pure blue phase was obtained when heat-treated at 600 °C for 1 h. While, pure rose without any blue phase was synthesized in $\text{Na}_2\text{CoP}_2\text{O}_7\text{-NPs/C}$ after HT and HT \rightarrow BM \rightarrow HT process. However, with increasing holding time from 1 to 3 h, some blue phase was obtained in $\text{Na}_2\text{CoP}_2\text{O}_7\text{-NPs/C}$ after HT \rightarrow BM \rightarrow HT process (Figure 5.3.1b).

Figure 5.3.2 shows the XRD patterns of $\text{Na}_{1.8}\text{Co}_{1.1}\text{P}_2\text{O}_7\text{-NPs/C}$ with various annealing condition. Similar to B- $\text{Na}_{1.8}\text{Co}_{1.1}\text{P}_2\text{O}_7$ and $\text{Na}_2\text{CoP}_2\text{O}_7\text{-NPs/C}$, pure rose was synthesized in $\text{Na}_{1.8}\text{Co}_{1.1}\text{P}_2\text{O}_7\text{-NPs/C}$ after HT process (HT condition: 600 °C for 1 h) and HT \rightarrow BM \rightarrow HT process (Figure 5.3.2a). Interestingly, whether increasing the holding time of 3 and 6 h or increasing heat treatment temperature, pure rose without any blue phase was synthesized in all case (Figure 5.3.2b-d). In order words, both $\text{Na}_2\text{CoP}_2\text{O}_7\text{-NPs/C}$ and $\text{Na}_{1.8}\text{Co}_{1.1}\text{P}_2\text{O}_7\text{-NPs/C}$ synthesized by a sol-gel method exhibited more phase

stability in metastable rose phase than B-Na₂CoP₂O₇ and B-Na_{1.8}Co_{1.1}P₂O₇ synthesized by a solid-state reaction at higher heat-treating temperature and for a longer holding time.

This phenomenon that the stable phase is dependent on the particle size in nanoscale can be found other materials. In the case of macroscale TiO₂, rutile polymorph is the most thermodynamically stable phase in TiO₂ at ambient pressures and temperatures, however, anatase polymorph can be a majority product in nanoscale TiO₂ synthesized by a wet-chemical synthetic method. [5.4-5.6] Not only TiO₂, but also other inorganic nano-materials, *i.e.* VO₂, ZrO₂ and CdSe, show this phenomenon. [5.7-5.9] Indeed, B-Na₂CoP₂O₇ synthesized by a solid-state reaction has a micro-sized particles (Figure 5.3.3), while Na₂CoP₂O₇-NPs has a tens of sized nanoparticles below 50 nm (Figure 5.1.5c-d). Considering both FESEM images of B-Na₂CoP₂O₇, Na₂CoP₂O₇-NPs/C and XRD patterns of B-Na₂CoP₂O₇ (Figure 5.2.1), Na₂CoP₂O₇-NPs/C (Figure 5.3.1), it can be said that particle size has an influence on the stable phase form in Na₂CoP₂O₇.

Figure 5.3.4 shows the XRD pattern of Na_{1.6}Co_{1.2}P₂O₇-NPs/C. Similar to Na_{1.8}Co_{1.1}P₂O₇-NPs/C, rose phase was synthesized regardless of holding time heat-treated at 600 °C. Also, no unidentified peak (*) at $2\theta = 14.3^\circ$ was detected in XRD patterns in contrast to B-Na_{1.6}Co_{1.2}P₂O₇. Considering above XRD patterns in Figure 5.3.1, 5.3.2 and 5.3.4, phase diagram of Na_{2-2x}Co_{1+x}P₂O₇-NPs/C synthesized by sol-gel method was tabulated in Table 5.3.1.

In sum, considering above XRD patterns and particle size in FESEM images, phase dependence of the $\text{Na}_{2-2x}\text{Co}_{1+x}\text{P}_2\text{O}_7$ on the heat-treating temperature and holding time is as follows;

- i) Pure metastable rose becomes to major products both stoichiometric and non-stoichiometric $\text{Na}_{2-2x}\text{Co}_{1+x}\text{P}_2\text{O}_7/\text{C}$ nanocomposites ($0 \leq x \leq 0.2$) synthesized by a sol-gel method and then heat-treated at 600°C for 1 h.
- ii) In stoichiometric $\text{Na}_2\text{CoP}_2\text{O}_7$ -NPs/C compound, partial rose phase is transformed to blue phase after $\text{HT} \rightarrow \text{BM} \rightarrow \text{HT}$ process for a longer holding time (HT condition: 600°C for 3 h).
- iii) In non-stoichiometric compounds, pure rose without any secondary peaks related to blue phase (B) or unidentified phase (*) can be obtained even under various heat treatment conditions.

Figure 3.2.5c-d and Figure 5.3.5 show the FESEM images of $\text{Na}_{2-x}\text{Co}_{1+x}\text{P}_2\text{O}_7$ -NPs/C. Similar to Fe-based pyrophosphate nanocomposites, less-agglomerated and uniform-sized $\text{Na}_{2-2x}\text{Co}_{1+x}\text{P}_2\text{O}_7$ -NPs/C was synthesized after $\text{HT} \rightarrow \text{BM} \rightarrow \text{HT}$ process. Also, they share similar particle size of 50 nm, meaning that particle size did not affect the ratio of Co and Na element in synthetic process.

Meanwhile, the atomic ratio of Na/Co/P in $\text{Na}_2\text{CoP}_2\text{O}_7$ -NPs/C, $\text{Na}_{1.8}\text{Co}_{1.1}\text{P}_2\text{O}_7$ -NPs/C and $\text{Na}_{1.6}\text{Co}_{1.2}\text{P}_2\text{O}_7$ -NPs/C synthesized at 600°C for 1 h,

600 °C for 3 h and 600 °C for 3 h, respectively, were measured and their values were tabulated in Table 5.3.2. Shown in table 5.3.2, each elemental ratio is 2.02:1.03:2, 1.82:1.12:2 and 1.65:1.23:2, respectively, by ICP-OES. From these results, the elemental ratio in all products almost coincides with the elemental ratio in starting materials mixture before heat treatment.

Table 5.3.1 Phase diagram of $\text{Na}_{2-2x}\text{Co}_{1+x}\text{P}_2\text{O}_7$ -NPs/C synthesized by sol-gel method obtained from XRD patterns in Figure 5.3.1, 5.3.2 and 5.3.4.

$\text{Na}_{2-2x}\text{Co}_{1+x}\text{P}_2\text{O}_7$ (Annealing temperature: 600 °C)			
Time	$\text{Na}_2\text{CoP}_2\text{O}_7$	$\text{Na}_{1.8}\text{Co}_{1.1}\text{P}_2\text{O}_7$	$\text{Na}_{1.6}\text{Co}_{1.2}\text{P}_2\text{O}_7$
1 + 1 h	rose → rose	rose → rose	rose → rose
3 + 3 h	rose → rose + blue	rose → rose	rose → rose

Table 5.3.2 Atomic ratio of Na, Co and P in each $\text{Na}_2\text{CoP}_2\text{O}_7$ -NPs/C, $\text{Na}_{1.8}\text{Co}_{1.1}\text{P}_2\text{O}_7$ -NPs/C and $\text{Na}_{1.6}\text{Co}_{1.2}\text{P}_2\text{O}_7$ -NPs/C synthesized at 600 °C for 1 h, 600 °C for 3 h and 600 °C for 3 h, respectively, by ICP analysis.

Sample	Element	# of Moles	Atomic Ratio
$\text{Na}_2\text{CoP}_2\text{O}_7$ -NPs/C	Na	1.144	2.02
	Co	0.583	1.03
	P	1.134	2.00
$\text{Na}_{1.8}\text{Co}_{1.1}\text{P}_2\text{O}_7$ -NPs/C	Na	4.157	1.82
	Co	0.712	1.12
	P	1.268	2.00
$\text{Na}_{1.6}\text{Co}_{1.2}\text{P}_2\text{O}_7$ -NPs/C	Na	0.929	1.65
	Co	0.689	1.23
	P	1.122	2.00

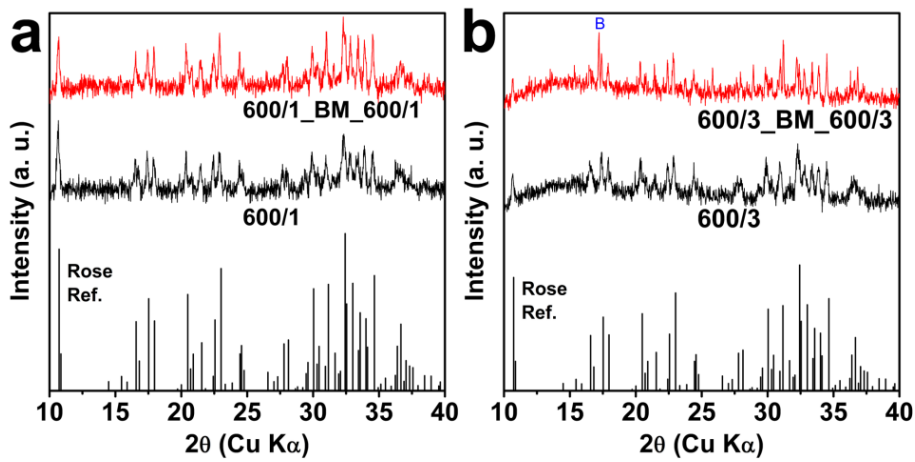


Figure 5.3.1 XRD patterns of $\text{Na}_2\text{CoP}_2\text{O}_7$ -NPs/C. HT condition of (a) 600 $^{\circ}\text{C}$ for 1 h and (b) 600 $^{\circ}\text{C}$ for 3 h.

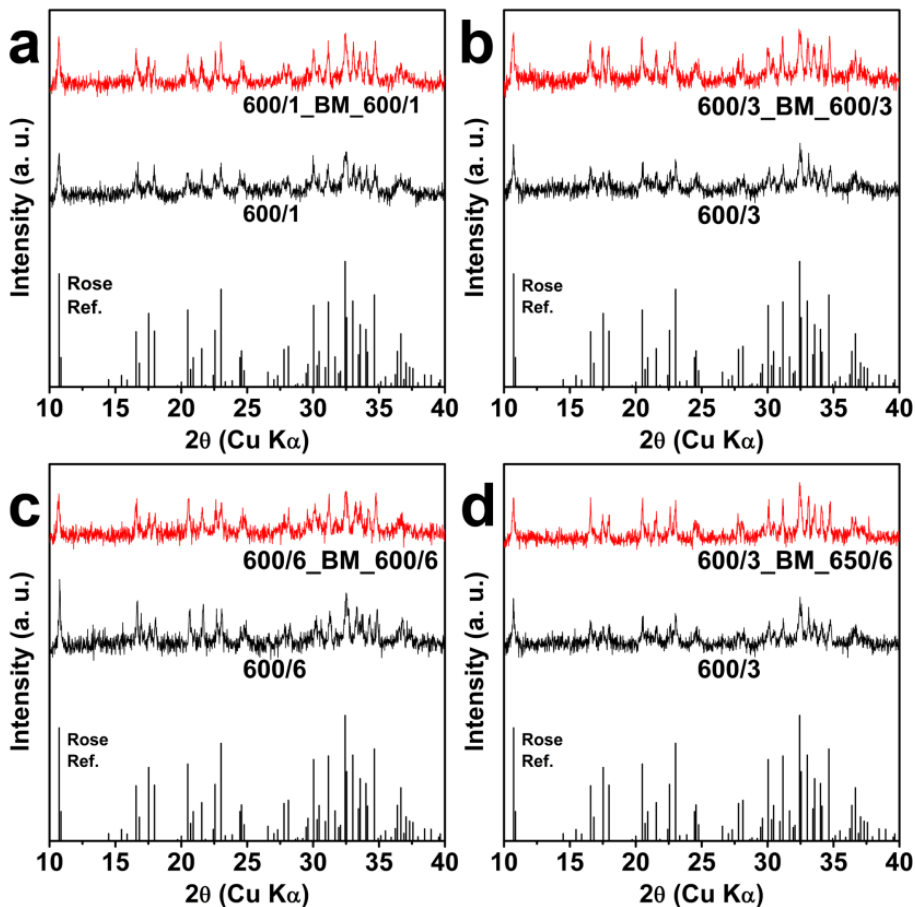


Figure 5.3.2 XRD patterns of $\text{Na}_{1.8}\text{Co}_{1.1}\text{P}_2\text{O}_7$ -NPs/C. HT condition of (a) 600 °C for 1 h, (b) 600 °C for 3 h, (c) 600 °C for 6 h, and (d) 600-650 °C for 3-6 h.

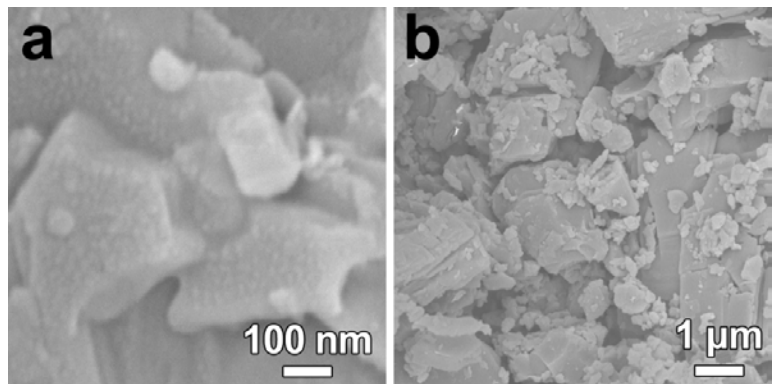


Figure 5.3.3 (a) High- and (b) low-magnification FESEM images of B- $\text{Na}_2\text{CoP}_2\text{O}_7$ synthesized by a solid-state reaction.

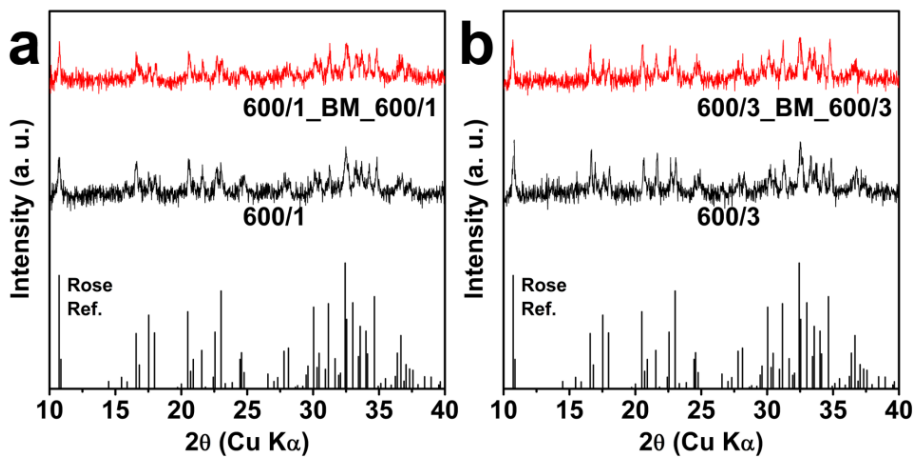


Figure 5.3.4 XRD patterns of $\text{Na}_{1.6}\text{Co}_{1.2}\text{P}_2\text{O}_7$ -NPs/C. HT condition of (a) $600\text{ }^{\circ}\text{C}$ for 1 h and (b) $600\text{ }^{\circ}\text{C}$ for 3 h.

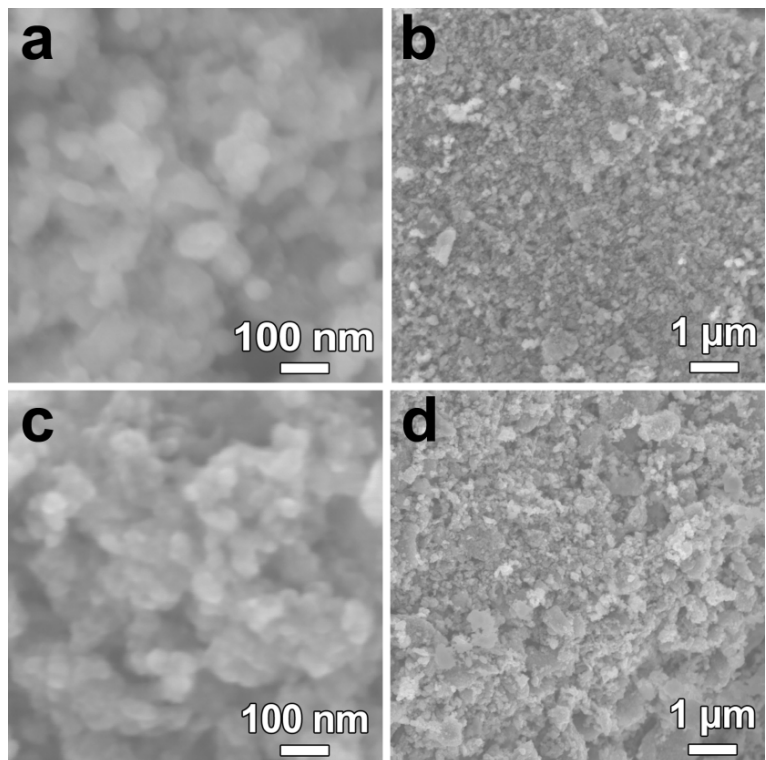


Figure 5.3.5 High- and low-magnification FESEM images of (a-b) $\text{Na}_{1.8}\text{Co}_{1.1}\text{P}_2\text{O}_7\text{-NPs/C}$ and (c-d) $\text{Na}_{1.6}\text{Co}_{1.2}\text{P}_2\text{O}_7\text{-NPs/C}$.

5.3.2 $\text{Na}_{2-2x}\text{Co}_{1+x}\text{P}_2\text{O}_7/\text{C}$ Nanocomposites for Na-Ion Batteries

B- $\text{Na}_{1.8}\text{Co}_{1.1}\text{P}_2\text{O}_7/\text{C}$ for NIBs

Prior to evaluate the electrochemical performance of $\text{Na}_{2-2x}\text{Co}_{1+x}\text{P}_2\text{O}_7$ -NPs/C, electrochemical performance of rose phase B- $\text{Na}_{1.8}\text{Co}_{1.1}\text{P}_2\text{O}_7/\text{C}$ was investigated. Because pure rose $\text{Na}_2\text{CoP}_2\text{O}_7$ cannot be synthesized, while $\text{Na}_{1.8}\text{Co}_{1.1}\text{P}_2\text{O}_7$ can be, rose phase B- $\text{Na}_{1.8}\text{Co}_{1.1}\text{P}_2\text{O}_7$ was selected. Pure rose B- $\text{Na}_{1.8}\text{Co}_{1.1}\text{P}_2\text{O}_7$ without carbon can be synthesized annealed at 600 °C for 1 h (Figure 5.2.2). However, pure rose B- $\text{Na}_{1.8}\text{Co}_{1.1}\text{P}_2\text{O}_7/\text{C}$ cannot be obtained when synthesized by 1-step; starting materials were mixed with glucose and annealed at 600 °C for 1 h (Figure 5.3.6). So, Rose phase B- $\text{Na}_{1.8}\text{Co}_{1.1}\text{P}_2\text{O}_7/\text{C}$ was synthesized at first, and then mixed with graphite for carbon coating. The ratio of B- $\text{Na}_{1.8}\text{Co}_{1.1}\text{P}_2\text{O}_7$ and graphite was 7:3 in wt%. In this case, pure rose B- $\text{Na}_{1.8}\text{Co}_{1.1}\text{P}_2\text{O}_7/\text{C}$ can be obtained (Figure 5.3.6).

Figure 5.3.7 show the galvanostatic charging/discharging profiles of B- $\text{Na}_{1.8}\text{Co}_{1.1}\text{P}_2\text{O}_7/\text{C}$ at 0.2 C (1 C = 96 mA g⁻¹) up to 30th cycle, over the voltage range of 1.5–4.7 V (vs. Na/Na⁺). It can be seen that B- $\text{Na}_{1.8}\text{Co}_{1.1}\text{P}_2\text{O}_7/\text{C}$ was electrochemically reacted with Na-ions in this voltage range. But discharge capacity reacted at high voltage over 4.0 V was measured to be low, indicative of few amount of Na-ions insertion in $\text{Na}_{1.8}\text{Co}_{1.1}\text{P}_2\text{O}_7$. Also, considering its theoretical capacity (96 mA h g⁻¹), lower discharge capacity of 40-50 mA h g⁻¹ was measured, probably owing to the large particle size of B- $\text{Na}_{1.8}\text{Co}_{1.1}\text{P}_2\text{O}_7$ or

non-homogeneous graphite coating on the surface of B-Na_{1.8}Co_{1.1}P₂O₇, which brought out low electrochemical reaction.

Na_{2-2x}Co_{1+x}P₂O₇/C Nanocomposites for NIBs

Cyclic voltammetry

The electrochemical properties of the Na₂CoP₂O₇-NPs/C, Na_{1.8}Co_{1.1}P₂O₇-NPs/C and Na_{1.6}Co_{1.2}P₂O₇-NPs/C electrodes were evaluated for the NIB cathode. Figure 5.3.8 shows the cyclic voltammograms of Na₂CoP₂O₇-NPs/C, Na_{1.8}Co_{1.1}P₂O₇-NPs/C and Na_{1.6}Co_{1.2}P₂O₇-NPs/C for initial 3 cycles measured at a scan rate of 0.05 mV s⁻¹ in voltage range of 3.0-5.0 V (vs. Na/Na⁺) to identify the electrochemical reactions. It can be seen that clear redox peaks between 3.9 and 4.7 V were observed in all three Na_{2-2x}Co_{1+x}P₂O₇-NPs/C which are consistent with previous study. [5.3]

Figure 5.3.9 shows the comparison of cyclic voltammetry at 5th cycle measured at a scan rate of 0.05 mV s⁻¹ in voltage range of 3.0-4.65 V (vs. Na/Na⁺). Redox peak intensity near 3.9 V were decreased as x in Na₂₋_{2x}Co_{1+x}P₂O₇-NPs/C was increased. Considering previous researches, [5.3,5.10] redox peak near 3.9 V is associated with the 1D channel of Na-ions. Excess amount of Co element as increase of x in Na_{2-2x}Co_{1+x}P₂O₇-NPs/C occupied the Na sites where Na-ions are intercalated/deintercalated. This Co defect in Na site interfered in Na-ion migration resulting in decrease of electrochemical reaction near 3.9 V. Also, Na₂CoP₂O₇-NPs/C and Na_{1.8}Co_{1.1}P₂O₇-NPs/C

exhibited the same redox peak between 4.3 and 4.6 V, while redox peaks of $\text{Na}_{1.6}\text{Co}_{1.2}\text{P}_2\text{O}_7$ -NPs/C were shifted to lower voltage, indicating that $\text{Na}_{1.6}\text{Co}_{1.2}\text{P}_2\text{O}_7$ -NPs/C has a different electrochemical reaction mechanism with $\text{Na}_2\text{CoP}_2\text{O}_7$ -NPs/C and $\text{Na}_{1.8}\text{Co}_{1.1}\text{P}_2\text{O}_7$ -NPs/C.

Cyclic performance

Figure 5.3.10 shows the galvanostatic charging/discharging profiles of $\text{Na}_2\text{CoP}_2\text{O}_7$ -NPs/C at 0.2 C (1 C = 96 mA g⁻¹) up to 30th cycle, charged to 100 mA h g⁻¹ and discharged to 1.5 V. 1st discharge capacities were measured to be 60 mA h g⁻¹, however capacity was increased up to 75 mA h g⁻¹ as more cycling was performed. It is considered that activation processes such as size, good dispersion, or compact contact between active materials and supports could improve the specific capacity of NCP-NPs/C after cycling.

Figure 5.3.11 shows the galvanostatic profiles of $\text{Na}_{1.8}\text{Co}_{1.1}\text{P}_2\text{O}_7$ -NPs/C for the same measurement condition with $\text{Na}_2\text{CoP}_2\text{O}_7$ -NPs/C. compared to B- $\text{Na}_{1.8}\text{Co}_{1.1}\text{P}_2\text{O}_7$ /C, discharge capacity reacted at high voltage over 5.0 V was measured to be higher. Also compared to $\text{Na}_2\text{CoP}_2\text{O}_7$ -NPs/C, discharge capacity was increased to 80 mA h g⁻¹ at 30th cycle due to more possible $\text{Co}^{2+}/\text{Co}^{3+}$ redox reaction in $\text{Na}_{1.8}\text{Co}_{1.1}\text{P}_2\text{O}_7$ -NPs/C. However, discharge capacity was not always increased at x in $\text{Na}_{2-2x}\text{Co}_{1+x}\text{P}_2\text{O}_7$ -NPs/C was increased. Shown in Figure 5.3.12, discharge capacity of $\text{Na}_{1.6}\text{Co}_{1.2}\text{P}_2\text{O}_7$ -NPs/C at 30th

cycle was measured to be lower than $\text{Na}_{1.8}\text{Co}_{1.1}\text{P}_2\text{O}_7$ -NPs/C, due to the Co in Na sites acting as a defect.

Figure 5.3.13 shows the galvanostatic charging/discharging profiles of $\text{Na}_{1.8}\text{Co}_{1.1}\text{P}_2\text{O}_7$ -NPs/C at 0.2 C (1 C = 96 mA g⁻¹) up to 30th cycle, charged to 120 mA h g⁻¹ and discharged to 1.5 V. Also, comparison of 10th and 20th voltage discharge capacity profiles are presented in Figure 5.3.14. As more Na-ions were charged in $\text{Na}_{1.8}\text{Co}_{1.1}\text{P}_2\text{O}_7$ -NPs/C, discharge capacity was measured to 90 mA h g⁻¹ at 30th cycle. It can be seen that discharge capacity reacted at high voltage over 4.0 V was increased at 10th discharge when charged to 120 mA h g⁻¹ (Figure 5.3.14a). It seemed that insufficient Na-ions were deintercalated from $\text{Na}_{1.8}\text{Co}_{1.1}\text{P}_2\text{O}_7$ -NPs/C in Figure 5.3.11. However, considering the theoretical capacity of $\text{Na}_2\text{CoP}_2\text{O}_7$ (96 mA h g⁻¹) and assuming that only $\text{Co}^{2+}/\text{Co}^{3+}$ redox reaction, not including $\text{Co}^{3+}/\text{Co}^{4+}$ redox reaction occurs in $\text{Na}_2\text{CoP}_2\text{O}_7$ electrode, more than 100 mA h g⁻¹ in galvanostatic charge capacity after several cycles is contradictory. Also, the low coulombic efficiency observed in all galvanostatic voltage profiles of $\text{Na}_{2-2x}\text{Co}_{1+x}\text{P}_2\text{O}_7$ (Figure 5.3.7, 5.3.10, 5.3.11, 5.3.12, 5.3.13). From these results, electrolyte decomposition would occur during the charge process. This electrolyte decomposition occurred more easily when charged to 120 mA h g⁻¹, which had an influence on more fast voltage profiles degradation (Figure 5.2.14b). At 20th cycle, these high operating voltage over 4.0 V (vs. Na/Na⁺) is as much as, or more than upper limit of the stable window of currently used NIB electrolytes. [5.3] The

solution of this electrolyte decomposition problem at high voltage will bring out the improvement of electrochemical performance. Therefore, development of suitable high-voltage electrolyte is also accompanied for the practical use of this $\text{Na}_{2-2x}\text{Co}_{1+x}\text{P}_2\text{O}_7$ material.

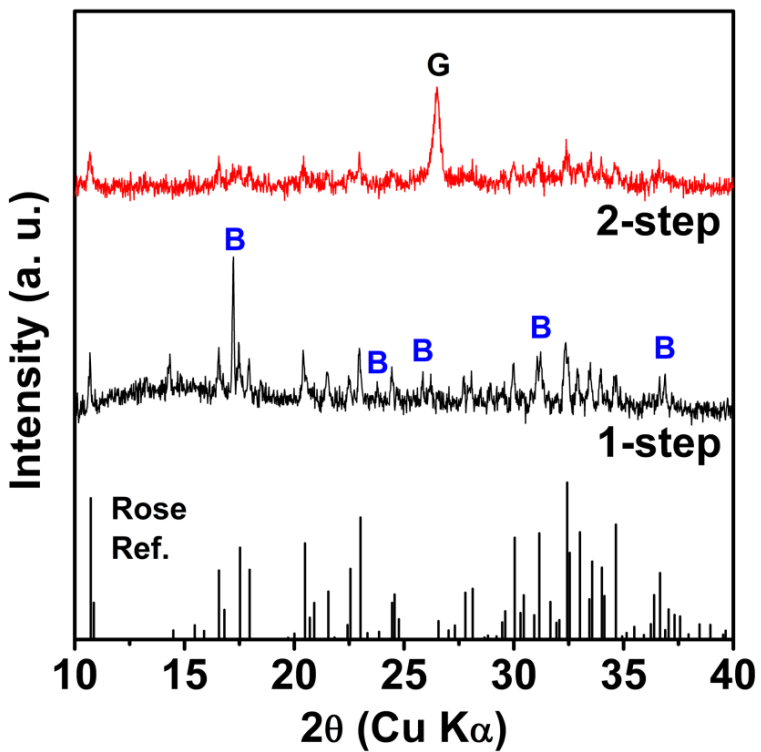


Figure 5.3.6 XRD pattern of B- $\text{Na}_{1.8}\text{Co}_{1.1}\text{P}_2\text{O}_7/\text{C}$ synthesized by (a) 1-step solid-state reaction with glucose as a carbon source, and (b) 2-step solid-state reaction with graphite as a carbon source.

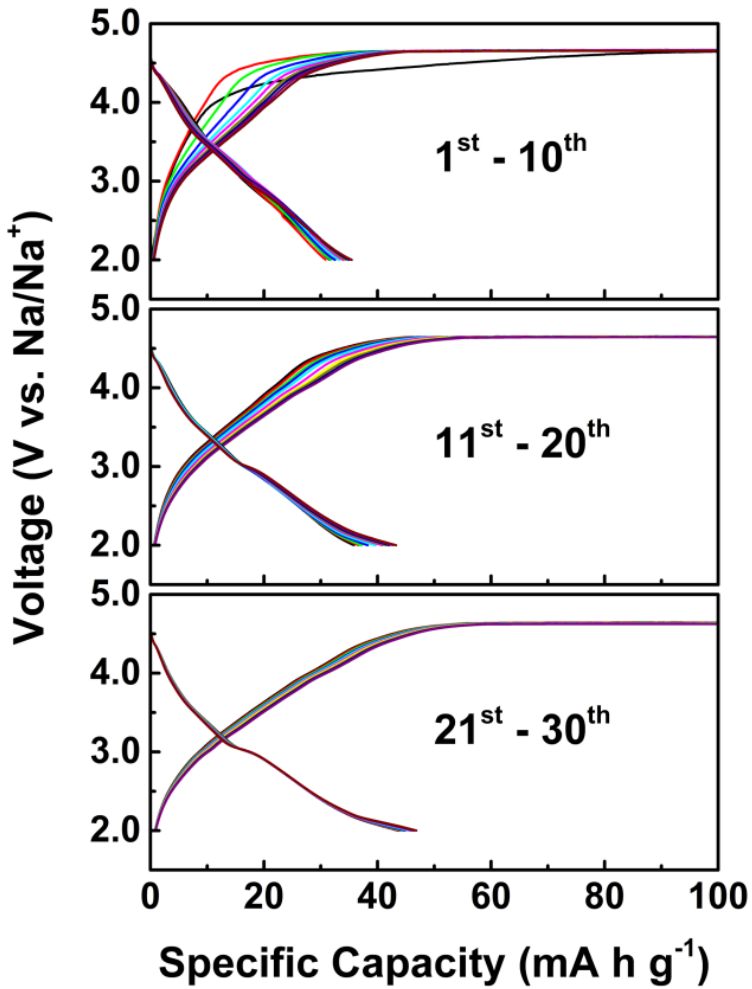


Figure 5.3.7 Galvanostatic voltage profiles of B-Na_{1.8}Co_{1.1}P₂O₇/C at 0.2 C.

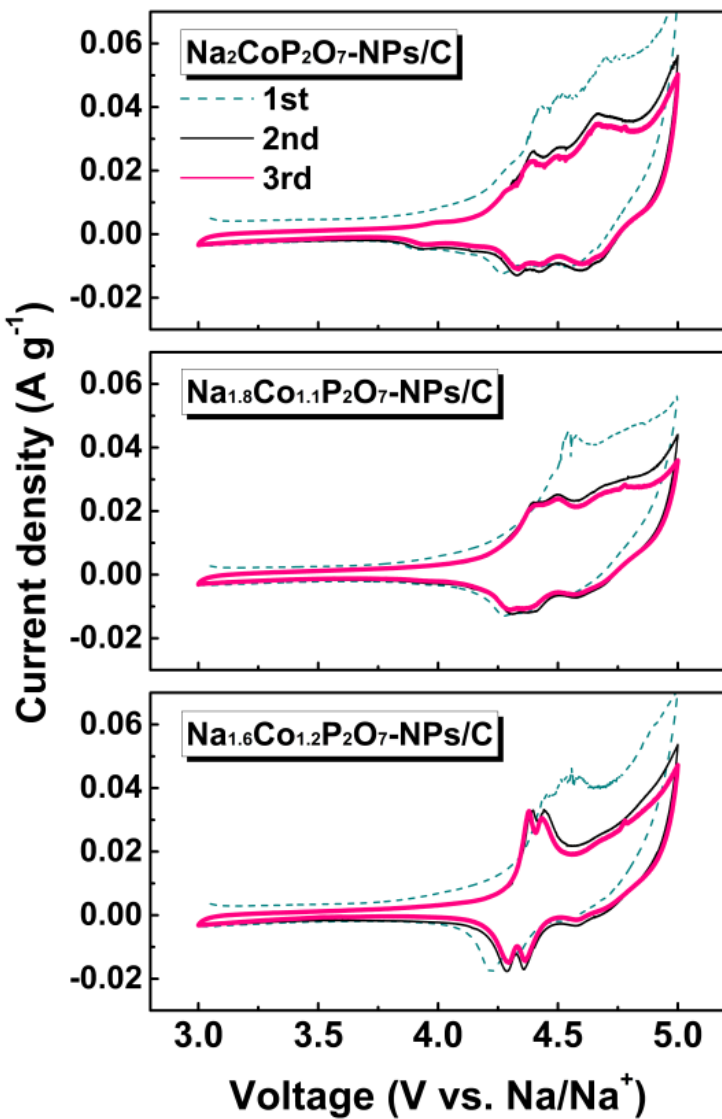
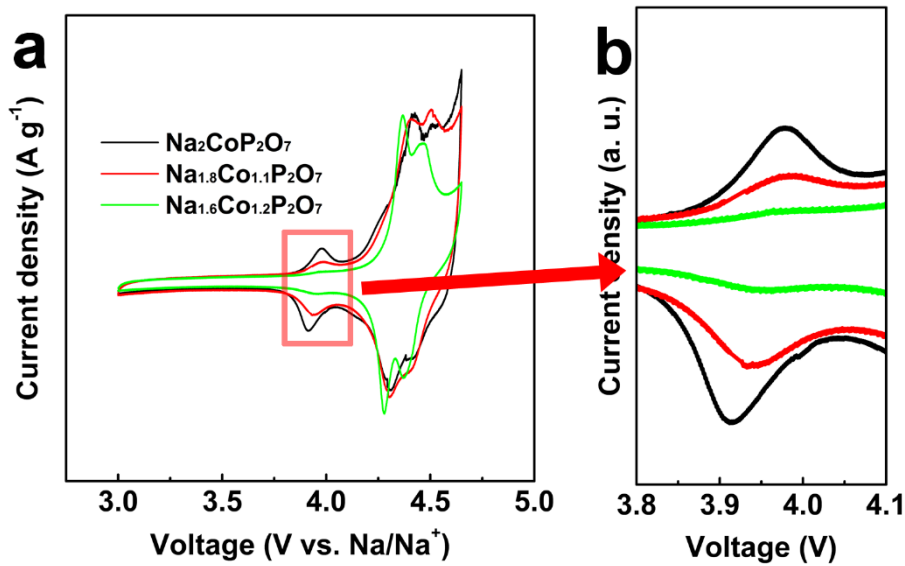


Figure 5.3.8 Cyclic voltammetry of (a) $\text{Na}_2\text{CoP}_2\text{O}_7\text{-NPs/C}$, (b) $\text{Na}_{1.8}\text{Co}_{1.1}\text{P}_2\text{O}_7\text{-NPs/C}$ and (c) $\text{Na}_{1.6}\text{Co}_{1.2}\text{P}_2\text{O}_7\text{-NPs/C}$ at a scan rate of 0.05 mV s^{-1} .



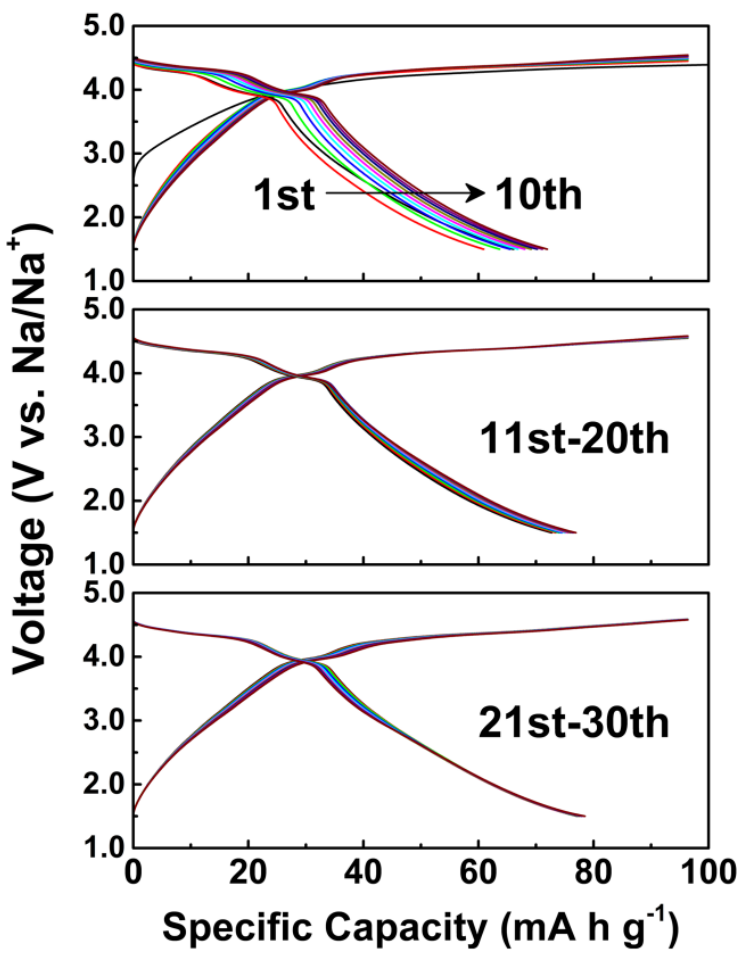


Figure 5.3.10 Galvanostatic voltage profiles of $\text{Na}_2\text{CoP}_2\text{O}_7$ -NPs/C at 0.2 C.

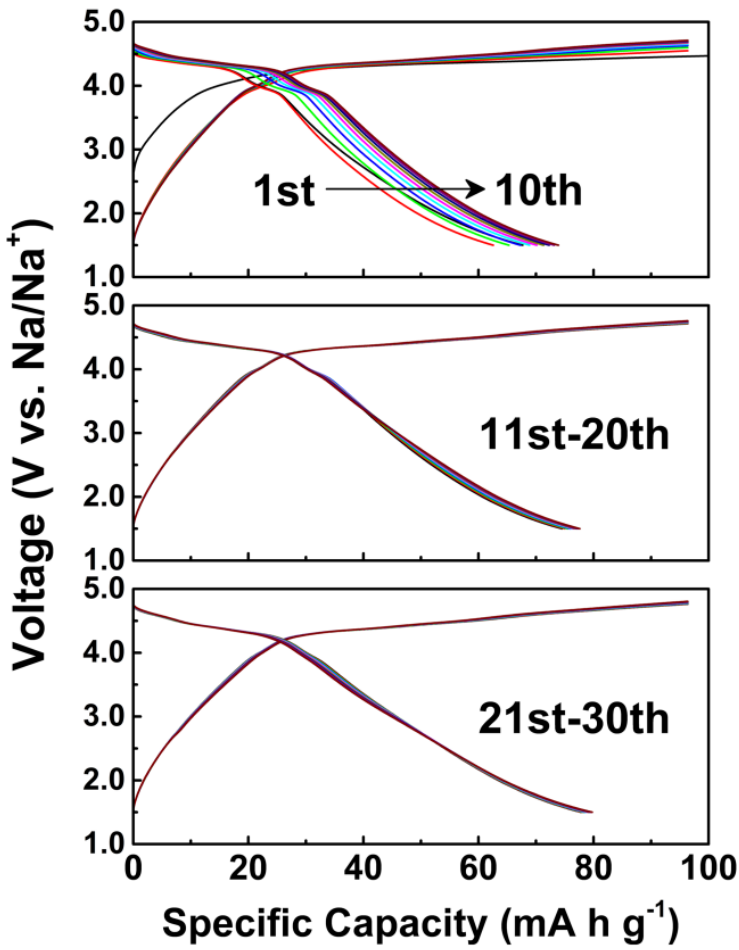


Figure 5.3.11 Galvanostatic voltage profiles of $\text{Na}_{1.8}\text{Co}_{1.1}\text{P}_2\text{O}_7$ -NPs/C at 0.2 C.

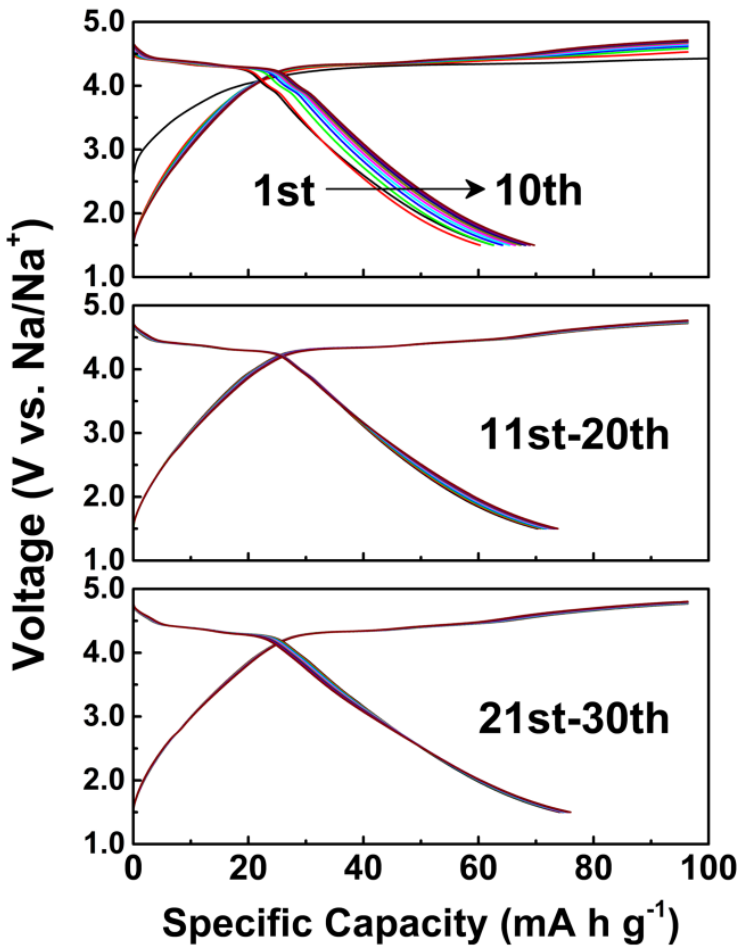


Figure 5.3.12 Galvanostatic voltage profiles of $\text{Na}_{1.6}\text{Co}_{1.2}\text{P}_2\text{O}_7\text{-NPs/C}$ at 0.2 C.

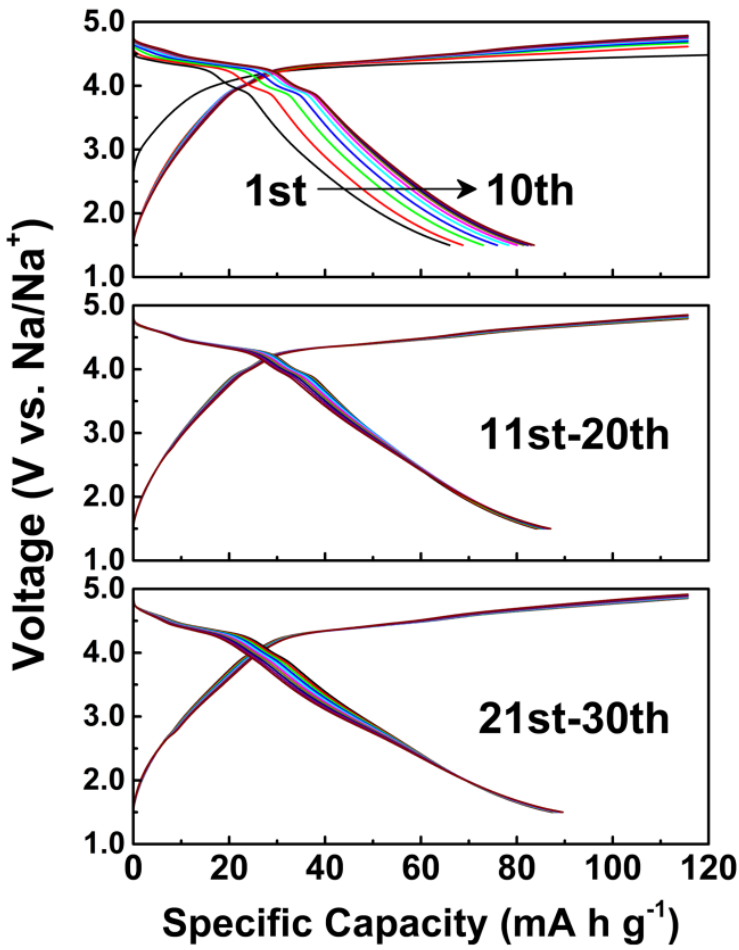


Figure 5.3.13 Galvanostatic voltage profiles of $\text{Na}_{1.8}\text{Co}_{1.1}\text{P}_2\text{O}_7$ -NPs/C charged to 120 mA h g^{-1} and discharged to 1.5 V at 0.2 C .

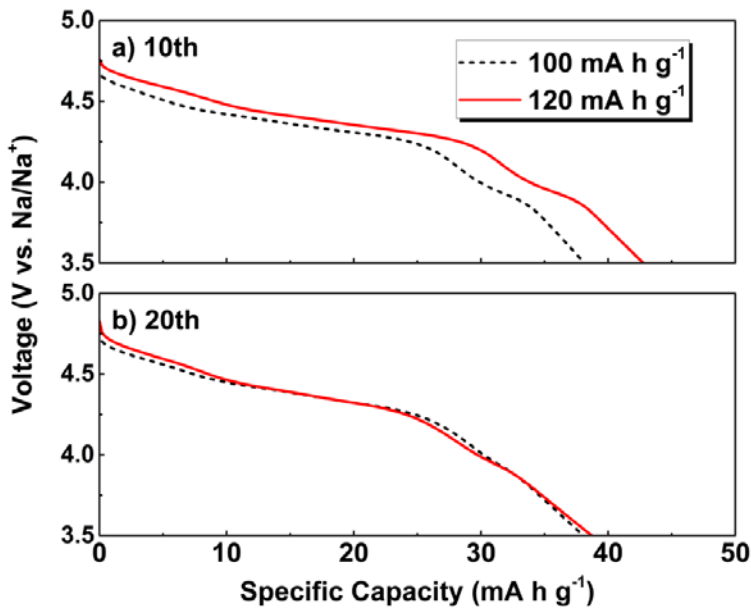


Figure 5.3.14 Comparison of discharge voltage profiles of $\text{Na}_{1.8}\text{Co}_{1.1}\text{P}_2\text{O}_{7-}$ NPs/C charged to 100 and 120 mA h g^{-1} , respectively, at 10th and 20th cycle.

5.4 Bibliography

- [5.1] F. Erragh, A. Boukhari, B. Elouadi, E. M. Holt, *J. Crystallogr. Spectrosc. Res.*, **1991**, *21*, 321–326.
- [5.2] P. Barpanda, J. Lu, T. Ye, M. Kajiyama, S.-C. Chung, N. Yabuuchi, S. Komaba, A. Yamada, *RSC Advances*, **2013**, *3*, 3857.
- [5.3] H. Kim, C. S. Park, J. W. Choi and Y. Jung, *Angew. Chem. Int. Ed.*, **2016**, *55*, 6662-6666.
- [5.4] A. S. Barnard, L. A. Curtiss, *Nano Lett.*, **2005**, *5*, 1261-1266.
- [5.5] A. S. Barnard, P. Zapol, *J. Chem. Phys.*, **2004**, *121*, 4276-4283.
- [5.6] W. Li, C. Ni, H. Lin, C. P. Huang, S. I. Shah, *J. Applied Phys.*, **2004**, *96*, 6663.
- [5.7] R. Lopez, T. E. Haynes, L. A. Boatner, L. C. Feldman, R. F. Haglund, *Phys. Rev. B*, **2002**, *65*, 224113.
- [5.8] R. C. Garvie, M. F. Goss, *J. Mater. Sci.*, **1986**, *21*, 1253-1257.
- [5.9] C.-C. Chen, A. B. Herhold, C. S. Johnson, A. P. Alivisatos, *Science*, **1997**, *276*, 398-401.
- [5.10] H. Kim, R. A. Shakoor, C. Park, S. Y. Lim, J.-S. Kim, Y. N. Jo, W. Cho, K. Miyasaka, R. Kahraman, Y. Jung and J. W. Choi, *Advanced Functional Materials*, **2013**, *23*, 1147-1155.

Chapter 6. Free-Standing Electrodes

6.1 Experiments

Fabrication of Free-Standing Electrodes

PCC was prepared by a thermal etching process as reported in a previous paper.

[6.1] Commercial clean CC (CeTech) was pre-treated with UV-ozone for 30 min to make it hydrophilic. $\text{FeCl}_3 \cdot 6\text{H}_2\text{O}$ (12 mmol, 97%, Sigma-Aldrich) and NaNO_3 (80 mmol, 99%, Sigma-Aldrich) were added into 80 mL distilled water under magnetic stirring, and the pH was adjusted to 1.5. This solution was transferred to a 100 mL Teflon-lined stainless steel autoclave, together with the CC, and hydrothermally reacted at 95 °C for 6 h in an electronic oven. After the hydrothermal reaction was complete, FeOOH nanorods grown on the CC were washed, dried, and heat-treated at 900 °C for 1 h in Ar. PCC was obtained by completely dissolving the ferric oxide in concentrated hydrochloric acid.

$\text{Na}_2\text{FeP}_2\text{O}_7$ -NPs/C slurry was prepared by ball milling of $\text{Na}_2\text{FeP}_2\text{O}_7$ -NPs/C that were first heat-treated with ZrO_2 balls and ethanol. After filtering out the ZrO_2 balls, a piece of CC was dipped in the $\text{Na}_2\text{FeP}_2\text{O}_7$ -NPs/C slurry for 1 h, taken out, dried, and heat-treated in a tube furnace at 600 °C for 3 h under flowing 5% H₂/Ar balance gas for the fabrication of $\text{Na}_2\text{FeP}_2\text{O}_7$ -NPs/C@PCC.

Materials Characterization

X-ray diffraction (XRD) patterns of the powder samples were measured with a Bruker D8-Advance using Cu K α radiation. Field-emission scanning electron microscopy (FESEM) images were taken by a Hitachi SU-70.

Electrochemical Measurements

The electrochemical properties of all free-standing electrodes were evaluated using coin-type (CR2032) half cells that were fabricated in an Ar-filled glove box. Working electrodes were fabricated without conductive agents and binder. The average mass loading of the active materials on PCC was 1-1.5 mg cm⁻². The cells were assembled with a working electrode, a separator film (glass microfiber), and Na-metal foil as the counter electrode saturated with a liquid electrolyte consisting of 1 M NaClO₄ dissolved in a solution of ethylene carbonate and propylene carbonate (EC/PC), at a volume ratio of 1:1. The fabricated cells were galvanostatically cycled using an automatic battery cycler (WBCS3000, WonATech, Korea). Free-standing electrodes were cycled at voltages ranging from 2.0 to 4.0 V.

6.2 Porous Carbon Cloth

As mentioned above (chapter 1 in Introduction), CC not only displays excellent mechanical flexibility and strength compared to other carbon-based flexible substrates, it also serves as a three-dimensional current collector, replacing traditional Cu or Al foil. [6.1] So, CC was adopted as a flexible current collector in this work.

Schematic illustrations in Figure 6.2.1 present the overall fabrication process of the $\text{Na}_2\text{FeP}_2\text{O}_7$ -NPs/C on the surface of porous carbon cloth ($\text{Na}_2\text{FeP}_2\text{O}_7$ -NPs/C@PCC) electrode. First, $\text{Na}_2\text{FeP}_2\text{O}_7$ -NPs/C was synthesized via a sol-gel method, followed by a post-heat treatment process. Second, $\text{Na}_2\text{FeP}_2\text{O}_7$ -NPs/C slurry was prepared by ball milling the $\text{Na}_2\text{FeP}_2\text{O}_7$ -NPs/C with ethanol media. Then, $\text{Na}_2\text{FeP}_2\text{O}_7$ -NPs/C slurry were uniformly coated on the surface of the CC by dip-coating, and then, dried. After heat treatment, $\text{Na}_2\text{FeP}_2\text{O}_7$ -NPs/C@PCC electrodes could be fabricated.

We selected CC with a fair amount of surface and a diameter of 7–8 μm in size (Figure 6.2.2) as a flexible current collector because it has been the main candidate for flexible electrodes in flexible LIBs. PCC modified by thermal etching from commercial CC was used as a flexible current collector for increasing the contact area between $\text{Na}_2\text{FeP}_2\text{O}_7$ -NPs/C and CC, and for removing some pre-treated material on the surface of commercial CC. Preparation of PCC was as follows;

i) UV-ozone treatment for CC

Clean bare-CC was pre-treated with UV-ozone for 30 min to make its surface hydrophilic for fully wetting in water in hydrothermal process.

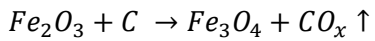
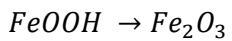
Even though bare-CC was in contact with D.I. water for a long time, water did not permeate it (Figure 6-1-3a). After UV-ozone treatment of bare-CC, however, it can be seen that water easily permeates (Figure 6-1-3b). Because the surface of bare-CC was modified from hydrophobic to hydrophilic through the UV-ozone treatment, CC can be immersed into an aqueous solution for hydrothermal process.

ii) Hydrothermal reaction

CC in ferric solution ($\text{FeCl}_3 + \text{NaNO}_3$) was hydrothermally reacted at 95 °C for 6 h in an electronic oven. After the hydrothermal process, dense FeOOH nanorods of uniform size and morphology were grown on the surface of CC (Figure 6.2.4a).

iii) Thermal etching

By heat-treating the FeOOH-CC at 900 °C for 1 h in inert atmosphere flowing Ar gas, the FeOOH nanorods were transformed to Fe_3O_4 particles, simultaneously with a partial reaction of C on the surface of CC with O, becoming CO_x , resulting in the embedding of Fe_3O_4 on the surface of CC (Figure 6.2.5b). [6.1]



iv) HCl etching and drying

Upon immersion of Fe_3O_4 -embedded CC in HCl to fully dissolve the embedded Fe_3O_4 , PCC was obtained (Figure 5e).

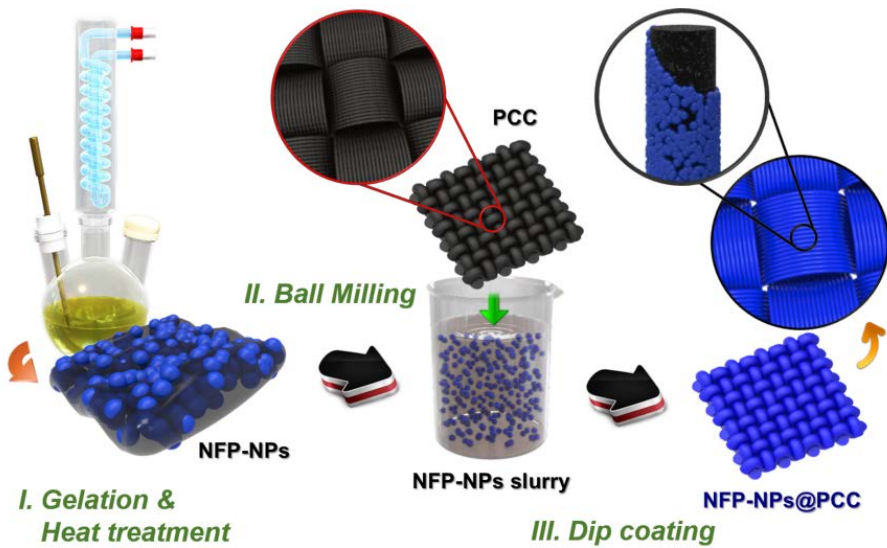


Figure 6.2.1 Schematic illustration of the fabrication of $\text{Na}_2\text{FeP}_2\text{O}_{7-}$ -NPs/C@PCC electrode.

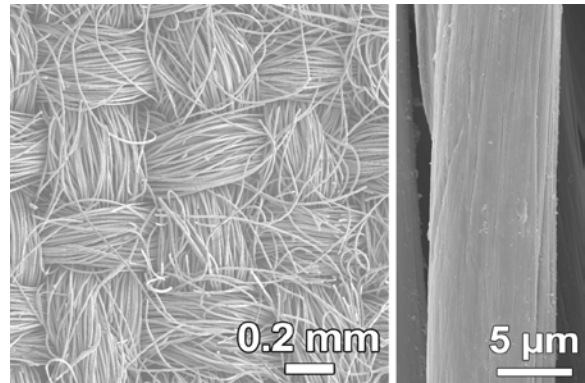


Figure 6.2.2 FESEM images of bare-CC.

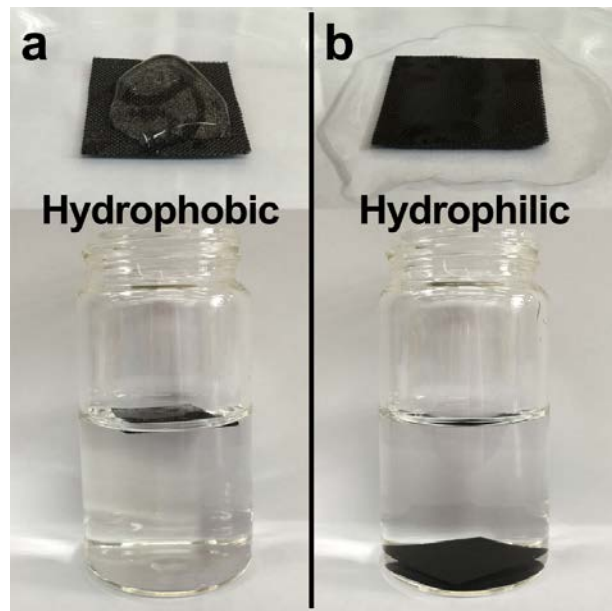


Figure 6.2.3 Digital photographs of (a) bare-CC and (b) UV-ozone-treated CC with water.

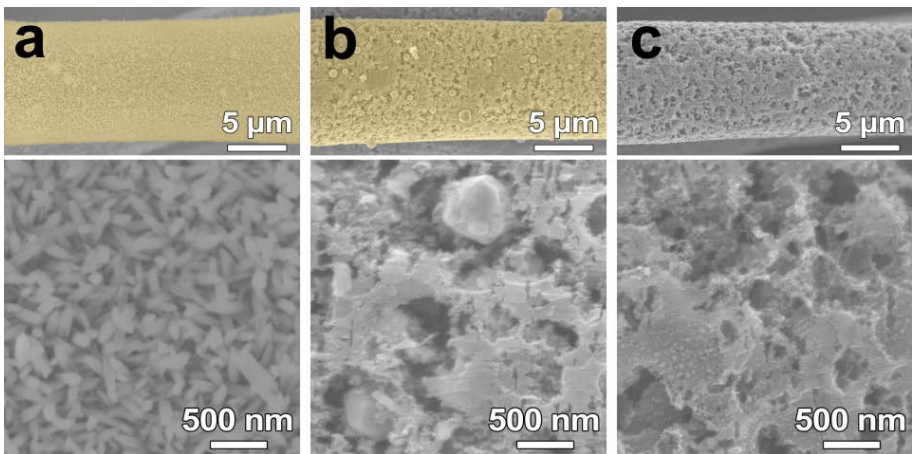


Figure 6.2.4 FESEM images of (a) FeOOH@CC, (b) Fe_3O_4 embedded in CC, and (e) PCC.

6.3 Na₂FeP₂O₇/C Nanocomposite on Porous Carbon Cloth

6.3.1 Fabrication of Na₂FeP₂O₇/C Nanocomposite on Porous Carbon Cloth

Free-standing Na₂FeP₂O₇-NPs/C@PCC electrodes without conductive agents and binders were fabricated by combining the Na₂FeP₂O₇-NPs/C slurry prepared by ball milling with ethanol and PCC through a dip-coating process.

Figure 6.3.1 shows the schematic illustration of the Na₂FeP₂O₇-NPs/C@PCC electrode. After dip-coating, drying and heat-treating, although there was no binder between the Na₂FeP₂O₇-NPs/C and PCC, all the Na₂FeP₂O₇-NPs/C were attached well on the surface of PCC without any unattached particles (Figure 6.3.2). In addition, the SEM image and EDS elemental mapping of a piece of Na₂FeP₂O₇-NPs/C@PCC shows that a thin layer of Na₂FeP₂O₇-NPs/C was uniformly coated on the surface of PCC (Figure 6.3.2 and Figure 6.3.3), and the particle size of these Na₂FeP₂O₇-NPs/C on the surface of PCC was less than 50 nm, indicative of no particle size change. XRD patterns of Na₂FeP₂O₇-NPs/C@PCC indicated that all reflection peaks except for the two peaks related to CC (broad peak at $2\theta = 25^\circ$ and sharp peak at $2\theta = 29^\circ$) coincided with those of B-Na₂FeP₂O₇/C (Figure 6.3.4).

Considering the above analysis, Na₂FeP₂O₇-NPs/C maintain their original states in this dip-coating process. Interestingly, Na₂FeP₂O₇-NPs/C@PCC also maintained their exceptional flexibility in spite of applying

various physical and chemical treatments during the dip-coating process
(Figure 6.3.5).

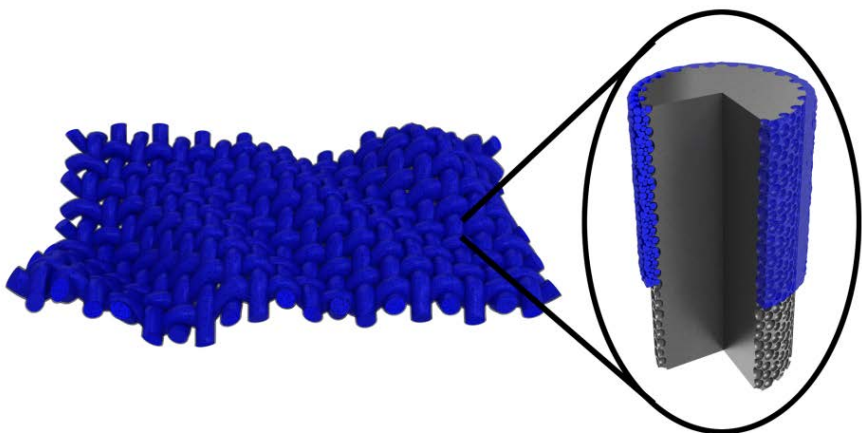


Figure 6.3.1 Schematic illustration of the $\text{Na}_2\text{FeP}_2\text{O}_7\text{-NPs/C@PCC}$ electrode.

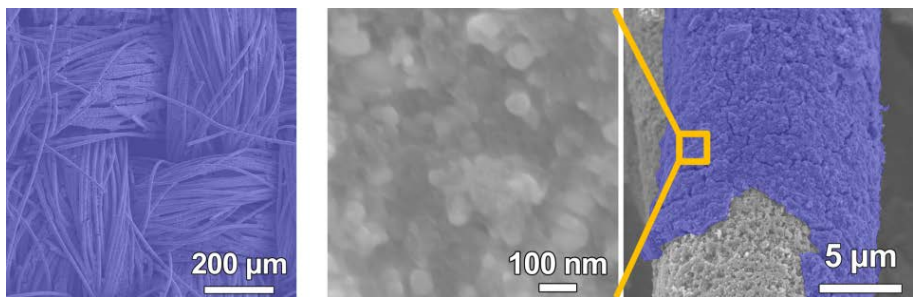


Figure 6.3.2 FESEM images of $\text{Na}_2\text{FeP}_2\text{O}_7$ -NPs/C@PCC.

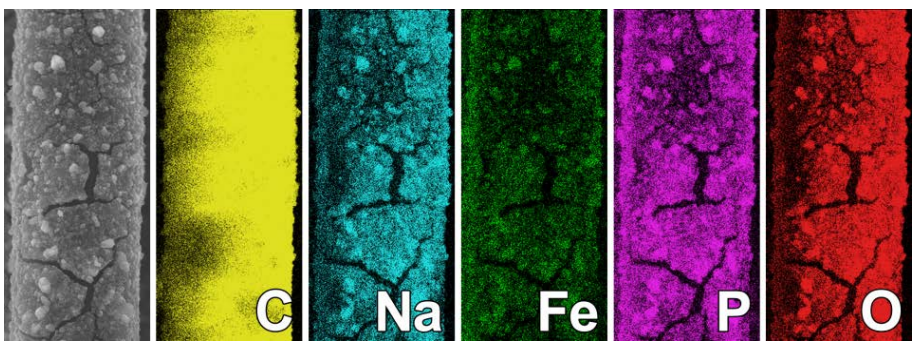


Figure 6.3.3 EDS elemental mapping of Na₂FeP₂O₇-NPs/C@PCC.

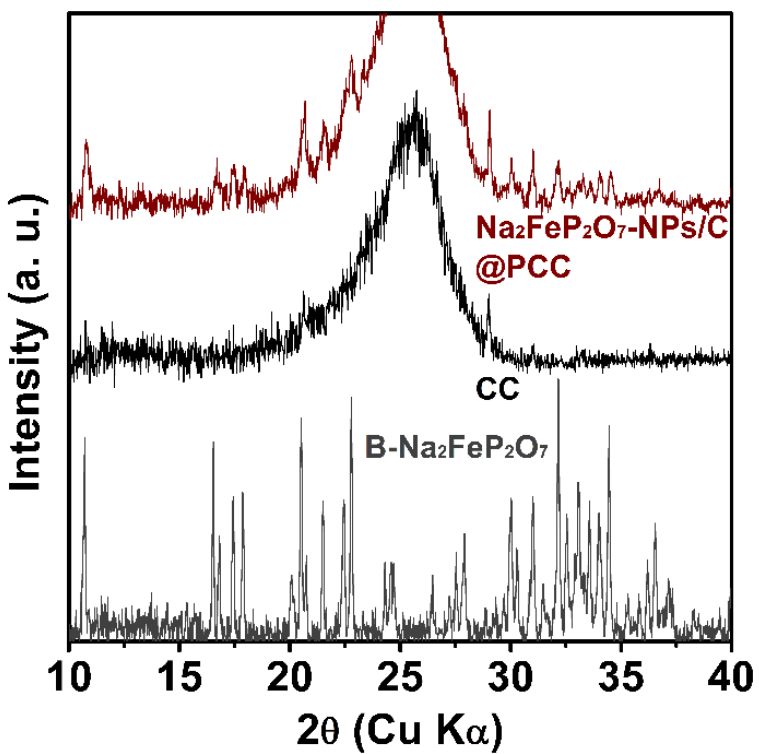


Figure 6.3.4 XRD patterns of commercial bare-CC and Na₂FeP₂O₇-NPs/C@PCC.

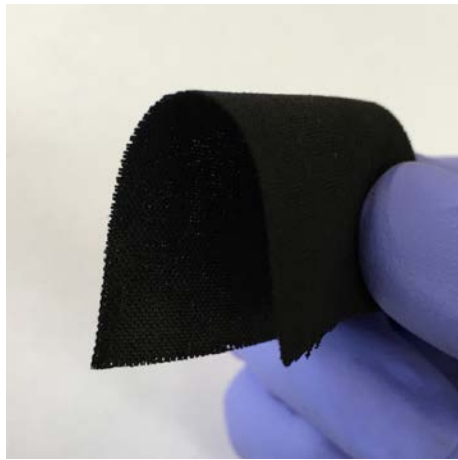


Figure 6.3.5 Digital photograph of flexible Na₂FeP₂O₇-NPs/C@PCC electrode.

6.3.2 Na₂FeP₂O₇/C Nanocomposite on Porous Carbon Cloth for Na-Ion Batteries

The cyclic performance of the conductive agents- and binder-free Na₂FeP₂O₇-NPs/C@PCC electrodes was evaluated. First, the rate performance of Na₂FeP₂O₇-NPs/C@PCC from 0.1 to 10 C was presented in Figure 6.3.6. With increasing rates of 0.1, 0.2, 0.5, 1 and 2 C, the discharge capacities of Na₂FeP₂O₇-NPs/C@PCC were measured to be 95, 93, 90, 87 and 84 mA h g⁻¹, respectively, which showed the equal rate performance up to 2 C compared to that of M-Na₂FeP₂O₇-NPs/C electrode (shown in Figure 4.1.20 of chapter 4) despite the absence of conductive agents and binder in Na₂FeP₂O₇-NPs/C@PCC electrode. At the rate of 5 and 10 C, Na₂FeP₂O₇-NPs/C@PCC delivered 77 and 68 mA h g⁻¹ of discharge capacities, respectively, which still exhibited high rate capability.

Second, long-term cycling test at 10 C was measured. The discharge capacity at 2000th cycle was 56 mA h g⁻¹ which cyclic retention of Na₂FeP₂O₇-NPs/C@PCC was 82.0%. Even though no conductive agents and binders were added in Na₂FeP₂O₇-NPs/C@PCC electrode, it also exhibited superior fast charge/discharge capability and long-term cyclability. It is considered that this good cyclability of Na₂FeP₂O₇-NPs/C@PCC resulted from the uniform coating of Na₂FeP₂O₇-NPs/C on the surface of PCC without any unattached particles. In addition, the small volume change of Na₂FeP₂O₇ (approximately 2.1–2.6%) during the intercalation/deintercalation contributed to little detachment of

$\text{Na}_2\text{FeP}_2\text{O}_7$ -NPs/C from their original $\text{Na}_2\text{FeP}_2\text{O}_7$ -NPs/C@PCC architecture [6.2,6.3].

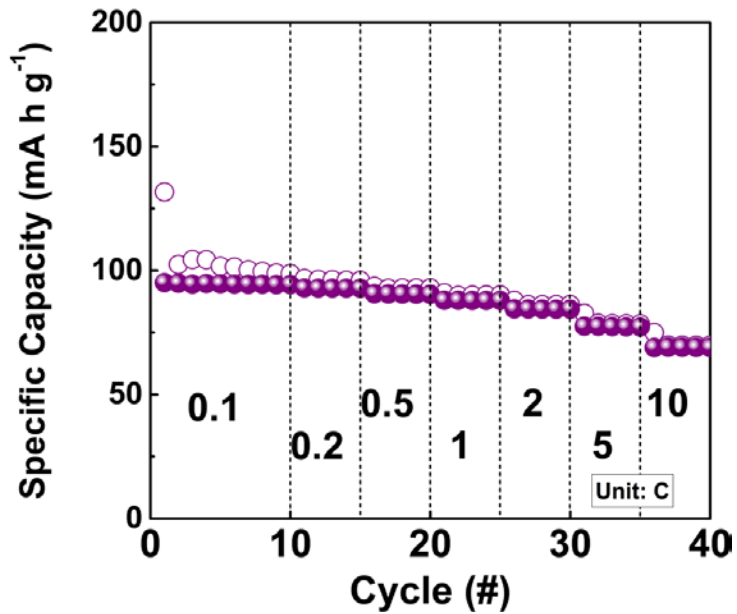


Figure 6.3.6 Rate capability of $\text{Na}_2\text{FeP}_2\text{O}_7$ -NPs/C@PCC.

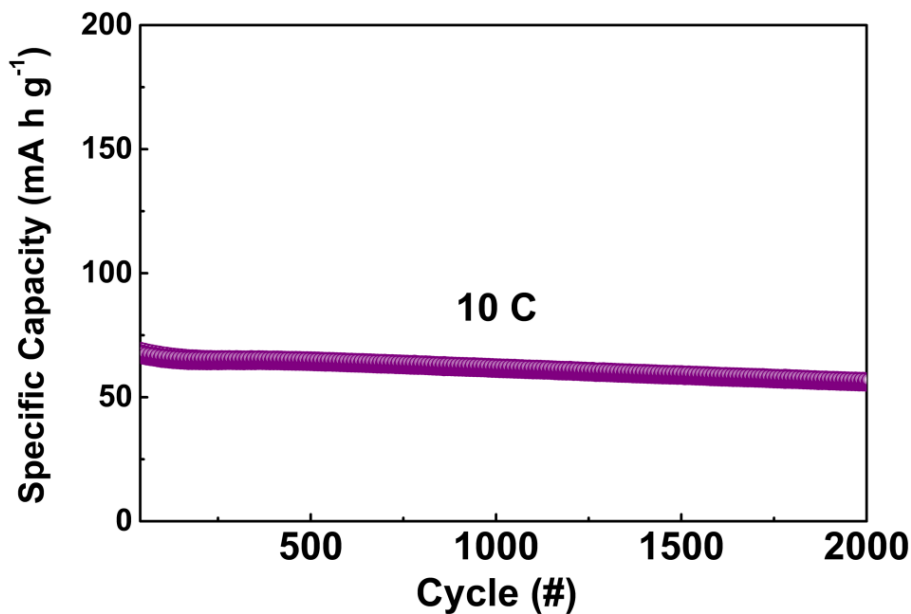


Figure 6.3.7 Long-term cyclability of $\text{Na}_2\text{FeP}_2\text{O}_7$ -NPs/C@PCC at 2000th cycle.

6.4 Bibliography

- [6.1] M.-S. Balogun, W. Qiu, F. Lyu, Y. Luo, H. Meng, J. Li, W. Mai, L. Mai, Y. Tong, *Nano Energy*, **2016**, *26*, 446-455.
- [6.2] P. Barpanda, G. Liu, C. D. Ling, M. Tamaru, M. Avdeev, S.-C. Chung, Y. Yamada, A. Yamada, *Chem. Mater.*, **2013**, *25*, 3480-3487.
- [6.3] P. Barpanda, T. Ye, S.-i Nishimura, S.-C. Chung, Y. Yamada, M. Okubo, H. Zhou, A. Yamada, *Electrochim. Commun.*, **2012**, *24*, 116-119.

Chapter 7. Conclusion

Synthetic strategy to prepare the $\text{Na}_2\text{MP}_2\text{O}_7$ NPs ($\text{M} = \text{Fe, Co, Ni}$) embedded in carbon composites with a size ranging from 20 nm to 50 nm was developed. They could be synthesized by a scalable and facile sol-gel method, followed by a post heat treatment process. $\text{Na}_2\text{MP}_2\text{O}_7$ -NPs/C without aggregation could be prepared after an additional ball milling and re-heat treatment process.

In the case of $\text{Na}_2\text{FeP}_2\text{O}_7$ -NPs/C, it exhibited not only a high reversible capacity, close to the theoretical value at low rates after the first cycle, but also a superior rate capability of 77, 70, 66 and 65 mA h g^{-1} at 10, 20, 30 and 60 C and exceptional long-term cyclability over 10000 cycles at 10 C and 60 C, compared to those reported to date attributed to facile Na-ion migration resulted from the particle size reduction and increase in the surface.

For the cathode material with higher specific capacity and power in NIBs, $\text{Na}_{3.12}\text{Fe}_{2.44}(\text{P}_2\text{O}_7)_2$ -NPs/C/rGO composite was successfully synthesized by the same synthetic process with that of $\text{Na}_2\text{FeP}_2\text{O}_7$ -NPs/C/rGO. GO was reduced to rGO in the heat treatment process. $\text{Na}_{3.12}\text{Fe}_{2.44}(\text{P}_2\text{O}_7)_2$ NPs embedded in tiny carbon flakes with a particle size under 50 nm were well-incorporated with rGO. The addition of only small amount of rGO resulted in advances in the electrochemical performance of $\text{Na}_{3.12}\text{Fe}_{2.44}(\text{P}_2\text{O}_7)_2$ -NPs/C. This rGO-supported $\text{Na}_{3.12}\text{Fe}_{2.44}(\text{P}_2\text{O}_7)_2$ -NPs/C composite exhibited a superior rate capability (92, 85 and 78 mA h g^{-1} at 2, 5 and 10 C), and long-term cyclic

stability (capacity retention of 70% over 5000th cycle at 10 C). This low-cost elements and exceptional electrochemical performance of NFP- $\text{Na}_{3.12}\text{Fe}_{2.44}(\text{P}_2\text{O}_7)_2$ -NPs/C/rGO enable it to apply in the large-scale electrical energy storage.

For the cathode material with higher operating voltage and specific capacity in NIBs, rose phase $\text{Na}_{2-2x}\text{Co}_{1+x}\text{P}_2\text{O}_7$ -NPs/C ($0 \leq x \leq 0.2$) were synthesized. Prior to this, various synthetic conditions to synthesize metastable rose phase $\text{Na}_{2-2x}\text{Co}_{1+x}\text{P}_2\text{O}_7$ in microscale were established. Rose phase could be synthesized at lower annealing temperature. With the increasing of Co element and decreasing of Na element for charge balance in non-stoichiometric $\text{Na}_{2-2x}\text{Co}_{1+x}\text{P}_2\text{O}_7$ compounds, metastable rose phase could be obtained stably at higher annealing temperature compared to stoichiometric compound.

In contrast to B- $\text{Na}_{2-2x}\text{Co}_{1+x}\text{P}_2\text{O}_7$, pure metastable rose could become to major products both stoichiometric and non-stoichiometric $\text{Na}_{2-2x}\text{Co}_{1+x}\text{P}_2\text{O}_7$ /C nanocomposites. For the first time, $\text{Na}_{2-2x}\text{Co}_{1+x}\text{P}_2\text{O}_7$ /C exhibited the long plateau in high voltage ranges and higher discharge capacity of 90 mA h g⁻¹ compared to B- $\text{Na}_{1.8}\text{Co}_{1.1}\text{P}_2\text{O}_7$ /C. The solution of electrolyte decomposition problem at high voltage will bring out the improvement of electrochemical performance.

Finally, uniformly coated $\text{Na}_2\text{FeP}_2\text{O}_7$ -NPs/C on the surface of the PCC electrode could be fabricated by combining the $\text{Na}_2\text{FeP}_2\text{O}_7$ -NPs/C slurry prepared by ball-milling the $\text{Na}_2\text{FeP}_2\text{O}_7$ -NPs/C with ethanol and PCC prepared

by thermal etching of the commercial CC through a simple dip-coating process.

This conductive agent- and binder-free $\text{Na}_2\text{FeP}_2\text{O}_7$ -NPs/C@PCC electrode delivered comparable capacity to $\text{Na}_2\text{FeP}_2\text{O}_7$ -NPs/C, and also exhibited excellent rate capability and long-term cyclability over 2000 cycles even at 10 C, and can be used as a flexible electrode in NIBs.

Abstract in Korean

국 문 초 록

전세계적으로 에너지 수요 및 저장이 계속적으로 늘어나면서 친환경적인 에너지 저장 장치가 중요한 이슈로 떠오르고 있다. 이차전지는 기존의 화석연료 및 원자력 반응을 통해 얻거나 또는 태양, 바람 등의 친환경 원료로부터 생산된 에너지를 효율적으로 저장할 수 있는 전기화학적 에너지 저장 장치로, 이중 리튬이차전지(또는 리튬이온전지)는 고 출력, 고 에너지 밀도, 낮은 메모리 효과, 긴 수명 특성 및 친환경적인 특성으로 인해 에너지 저장 장치로 많이 사용되고 있다. 최근에는 리튬이차전지 내 무게 및 부피 에너지 밀도를 발전시키는 연구가 많이 이루어지며 이로 인해 리튬이차전지는 전기자동차, 또는 그리드규모 에너지 저장 장치 등의 대용량 에너지 저장 장치에 적용하려고 한다. 그러나 리튬 원자재의 희소성 및 세계적으로 불균등한 매장 등으로 인한 높은 가격은 대용량 에너지 저장 장치에 사용되기에 단점을 가진다. 따라서 새로운 이차전지의 개발이 필요하다.

소듐이차전지는 값싼 소듐 원자재로 인해 대용량 에너지 저장 장치 산업에서 차세대 리튬이차전지로 각광받고 있다. 특히, 소듐이차전지 양극소재는 리튬이차전지 양극소재와 전기화학적 반응에서 그 유사성을 지녀 쉽게 적용할 수 있는 장점이 있다.

따라서 고성능 소듐이차전지 양극소재의 개발이 필요하고 이에 연구가 진행되고 있다. 이를 중 피로인산염계 기반 다음이온 구조 물질 ($\text{Na}_2\text{MP}_2\text{O}_7$; M = 전이금속)은 화학적, 열적 안정 및 우수한 전기화학적 특성으로 인해 소듐이차전지 양극소재로 각광받고 있다.

따라서 본 연구에서는 나노 및 조성 관점에서 피로인산염계 물질을 설계 및 합성하고 이의 고성능 소듐이차전지 양극물질로서의 전기화학적 특성을 평가한다. 또한 이렇게 합성한 양극물질과 유연물질을 결합하여 고성능 유연전극 소듐이차전지를 제작하고 이의 전기화학적 특성을 평가한다. 이를 위해 먼저 졸-겔 및 추가 열처리 공정을 통해 카본으로 잘 둘러싸여있는 $\text{Na}_2\text{MP}_2\text{O}_7$ ($\text{M} = \text{Fe}, \text{Co}, \text{Ni}$) 나노복합체를 합성하는 전략을 제시하였다. 이 합성 방법을 통해 50 nm 이하 크기의 나노 입자들이 카본에 균일하게 잘 들어가 있는 $\text{Na}_2\text{MP}_2\text{O}_7$ ($\text{M} = \text{Fe}, \text{Co}, \text{Ni}$) 나노복합체를 합성할 수 있다.

철 기반 피로인산염 ($\text{Na}_2\text{FeP}_2\text{O}_7$) 관점에서 연구를 먼저 진행한다. $\text{Na}_2\text{FeP}_2\text{O}_7$ 나노복합체는 이론용량과 매우 근접한 용량을 보였다. 또한, 이는 10-60 C의 매우 빠른 전류밀도에서도 77-65 mA h g⁻¹ 사이의 높은 출력 특성과 10000 사이클 이상에서 용량 저하 적은 긴 수명 특성을 보였다. 한편, 조성 변화를 통해 철 기반 피로인산염 물질의 전기화학적 특성을 향상한다. $\text{Na}_{3.12}\text{Fe}_{2.44}(\text{P}_2\text{O}_7)_2$ 는 $\text{Na}_2\text{FeP}_2\text{O}_7$ 에 비해 구조 내 더 많은 $\text{Fe}^{2+}/\text{Fe}^{3+}$ 산화/환원 반응이 일어나 실제 용량 및 에너지 밀도의 향상이 기대된다. 따라서 같은

합성 방법으로 $\text{Na}_{3.12}\text{Fe}_{2.44}(\text{P}_2\text{O}_7)_2$ 나노복합체를 합성하고 이의 전기화학적 특성을 평가하였다. 실제로, $\text{Na}_{3.12}\text{Fe}_{2.44}(\text{P}_2\text{O}_7)_2$ 나노복합체는 $\text{Na}_2\text{FeP}_2\text{O}_7$ 나노복합체보다 더 높은 용량을 보였다. 추가적으로, 환원된 그래핀 산화물을 첨가한 $\text{Na}_{3.12}\text{Fe}_{2.44}(\text{P}_2\text{O}_7)_2$ 나노복합체를 합성하였고 이는 기존 나노복합체보다 더 좋은 출력 및 긴 수명 특성을 보였다.

코발트 기반 피로인산염 ($\text{Na}_2\text{CoP}_2\text{O}_7$) 은 세 가지 구조가 존재한다. 그 중 triclinic 다형체 (rose phase; 로즈 상)는 $\text{Na}_2\text{FeP}_2\text{O}_7$ 와 유사한 구조를 가지면서, $\text{Na}_2\text{FeP}_2\text{O}_7$ 보다 매우 높은 작동 전압 특성을 보인다. 하지만 로즈 상은 준 안정상으로 일반적인 합성 조건에서 쉽게 합성되지 않는다. 따라서 고상법을 통해 다양한 합성 조건 (열처리 온도, 시간, 조성 비율)을 변경하여 로즈 상이 합성되는 조건을 논의한다. 로즈 상은 비교적 낮은 온도 (500 도)에서 합성이 가능하며, 조성 내 코발트 비율이 늘고 소듐 비율이 줄면 ($\text{Na}_{2-2x}\text{Co}_{1+x}\text{P}_2\text{O}_7$; $0 \leq x \leq 0.2$) 더 높은 온도에서도 준 안정상의 로즈 상이 안정하게 합성되었다.

$\text{Na}_2\text{CoP}_2\text{O}_7$ 나노복합체는 고상법으로 합성한 마이크로크기 입자와는 달리 비교적 높은 온도 (600 도)에서도 주안정상의 로즈 상이 안정하게 합성되었다. 마찬가지로 조성 내 코발트, 소듐 비율을 달리 하여도 로즈 상의 나노복합체가 합성되었다. 이렇게

합성된 $\text{Na}_{2-2x}\text{Co}_{1+x}\text{P}_2\text{O}_7$ 나노복합체는 마이크로입자와는 달리 고 전압에서 90 mA h g^{-1} 이상의 안정된 용량을 나타내었다.

마지막으로, 유연 전극으로 사용하기 위해 다공성의 탄소 섬유 표면에 담금 코팅 방법을 통해 $\text{Na}_2\text{FeP}_2\text{O}_7$ 나노복합체를 코팅한 전극을 제작하였다. 이렇게 제작된 유연 전극은 도전제 및 바인더 첨가 없이도 매우 우수한 출력 및 긴 수명 특성을 보였다.

현재까지 서술한 바와 같이, 본 연구는 나노 및 조성 공학을 통해 피로인산염계 나노복합체 합성, 이의 고성능 소듐이차전지용 양극소재로서의 전기화학적 특성 평가 및 이와 다공성 탄소 섬유의 결합을 통해 유연 전극으로서의 가능성을 평가하는데 초점을 맞췄다. 더 나아가, 본 연구에서 사용한 합성 전략은 다른 피로인산염계 나노복합체 등에 적용할 수 있으며, 현재 소듐이차전지 및 다른 에너지 저장 장치가 직면하고 있는 문제점을 해결할 수 있는 돌파구를 마련할 수 있을 것이다.

주요어: 피로인산염, 나노복합체, 줄-겔, 유연 전극, 탄소 섬유, 담금 코팅, 양극, 소듐이온전지, 소듐이차전지

학 번: 2010-20608

Research achievements

1) Refereed papers

33. H. J. Song, M. Choi, J. -C. Kim, S. Park, C. W. Lee, S. -H. Hong, B. -K. Kim, D. -W. Kim, Enhanced Lithium Storage in Reduced Graphene Oxide-supported M-phase Vanadium(IV) Dioxide Nanoparticles, *Sci. Rep.*, **2016**, 6, 30202.
32. H. J. Song, C. W. Lee, S. W. Hwang, I. S. Cho, Wet-chemical preparation of barium magnesium orthophosphate, $\text{Ba}_2\text{Mg}(\text{PO}_4)_2:\text{Eu}^{2+}$, nanorod phosphor with enhanced optical and photoluminescence properties, *RSC Adv.*, **2016**, 6, 61378-61385.
31. S. Park, C. W. Lee, J. -C. Kim, H. J. Song, H. -W. Shim, S. Lee, D. -W. Kim, Heteroepitaxy-induced rutile VO_2 with abundantly exposed (002) facets for high lithium electroactivity, *ACS Energy Lett.*, **2016**, 1, 216-224.
30. H. J. Song, M. Choi, J. -C. Kim, S. Park, C. W. Lee, S. -H. Hong, D. -W. Kim, “Li-electroactivity of thermally-reduced V_2O_3 nanoparticles”, *Mater. Lett.*, **2016**, 180, 243-246.
29. D. S. Kong, M. J. Kim, H. J. Song, I. S. Cho, S. Jeong, H. Shin, S. Lee, H. S. Jung, “Fine tuning of emission property of white light-emitting diodes by quantum-dot-coating on YAG:Ce nanophosphors”, *Appl. Surf. Sci.*, **2016**, 379, 467-473.

28. S. Park, H. -W. Shim, C. W. Lee, H. J. Song, J. -C. Kim, D. -W. Kim, “High-power and long-life supercapacitive performance of hierarchical, 3-D urchin-like $W_{18}O_{49}$ nanostructure electrodes”, *Nano Res.*, **2016**, *9*, 633-643.
27. J. -C. Kim, M. Choi, D. -S. Kim, H. J. Song, D. -W. Kim, “Windshield-waste-driven synthesis of hydroxy sodalite”, *J. Ceram. Soc. Japan*, **2015**, *123*, 1022-1026.
26. J. -C. Kim, M Choi, H. J. Song, J. E. Park, J. -H. Yoon, K. -S. Park, C. G. Lee, D. -W. Kim, “Synthesis of uniform-sized zeolite from windshield waste”, *Mater. Chem. Phys.*, **2015**, *166*, 20-25.
25. C. W. Lee, H. K. Park, S. Park, H. S. Han, S. W. Seo, H. J Song, S. Shin, D. -W. Kim, K. S. Hong, “Ta-substituted $SnNb_{2-x}Ta_xO_6$ photocatalysts for hydrogen evolution under visible light irradiation”, *J. Mater. Chem. A*, **2015**, *3*, 825-831.
24. S. Park, H. J. Song, C. W. Lee, S. W. Hwang, I. S. Cho, “Enhanced photocatalytic activity of ultrathin $Ba_5Nb_4O_{15}$ two-dimensional nanosheets”, *ACS Appl. Mater. Interfaces*, **2015**, *7*, 21860-21867.
23. H. J. Song,[‡] J. -C. Kim,[‡] M. Choi, C. Choi, M. A. Dar, C. W. Lee, S. Park, D. -W. Kim, “ Li_2MnSiO_4 nanorods-embedded carbon nanofibers for lithium-ion battery electrodes”, *Electrochim. Acta*, **2015**, *180*, 756-762.
(Equal contribution)

22. H. J. Song,[‡] J. –C. Kim,[‡] C. W. Lee, S. Park, M. A. Dar, S. –H. Hong, D. –W. Kim, “Reversible Li-storage in titanium(III) oxide nanosheets”, *Electrochim. Acta*, **2015**, *170*, 25-32. (Equal contribution)
21. C. W. Lee, J. –C. Kim, S. Park, H. J. Song, D. –W. Kim, “Highly stable sodium storage in 3-D gradational Sb–NiSb–Ni heterostructures”, *Nano Energy*, **2015**, *15*, 479-489.
20. H. –W. Shim, S. Park, H. J. Song, J. –C. Kim, E. Jang, K. S. Hong, T. D. Kim, D. –W. Kim, “Biomineralized multifunctional magnetite/carbon microspheres for applications in Li-ion batteries and water treatment”, *Chem. Eur. J.*, **2015**, *21*, 4655-4663.
19. C. W. Lee, S. –D. Seo, H. K. Park, S. Park, H. J. Song, D. –W. Kim, K. S. Hong, “High-areal-capacity lithium storage of the Kirkendall effect-driven hollow hierarchical NiS_x nanoarchitecture”, *Nanoscale*, **2015**, *7*, 2790-2796.
18. S. Park, H. –W. Shim, C. W. Lee, H. J. Song, I. J. Park, J. –C. Kim, K. S. Hong, D. –W. Kim, “Tailoring uniform γ-MnO₂ nanosheets on highly conductive three-dimensional current collectors for high-performance supercapacitor electrodes”, *Nano Res.*, **2015**, *8*, 990-1004.
17. S. Park, S. –D. Seo, H. J. Kim, C. W. Lee, H. J. Song, S. S. Shin, H. K. Park, K. S. Hong, D. –W. Kim, “Three-dimensional hierarchical Li₄Ti₅O₁₂ nanoarchitecture by a simple hydrothermal method”, *J. Nanosci. Nanotech.*, **2014**, *14*, 9307-9312.
16. M. J. Kim, J. H. Park, K. Y. Lee, S. Lee, G. –S. Han, H. J. Song, H. Shin, T. K. Ahn, H. S. Jung, “Cerium-doped yttrium aluminum garnet hollow shell

- phosphors synthesized via the Kirkendall effect”, *ACS Appl. Mater. Interfaces*, **2014**, 6, 1145-1151.
15. M. H. Lee, J. H. Park, H. S. Han, H. J. Song, I. S. Cho, J. H. Noh, K. S. Hong, “Nanostructured Ti-doped hematite (α -Fe₂O₃) photoanodes for efficient photoelectrochemical water oxidation”, *Int. J. Hydrogen Energy*, **2014**, 39, 17501-17507.
14. H. J. Song, J. -C. Kim, H. -S. Roh, C. W. Lee, S. Park, D. -W. Kim, K. S. Hong, “Anion-controlled synthesis of TiO₂ nano-aggregates for Li ion battery electrodes”, *Mater. Chact.*, **2014**, 96, 13-20.
13. S. Park, H. J. Kim, C. W. Lee, H. J. Song, S. S. Shin, S. W. Seo, H. K. Park, S. Lee, D. -W. Kim, K. S. Hong, “Sn self-doped α -Fe₂O₃ nanobranch arrays supported on a transparent, conductive SnO₂ trunk to improve photoelectrochemical water oxidation”, *Int. J. Hydrogen Energy*, **2014**, 39, 16459-4979.
12. S. Park, S. Kim, H. J. Kim, C. W. Lee, H. J. Song, S. W. Seo, H. K. Park, D. -W. Kim, K. S. Hong, “Hierarchical assembly of TiO₂-SrTiO₃ heterostructures on conductive SnO₂ backbone nanobelts for enhanced photoelectrochemical and photocatalytic performance”, *J. Hazard. Mater.*, **2014**, 275, 10-18.
11. D. K. Yim,[‡] H. J. Song,[‡] H. -S. Roh, S. -J. Kim, B. S. Han, Y. -H. Jin, H. -S. Hong, D. -W. Kim, K. S. Hong, “Luminescent properties of RbSrPO₄:Eu²⁺ phosphors for near-UV-based white-light-emitting diodes”, *Eur. J. Inorg. Chem.*, **2013**, 2013, 4662-4666. (Equal contribution)

10. H. J. Song,[‡] D. K. Yim,[‡] H. –S. Roh, I. S. Cho, S. –J. Kim, Y. –H. Jin, H. –W. Shim, D. –W. Kim, K. S. Hong, “RbBaPO₄:Eu²⁺: a new alternative blue-emitting phosphor for UV-based white light-emitting diodes”, *J. Mater. Chem. C*, **2013**, *1*, 500-505. (Equal contribution)
9. S. Hur, H. J. Song, H. –S. Roh, D. –W. Kim, K. S. Hong, “Enhancement of fluorescence by Ce³⁺ doping in green-emitting Ca₁₅(PO₄)₂(SiO₄)₆:Eu²⁺ phosphor for UV-based w-LEDs”, *Ceram. Int.*, **2013**, *39*, 9791-9795.
8. I. J. Park, H. –S. Roh, H. J. Song, D. H. Kim, J. S. Kim, W. M. Seong, D. –W. Kim, K. S. Hong, “γ-Al₂O₃ nanospheres-directed synthesis of monodispersed BaAl₂O₄:Eu²⁺ nanosphere phosphors”, *Cyrs. Eng. Comm.*, **2013**, *15*, 4797-4801.
7. S. Hur, H. J. Song, H –S. Roh, D. –W. Kim, K. S. Hong, “A novel green-emitting Ca₁₅(PO₄)₂(SiO₄)₆:Eu²⁺ phosphor for applications in n-UV based w-LEDs”, *Mater. Chem. Phys.*, **2013**, *139*, 350-354.
6. H. J. Song, J. H. Noh, H. –S. Roh, J. S. Kim, D. –W. Kim, K. S. Hong, “Preparation and characterization of nano-sized Y₃Al₅O₁₂:Ce³⁺ phosphor by high-energy milling process”, *Cur. Appl. Phys.*, **2013**, *13*, S69-S74.
5. H. –S. Roh, S. Hur, H. J. Song, I. J. Park, D. K. Yim, D. –W. Kim, K. S. Hong, “Luminescence properties of Ca₅(PO₄)₂SiO₄:Eu²⁺ green phosphor for near UV-based white LED”, *Mater. Lett.*, **2012**, *70*, 37-39.
4. H. J. Song, D. K. Yim, I. –S. Cho, H. –S. Roh, J. S. Kim, D. –W. Kim, K. S. Hong, “Luminescent properties of phosphor converted LED using an orange-emitting Rb₂CaP₂O₇:Eu²⁺ phosphor”, *Mater. Res. Bull.*, **2012**, *47*, 4522-4526.

3. H. -S. Roh, D. H. Kim, I. -J. Park, H. J. Song, S. Hur, D. -W. Kim, K. S. Hong, “Template-free synthesis of monodispersed $\text{Y}_3\text{Al}_5\text{O}_{12}:\text{Ce}^{3+}$ nanosphere phosphor”, *J. Mater. Chem.*, **2012**, 22, 12275-12280.
2. J. S. Kim, H. J. Song, H. -S. Roh, D. K. Yim, J. H. Noh, K. S. Hong, “Luminescent characteristics of green emitting $\text{Li}_2\text{Ca}_2\text{Si}_2\text{O}_7:\text{Eu}^{2+}$ phosphor”, *Mater. Lett.*, **2012**, 79, 112-115.
1. D. K. Yim, H. J. Song, I. -S. Cho, J. S. Kim, K. S. Hong, “A novel blue-emitting $\text{NaSrPO}_4:\text{Eu}^{2+}$ phosphor for near UV based white light-emitting-diodes”, *Mater. Lett.*, **2011**, 65, 1666-1668.

2) Patents

2. K. S. Hong, H. S. Jung, H. J. Song, D. H. Kim, S. Hur, J. S. Kim, C. W. Lee, Method for treating nano-phosphor with atmospheric pressure plasma, Korea patents, 10-2013-0044219.
1. K. S. Hong, H. S. Jung, C. W. Lee, S. K. Lee, K. J. Jung, D. H. Kim, H. J. Song, J. H. Noh, D. W. Kim, S. S. Choi, Y. S. Hwang, J. Y. Park, Method for manufacturing nano-particles of titanium-based oxide carbon complex, Korea patents, 10-2013-0038543.